

ABSTRACT

Title of dissertation: Dynamics and Control of a Hovering
Quadrotor in Unsteady Wind

William Stephen Craig
Doctor of Philosophy, 2019

Dissertation directed by: Professor Derek A. Paley
Department of Aerospace Engineering
and Institute for Systems Research

Quadrotor helicopters show great promise for a variety of missions in commercial, military, and recreational domains. Many of these missions require flight outdoors where quadrotors struggle, partially due to their high susceptibility to wind gusts. This dissertation addresses the problem of quadrotor flight in wind with (1) a physics-based analysis of the interaction between the wind and the quadrotor, (2) the addition of flow sensing onboard the quadrotor to measure external wind, and (3) both linear and nonlinear control development incorporating flow sensing and taking aerodynamic interactions into account. Using flow measurements in addition to traditional IMU sensing enables the quadrotor to react to the wind directly, rather than delaying until the wind affects the rigid-body dynamics as with IMU sensing alone.

The aerodynamic response of a quadrotor to wind is modeled using blade flapping, which characterizes the tilt of the rotor plane a result of uneven lift on the blades. The model is validated by mounting a motor and propeller to a spherical

pendulum and subjecting it to a wind gust. The blade-flapping model is utilized in a nonlinear geometric feedback-linearization controller that is built in a cascaded framework, first developing the inner-loop attitude controller, then the outer-loop position controller. The controller directly cancels the forces and moments resulting from aerodynamic disturbances using measurements from onboard flow probes, and also includes a variable-gain algorithm to address the inherent thrust limitations on the motors. A linear model and controller is also developed, using frequency-domain system-identification techniques to characterize the model, and handling-qualities-criteria based optimization to select gains. A linear model of the aerodynamic interactions, based on the blade-flapping work, provides flow-feedback capability similar to the nonlinear controller. Experimental testing is performed for each of the developed controllers, all of which show improvement through the use of flow feedback. Attitude is tested independently by mounting the quadrotor on a ball-joint, allowing for both gust and saturation testing. Gust rejection is also tested for both linear and nonlinear controllers in free flight, showing further benefits than considering attitude alone.

DYNAMICS AND CONTROL OF A HOVERING QUADROTOR
IN UNSTEADY WIND

by

WILLIAM STEPHEN CRAIG

Dissertation submitted to the Faculty of the Graduate School of the
University of Maryland, College Park in partial fulfillment
of the requirements for the degree of
Doctor of Philosophy
2019

Advisory Committee:
Professor Derek A. Paley
Professor Robert Sanner
Professor Roberto Celi
Professor Olivier Bauchau
Professor Balakumar Balachandran

© Copyright by
William Stephen Craig
2019

Dedication

To my wife Anna, for her unwavering support

Acknowledgments

First, I would like to thank my advisor and mentor Prof. Derek A. Paley. Without his guidance, support, and encouragement this truly would not have been possible. He has helped me to develop into the engineer I'm proud to be. He gave me the freedom to pursue my own ideas, while still ensuring that I remained on track, and he knew when to push me and when I already had more than enough. He helped me to expand on the tools I have and apply them in an effective and technically rigorous manner, and taught me how to convey my ideas with precision and clarity in writing and through presentation. He has shown me what it looks like to manage family life with the demands of a research position, and has prepared me well to succeed in my next role. He's someone I've looked up to since I began, and someone I will seek to emulate throughout my career.

I would also like to thank my committee, whose variety of expertise and feedback have improved the clarity, rigor, and storyline of my work. I appreciate their attention to detail, ensuring that what I present is both understandable and technically accurate. I am thankful for everything I've learned through all the courses I've taken with them, which have allowed me to effectively perform my research. Finally I want to thank them for their questions and comments in my qualifying and comprehensive exams, which prepared me well to discuss and defend my work.

There are also a number of other individuals who have been instrumental in this work. Derrick Yeo served as Co-PI for much of my work, and in addition to providing the flow sensors and communication for testing, his experience and exper-

tise in experimental work enabled each of the tests to get off the ground far quicker and easier than if I had been on my own. He has also been a great encouragement throughout the process, and was always able to empathize with the highs and lows of research. Mark Lopez has been the technical point of contact for my work for several years, and his patience and expertise were essential to the recent work with linear systems. Bernadine Passe, JT Lewis, and Aniket Goel, who were undergrads that worked with me over the past several years, have also played important roles in the work and my personal development as a researcher and leader. My labmates Daigo Shishika and Frank Lagor also played a vital role in my growth at UMD. When I first started at UMD, they were who I turned to when I needed help, either with homework, ideas, or just rising to the challenge of the PhD. Without their understanding and support, my first and most difficult years at UMD would have been much harder. I would also like to thank Elena Shreshtha, who designed, built, and tested the gust generation system I used for the majority of my experiments, and provided support and feedback about my work. Finally, my master's advisor Dr. Kolodziej introduced me to the rigors of research, helped me to realize my desire for a PhD, and played a vital role in my preparation for a doctoral program.

I would also like to thank a number of other colleagues from throughout my education. Everyone in CDCL has played a role in my success. They've helped me to generate and work through ideas, provided valuable feedback regarding research, presentations, and oral exams, and been willing to make time to socialize outside of work. The students and faculty on the 2017 helicopter design team have also been an important part of my development. Through that experience I grew in

my ability to present effectively and defend my ideas, I learned about many of the facets of effective team work, and also learned what a team can accomplish when everyone is fully dedicated. Many other students across the department have also played important roles, providing encouragement, inspiration, and reassurance as I've pursued my research. The staff in the Aerospace Department have also done an excellent job guiding me through the logistics of the degree, making it easy for me to focus on my research. I would also like to thank my advisors and mentors from my bachelor's and master's degrees at RIT, who helped me find subject matter that I'm really excited about and guided me into research.

I am also greatly appreciative of the University of Maryland Vertical Lift Rotorcraft Center of Excellence Army Grant Numbers W911W61120012 and W911W6-17-2-0004, which have generously funded my research for the duration of my time at UMD.

Finally, I want to thank my friends and family, who have provided steadfast support through the whole process, always been happy to listen, encourage, and navigate through all of what life threw at me even beyond the rigors of the PhD program. The UMD cycling team brought many great friendships, taught me the joy and challenge of road racing, and gave me a physical outlet amidst the intellectual intensity of graduate school. Old and new friends were always there for me, and each of my family members had a unique and valuable perspective on all the joys and challenges of research. My wife Anna was my greatest champion, has been dedicated to my success since before the program even began, and cared for and supported me far beyond what was required.

Table of Contents

Dedication	ii
List of Tables	viii
List of Figures	ix
List of Abbreviations	xii
1 Introduction	1
1.1 Motivation	1
1.2 Relation to State of the Art	2
1.3 Contributions of Dissertation	7
1.4 Outline	9
2 Background	10
2.1 Quadrotor Dynamics	10
2.2 Onboard Flow Sensing	12
2.3 Experimental Testbed	14
3 Blade Flapping and Rotor-Pendulum Dynamics	19
3.1 Rotor Dynamics	19
3.2 Rotor-Pendulum Dynamics	23
3.2.1 Full Model	23
3.2.2 Reduced Model	27
3.2.3 Rotor-Pendulum Equations of Motion	29
3.3 Rotor-Pendulum Experimental Results	35
4 Nonlinear Control of Quadrotor Attitude and Position	39
4.1 Attitude Control Design with $SO(3)$	39
4.2 Three Degree-of-Freedom Attitude Simulation	45
4.3 Variable-Gain Algorithm	52
4.4 Position Control Design with $SE(3)$	57
4.5 Six Degree-of-Freedom Position and Attitude Simulation	61

5	Linear Control of Attitude and Position	63
5.1	Model Identification	63
5.2	Controller Design	66
5.3	Controller Optimization	70
6	Quadrotor Control Experimental Results	74
6.1	Nonlinear Controller	74
6.1.1	Three Degree-of-Freedom Attitude Control	74
6.1.2	Six Degree-of-Freedom Position and Attitude Control	80
6.2	Linear Controller	85
7	Conclusion	89
A	Blade-Flapping Equations of Motion	92
B	Cleanflight Software Modifications	100
B.1	Firmware	100
B.1.1	Update for controller	100
B.1.2	Update for flow sensors	101
B.1.3	Notes	103
B.2	Configurator	104
	Bibliography	105

List of Tables

3.1	Rotor-Pendulum Model Parameters	33
4.1	Quadrotor Model Parameters	48
5.1	Stability Derivatives	66
5.2	Handling Qualities Specifications	72
5.3	Control Law Performance	72

List of Figures

2.1	Quadrotor reference frames: \mathcal{I} is the inertial frame, \mathcal{B} is the body frame, \mathcal{U} is the wind frame. The flow probe is situated at point P and \mathbf{u}_1 is aligned with the horizontal component of the wind \mathbf{V}_∞	12
2.2	Flow probe calibration	14
2.3	Experimental quadrotor vehicle with flow probes circled in red	15
2.4	Block diagram of experimental control loop, showing communication between motion capture, Matlab, transmitter (Tx) and flight controller (FC)	16
2.5	Linear fit of rotor thrust to experimental data	17
2.6	Gust generation system consists of a set of eight Dyson fans behind remotely operated blinds	18
3.1	Reference frames of the rotor-pendulum	20
3.2	Blade-flapping free-body diagram	22
3.3	Rotor-pendulum \mathcal{U} and \mathcal{V} frames	24
3.4	Hub force in wind: model/data comparison	29
3.5	Hub moment in wind: model/data comparison	30
3.6	Maximum flap-angle dependency on wind at 12,000 rpm. Upper limit denotes the flap angle requiring a control moment that saturates the thrusts.	30
3.7	Rotor-pendulum free-body diagram	31
3.8	Simulated rotor-pendulum results	35
3.9	Rotor-pendulum stand	36
3.10	Test stand with gust generation system	36
3.11	Model/data comparison for rotor-pendulum experiment	38
4.1	Position and control architecture	40
4.2	20 m/s 1-cosine wind gust profile	49
4.3	20 m/s wind gust response, $\Omega(0) = [0, 0, 0]^T$	49
4.4	20 m/s wind control effort, $\Omega(0) = [0, 0, 0]^T$	50
4.5	Response to $\Omega(0) = [5, 5, 5]^T$, no wind	50
4.6	Control effort for $\Omega(0) = [5, 5, 5]^T$, no wind	51

4.7	Effect of thrust saturation with multiple initial conditions, top: quadrotor angle, middle: maximum motor thrust for the unbounded case, bottom: maximum motor thrust for bounded cases	56
4.8	Simulated position control with and without variable gains. Initial location $(-8, 1, 0)$ to desired location $(0, 0, 10)$. Left: \mathbf{e}_1 , \mathbf{e}_2 and \mathbf{e}_3 positions. Right: Overhead view of \mathbf{e}_1 and \mathbf{e}_2 position.	62
4.9	Simulated position control with and without variable gains. Initial location $(-8, -6, 0)$ to desired location $(0, 0, 10)$. Left: \mathbf{e}_1 , \mathbf{e}_2 and \mathbf{e}_3 positions. Right: Overhead view of \mathbf{e}_1 and \mathbf{e}_2 position.	62
5.1	Chirp data for longitudinal degree of freedom used as input to CIFER [®]	65
5.2	Model-data agreement using stability derivatives identified in CIFER [®]	66
5.3	Model validation against time-series data	67
5.4	Quadrotor linear control architecture	68
5.5	CONDUIT [®] handling qualities window. Level one in blue, level two in pink, level three in red. Triangles and flags indicate the value of the handling quality, green arrows indicate an off-screen value, and the line in Nichols robust stability indicates the value across simultaneous changes in gain and phase.	73
6.1	Quadrotor experimental attitude test stand	75
6.2	Experimental quadrotor response to motor saturation; top: variable gain (solid) and static (dash-dot), middle: static gain motor input, bottom: variable gain motor input	76
6.3	Experimental quadrotor response on attitude stand to 4 m/s gusts in the $\mathbf{e}_1 = -\mathbf{b}_1$ direction	78
6.4	Experimental quadrotor response on attitude stand to 5 m/s gusts in the $\mathbf{e}_1 = -\mathbf{b}_1$ direction	79
6.5	Initial pitch response of each controller for the two different wind speeds and gust frequencies	79
6.6	Experimental quadrotor \mathbf{e}_1 position error in response to 5 s duration 4 m/s gusts in the $-\mathbf{e}_1$ direction. All three controllers use the same outer-loop control, and flow velocity is measured onboard using a custom flow probe.	81
6.7	Experimental quadrotor \mathbf{e}_1 position error in response to 2 s duration 4 m/s gusts in the $-\mathbf{e}_1$ direction. All three controllers use the same outer-loop control, and flow velocity is measured onboard using a custom flow probe.	82
6.8	Experimental quadrotor position response to 5 s duration 4 m/s gusts in the $-\mathbf{e}_1$ direction. All three controllers use the same outer-loop control. Grey area represents desired altitude based on fan output. . .	82
6.9	Experimental quadrotor position response to 2 s duration 4 m/s gusts in the $-\mathbf{e}_1$ direction. All three controllers use the same outer-loop control. Grey area represents desired altitude based on fan output. . .	83

6.10	Horizontal Euclidean-distance error for each controller at the two different gust frequencies. Boxes show 25th and 75th percentiles and median, whiskers show non-outlier values, and additional points show outliers.	83
6.11	Experimental quadrotor \mathbf{e}_1 position error in response to 5 s duration 5 m/s gusts in the $-\mathbf{e}_1$ direction using a linear controller. Flow velocity is measured onboard using a custom flow probe.	86
6.12	Experimental quadrotor \mathbf{e}_1 position error in response to 2 s duration 4 m/s gusts in the $-\mathbf{e}_1$ direction using a linear controller. Flow velocity is measured onboard using a custom flow probe.	86
6.13	Experimental quadrotor position response to 5 s duration 5 m/s gusts in the $-\mathbf{e}_1$ direction using a linear controller. Grey area represents desired altitude based on fan output.	87
6.14	Experimental quadrotor position response to 2 s duration 4 m/s gusts in the $-\mathbf{e}_1$ direction using a linear controller. Grey area represents desired altitude based on fan output.	87
A.1	Aerodynamic forces and angles on a rotor blade	94
A.2	Blade-flapping phase delay in hover	98

List of Abbreviations

A_f	quadrotor frontal area, m^2
C_D	quadrotor body drag coefficient
$C_{D_{RP}}$	rotor-pendulum bluff body drag coefficient
C_{l_α}	airfoil lift slope, $1/rad$
$I_{\bar{r}}$	rotor moment of inertia matrix, kgm^2
I_ℓ	rotor-pendulum rod moment of inertia matrix, kgm^2
I_β	rotor blade moment of inertia, kgm^2
J	quadrotor moment of inertia matrix, kgm^2
\mathbf{M}_{aero}	aerodynamic moment on quadrotor, Nm
\mathbf{M}_{thrust}	thrust moment produced by quadrotor, Nm
M_β	scaled aerodynamic moment on blade
M'_β	aerodynamic moment on blade, Nm
N_b	number of blades per rotor
N_r	number of rotors
N_β	blade static moment, kgm
R	rotation matrix describing quadrotor attitude
T_0	total thrust force produced by quadrotor, N
T_j	thrust force produced by rotor j , N
U_P	perpendicular flow over a rotor blade, m/s
U_T	tangential flow over a rotor blade, m/s
\mathbf{V}_∞	wind velocity, m/s
\mathbf{V}_{probe}	wind velocity measured by flow probe, m/s
\mathbf{X}_{probe}	flow probe position, m
c	blade chord, m
c_m	coefficient relating thrust to torque, N/Nm
$c_{m,c/2}$	blade pitch moment coefficient per unit span at the half chord
d	propeller distance above center of mass, m
dL	differential lift on blade, N
dD	differential drag on blade, N
dr'	blade element length as a fraction of blade length
e	blade hinge offset, m
e'	hinge offset as a fraction of total blade length
\mathbf{e}_R	quadrotor attitude error, rad
\mathbf{e}_v	quadrotor velocity error, m/s
\mathbf{e}_x	quadrotor position error, m
\mathbf{e}_Ω	quadrotor angular rate error, rad/s
\mathbf{f}_{aero}	aerodynamic force on quadrotor, N
\mathbf{f}_{bluff}	bluff body aerodynamic force on quadrotor, N
\mathbf{f}_{ind}	induced drag aerodynamic force on quadrotor, N

\mathbf{f}_{thrust}	quadrotor thrust force, N
k_β	hinge torsional spring constant, Nm/rad
k_R	attitude gain
k_v	velocity gain
k_x	position gain
k_Ω	angular rate gain
k_{λ_x}	Glauert longitudinal inflow gradient
ℓ	quadrotor cross-beam length or rotor-pendulum rod length, m
m	quadrotor mass, kg
m_m	motor mass, kg
$m_{\bar{r}}$	rotor mass, kg
m_ℓ	cross-beam mass, kg
r	displacement along the length of the blade, m
r'	non-dimensional displacement along the length of the blade
\bar{r}	rotor blade length, m
\mathbf{v}	quadrotor velocity, m/s
w	rotor-pendulum rod width, m
\mathbf{x}	quadrotor position, m
$\Delta \mathbf{V}_\infty$	velocity of wind relative to quadrotor, m/s
Ψ	configuration error function
Ω	quadrotor angular velocity, rad/s
α_{eff}	effective angle of attack, rad
α_{geo}	geometric angle of attack, rad
α_{ind}	induced angle of attack, rad
β	blade flap angle, rad
β_0	blade coning angle, rad
β_{1c}	longitudinal blade flapping angle, rad
β_{1s}	lateral blade flapping angle, rad
β_{max}	maximum blade flap angle, rad
γ	Lock number
ζ_{RP}	rotor-pendulum damping coefficient
θ	rotor-pendulum rotation angle along \mathbf{e}_3 , or quadrotor pitch angle, rad
θ_0	blade root angle of attack, rad
θ_{tw}	linear blade twist, rad
λ_0	average inflow ratio
λ_i	linear inflow ratio
μ	advance ratio
ν	quadrotor input moment, Nm
ν_β	blade scaled natural frequency
ρ	density of air, kg/m^3

τ	magnitude of moment from motor torque on rotor-pendulum, Nm
ϕ	rotor-pendulum rotation angle along \mathbf{b}_2 , or quadrotor roll angle, rad
ϕ_D	blade-flapping azimuthal phase delay, rad
ψ	blade azimuth angle, or quadrotor yaw angle, rad
ω_j	angular speed of rotor j , rad/s
ω_n	rotor blade natural frequency, $1/rad$
ω_{β_0}	torsional spring natural frequency, $1/rad$

Chapter 1: Introduction

1.1 Motivation

Quadrotor unmanned aerial systems (UAS) are powerful tools for commercial and military applications, and are often preferred over fixed-wing aircraft and single-main-rotor helicopters due to their mechanical simplicity and ability to hover. The ability to hover and vertically take off and land allows quadrotors to fly in more constrained environments than fixed-wing aircraft, and the use of fixed-pitch rotors that do not require a swashplate mechanism makes quadrotors simpler to build and maintain than single-main-rotor helicopters. Their utility has already been demonstrated in missions such as surveying farmland and aiding in natural disasters [1, 2], and recently a multirotor helicopter was even used to deliver a transplant organ [3].

As they continue to prove their effectiveness in relatively predictable environments, work is ongoing to extend their mission capability, including sensing and perception for unknown environments [4–6], aerobatic behavior [7, 8], hardware failures [9], and transportation of suspended loads [10, 11]. A lingering challenge is flight stability in gusty winds [12], [13]. Quadrotors are particularly vulnerable to wind disturbances due to their small size and low inertia [14]. This research addresses

the challenge of wind through the use of sensing, modeling, and control. I use a model of the aerodynamic interaction between the propellers and wind, paired with onboard flow sensing and feedback control, to improve the stability of quadrotors in unsteady winds, which contributes to the long-term goal of reliable outdoor flight in windy conditions. A goal of this work is to identify the degree of model fidelity required to accurately represent the rigid body system and the moment resulting from wind for use in feedback control.

1.2 Relation to State of the Art

This work addresses flight stability of quadrotors in windy conditions through the addition of flow sensors that are used in the feedback control to directly address the resulting aerodynamic forces and moments. A variety of other methods addressing flight in wind have also been employed, including distributed accelerometers and strain sensing [4], flow sensors for a sense-and-avoid architecture [5], control design specifically for wind turbulence on quadrotors [15], and robust control [16]. Gremillion et al. use distributed accelerometers to directly estimate and subsequently address the forces and moments acting on the vehicle [4], and also show benefits by adding strain sensors to the quadrotor frame in [17]. Berrios et al. use the Control-Equivalent-Turbulence-Input (CETI) model from [18] that identifies motor inputs replicating the effect of actual turbulence to design a gust-rejecting controller. The CETI model is used to optimize gains based on handling qualities criteria in CONDUIT[®] software, resulting in a controller that is inherently robust to distur-

bances containing frequency content typical of turbulent wind [15]. Kun et al. design a linear matrix inequality-based nonlinear adaptive robust controller that is able to guarantee performance under bounded external disturbances such as constant winds and wind gusts [16]. Yeo et al. use flow probes to measure downwash from another quadrotor to estimate its position, then avoid the resulting disturbance to achieve a safe trajectory [5]. The same flow probe hardware is used in this work to identify the magnitude and direction of an oncoming gust, which is addressed directly through the use of aerodynamic force and moment models.

The aerodynamic interaction of quadrotor propellers with wind is modeled here using the blade-flapping phenomena more commonly associated with full-size single-main-rotor helicopters [19]. When a helicopter flies forward, one side of the rotor advances into the oncoming wind, while the other side retreats from the wind, which leads to an increase (resp. decrease) in dynamic pressure and lift on the advancing (resp. retreating) side. The dissymmetry of lift yields a moment on the rotor blades that causes the blades to flap out of the plane of the hub, tilting the rotor plane and imparting a moment on the hub. Many quadrotors are able to maintain acceptable performance without including the effects of blade flapping [7, 8, 20, 21], for example, by using an uncertainty block for a robust controller [16]. However, improving performance in unsteady winds requires an accurate model of the aerodynamic interactions to incorporate into the feedback control of attitude and position, allowing the controller to address the wind gusts directly.

In this work, I seek to model the underlying physics of the blade-flapping effect on quadrotors in order to gain a better understanding of the behavior and

effectively address the forces and moments acting on the vehicle, accounting for the effects of both vehicle translation and external winds. The importance of incorporating blade flapping and other aerodynamic effects into quadrotor models has been recognized previously [22–27]. There are several key differences that separate this work. First, I explicitly use flow sensing to counteract aerodynamic moments on the vehicle, whereas in other prior work, blade flapping and other aerodynamic effects are addressed using velocity measurements, excluding the external airflow. Motivated by the underactuated nature of the quadrotor, wherein the inputs do not allow the vehicle to directly address disturbances in the plane of the rotors, other works focus on translational effects by accounting for the drag-like effects of blade flapping; here I focus on both rotational and translational effects. Furthermore, the majority of other blade-flapping models assume a teetering-rotor [23–25], which does not fully describe typical quadrotor systems including the one used here. Kai et al. [26] and Martin et al. [22] use lumped-parameter models that do not provide a detailed description of the underlying physics of the system. Hoffmann et al. [27] account for the moment produced by blade flapping in addition to the linear force, but not the effect of linear inflow, which in this work was found to be necessary for an accurate model.

The feedback controller described here relies on flow measurements from on-board multi-hole probes, which are used to estimate the aerodynamic forces and moments on the quadrotor. By using flow measurements as well as inertial sensing, the controller can react to the wind before the resulting aerodynamic moment propagates to the quadrotor’s dynamics, which yields benefits compared to relying on

inertial sensing alone. Work validating the benefit of flow feedback was performed previously with a one degree-of-freedom pitching test stand [28]. The flow-sensor package consists of fore and aft, and left and right facing probe pairs connected to a microcontroller unit through flexible tubing (a single fore and aft pressure probe is used for attitude testing). The microcontroller measures pairwise differential pressure, and transmits a digital signal to the flight controller corresponding to the horizontal wind components in the body frame.

Though this work uses flow probes to enhance the performance of a quadrotor, onboard flow probes have also been used for wind characterization, particularly in urban environments. Prudden et al. test the effect of quadrotor inflow on anemometer measurements to establish the required offset of the onboard anemometer relative to the propellers in order to avoid data corruption from the inflow [29]. Bruschi et al. design and investigate the performance of a novel anemometer with two-dimensional sensing, primarily for wind field characterization [30], which also shows potential for use in flow-feedback like that presented here. Thorpe et al. mount a sonic anemometer on a multicopter for use as a mobile wind field characterization system in urban environments, enabling the anemometer to be positioned anywhere in the wind field rather than relying on a static measurement system [31].

The nonlinear flight controller on which I build the flow-feedback design uses feedback linearization and takes advantage of the geometric Lie group $SE(3)$ following [32], with the addition of thrust constraints. Compared to other quadrotor control approaches, such as PID [33, 34], robust [16, 35], adaptive [8, 36], and optimal [37] control, feedback linearization allows the controller to cancel the aerody-

dynamic forces and moments directly. Developing the kinematics on $SE(3)$, which is a compact set representing the configuration space of the orientation and position of a rigid body, avoids the singularities associated with Euler angles and allows for potentially global solutions.

In order to establish stability guarantees for the feedback-linearization controller, rotor thrusts must not saturate. Cao and Lynch [33] and Roza and Maggiore [38] approach thrust saturation using the nested-saturation method from Teel [39], which is designed to address saturation in the case of a chain of integrators. Cao and Lynch [33] bound the roll and pitch angles of the system as well as the thrust by placing limits on system inputs, whereas Roza and Maggiore [38] place the bound on thrust only. Cutler and How [34] address saturation by choosing a trajectory that keeps the system states within the bounds required to avoid thrust saturation. This work uses the method of Pappas et al. [40] to bound the thrust on the system in order to guarantee stability when the feedback linearization alone does not saturate the thrust, and also employs a novel variable-gain algorithm to reduce the stabilization effort when the stabilizing gains would otherwise saturate the motors.

In addition to the nonlinear, variable-gain controller developed in this work, a traditional linear PID controller is also developed to show the benefits of flow sensing on a controller that has been optimized for gust rejection independently of the additional flow-feedback. Typically, gain tuning for quadrotor PID controllers is achieved with a trial-and-error methodology, where nominal gains are chosen based on experience, then tested in flight and adjusted as necessary. Trial and error may

yield an initially unstable platform, but is often successful due to the mechanical simplicity, structural integrity, and low cost of replacement parts for quadrotors. More recently, an approach generally used to evaluate full-scale helicopter stability and performance based on handling qualities metrics has also been pursued [41], which involves first identifying a linear model of the vehicle, then designing a controller such that the vehicle meets the desired handling qualities specifications. A systematic approach that uses CIPHER[®] software [42] for frequency-domain system identification and CONDUIT[®] software [43] for controller gain optimization has been used in [15, 44]. The linear controller presented here also relies on CIPHER[®] and CONDUIT[®] software for model identification and controller optimization, using handling quality specifications informed by [15, 41, 44]. Additionally, I incorporate flow feedback using the sensors described above and linear force and moment models based on system identification techniques as well as blade-flapping analysis.

1.3 Contributions of Dissertation

This dissertation makes contributions to the understanding of quadrotors in wind, and control and sensing methodologies to address gust rejection. A number of papers based on this work have been presented in conferences [45–48], and another has also been submitted to a journal [49]. The response of a quadrotor in wind is studied through a first-principles analysis of the blade-flapping response of a small, stiff propeller in uniform wind. The propeller causes the most complex aerodynamic interaction on the quadrotor; thus, establishing a theoretical understanding of how

propellers on this scale respond to wind is imperative to allow for meaningful treatment of flow measurements. The developed first-principles model is compared to experimental data to identify model parameters and to establish a reduced model that highlights the essential terms of the blade-flapping model. Finally, the accuracy of the model is demonstrated using additional experimental results from a spherical pendulum with a motor and propeller mounted at the end, referred to as a rotor-pendulum. The rotor-pendulum shows the dynamic response of a propeller to a wind gust, which confirms model predictions.

The propeller aerodynamics are included in the model of the quadrotor rigid-body dynamics, yielding a more accurate system description in the presence of wind disturbances, and allowing the aerodynamic effects to be addressed through feedback control. An existing nonlinear geometric feedback-linearization controller is extended to account for the aerodynamic forces and moments predicted by the model, where flow measurements are provided by small, lightweight onboard flow sensors. The controller also employs a variable-gain algorithm that insures thrust bounds are respected while allowing for arbitrarily large stability gains. This ensures that the motors maintain the desired direction of the moment on the vehicle, enabling it to more safely and accurately follow a prescribed trajectory. The merit of adding flow-sensing to the controller is experimentally demonstrated in attitude-only and free-flight configurations.

Parallel to the work with nonlinear control, the benefit of adding flow sensing to a disturbance-rejection optimized linear controller is also investigated. A linear model is developed using frequency-domain system-identification techniques. The

corresponding controller is optimized using desired handling qualities criteria, which characterize stability, performance, and actuator usage. A linear term based on the blade-flapping results is included in the model to address aerodynamic disturbances, yielding improved performance in experimental free-flight gust testing through the use of flow feedback.

1.4 Outline

The outline of this work is as follows. Chapter 2 provides background information to be used throughout the work, describing quadrotor dynamics, the flow sensing system, and the experimental testbed. Chapter 3 develops the blade flapping model that describes the aerodynamic moment on the quadrotor, and also describes modeling and testing with a two degree-of-freedom rotor-pendulum test stand. Chapter 4 develops the inner- and outer-loop controllers for the quadrotor, the thrust saturation algorithm, and provides results from simulation. Chapter 5 describes the linear controller development, including system identification, controller design, and controller optimization. Chapter 6 shows experimental results for each of the controllers designed in this work and discusses the advantages and disadvantages of adding flow sensing to each of the controllers. Finally, Chapter 7 summarizes the dissertation and highlights conclusions drawn from the work.

Chapter 2: Background

2.1 Quadrotor Dynamics

This work investigates attitude and position control of a quadrotor in six degree-of-freedom (DOF) flight. Define inertial reference frame $\mathcal{I} \triangleq (O, \mathbf{e}_1, \mathbf{e}_2, \mathbf{e}_3)$ in an east-north-up orientation and body reference frame $\mathcal{B} \triangleq (O', \mathbf{b}_1, \mathbf{b}_2, \mathbf{b}_3)$ in a forward-left-up orientation. Let the position of the center of mass O' of the quadrotor relative to the inertial reference frame be given by $\mathbf{x} \in \mathbb{R}^3$ and the orientation of the quadrotor relative to the inertial frame be represented by the rotation matrix $R \in SO(3)$, where $SO(3)$ is the special orthogonal group. The full state of the quadrotor is represented by $\mathbf{x} \times R \in SE(3)$, where $SE(3)$ is the special Euclidean group. The translational velocity of the quadrotor relative to the inertial frame is $\mathbf{v} = \dot{\mathbf{x}}$, and the angular velocity of the quadrotor relative to the inertial frame expressed as components in the body frame is $\boldsymbol{\Omega} = [p, q, r]^T$. Bold capital letters denote vectors in body frame components, lowercase bold letters denote vectors in inertial components, a \mathcal{B} superscript represents a body-frame derivative, and no superscript indicates inertial-frame derivatives. Using rigid-body kinematics and

Euler's laws, the translational and rotational dynamics are

$$\begin{aligned}
\dot{\mathbf{x}} &= \mathbf{v} \\
m\dot{\mathbf{v}} &= -mg\mathbf{e}_3 + \mathbf{f}_{thrust} + \mathbf{f}_{aero} \\
\dot{R} &= R\hat{\Omega} \\
J\dot{\Omega} &= -\hat{\Omega}J\Omega + \mathbf{M}_{thrust} + \mathbf{M}_{aero},
\end{aligned} \tag{2.1}$$

where m is the mass of the quadrotor, g is the gravitational force, $\mathbf{f}_{thrust} = f_{thrust}\mathbf{b}_3$ is the total thrust generated by the vehicle, and \mathbf{f}_{aero} is the aerodynamic drag force on the vehicle from both the propellers' induced drag and the drag on the body. J is the moment of inertia matrix, assumed to be diagonal due to the symmetry of the quadrotor. Moment \mathbf{M}_{thrust} is due to propeller thrusts and \mathbf{M}_{aero} is the aerodynamic moment due to interaction between the rotors and the wind. (The wedge operator $\hat{\cdot}$ denotes the matrix representation of the cross product, such that for any vectors \mathbf{x} and \mathbf{y} in \mathbb{R}^3 , $\hat{\mathbf{x}}\mathbf{y} = \mathbf{x} \times \mathbf{y}$. The vee operator \vee extracts the corresponding vector in \mathbb{R}^3 from a skew-symmetric matrix.)

The quadrotor vehicle is modeled as two perpendicular uniform beams of length ℓ attached at their centers to create four arms, with one rotor located at the end of each arm, as in Fig. 2.1. Rotors are located at position $d\mathbf{b}_3$ above each arm, where $d \ll \ell/2$. The moment of inertia is $J = \text{diag}\{m_\ell\ell^2/12+2m_m\ell^2, m_\ell\ell^2/12+2m_m\ell^2, m_\ell\ell^2/6+4m_m\ell^2\}$, where m_ℓ is the mass of each cross beam of the quadrotor, ℓ is the motor-to-motor length of each cross beam, and m_m is the mass of each motor. Rotors are assumed to spin about the \mathbf{b}_3 axis, with rotation directions shown in Fig. 2.1. This choice of rotor rotational directions results in zero net torque in

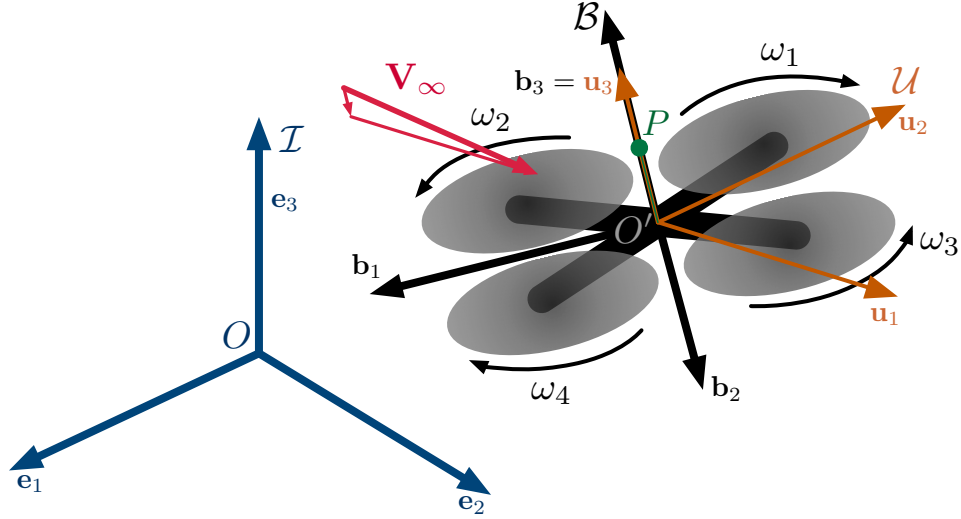


Figure 2.1: Quadrotor reference frames: \mathcal{I} is the inertial frame, \mathcal{B} is the body frame, \mathcal{U} is the wind frame. The flow probe is situated at point P and \mathbf{u}_1 is aligned with the horizontal component of the wind \mathbf{V}_∞

the \mathbf{b}_3 direction under nominal conditions with each rotor operating at the same speed and no outside aerodynamic forces.

2.2 Onboard Flow Sensing

The multi-hole probe P is positioned above the quadrotor's center of mass O' to reduce the effect of the vehicle drag and propeller inflow on the probe, and so the quadrotor's rotation must be taken into account when determining the wind velocity at O' . The vector measured by the flow probe is \mathbf{V}_{probe} , the inertial wind velocity in body-frame components is \mathbf{V}_∞ , the quadrotor translational velocity in body components is \mathbf{V} , the location of the probe relative to the center of mass is \mathbf{X}_{probe} , and the contribution of the quadrotor rotational velocity is $\hat{\Omega}\mathbf{X}_{probe}$. The

value measured by the probe is

$$\mathbf{V}_{probe} = \mathbf{V}_\infty - \mathbf{V} - \hat{\boldsymbol{\Omega}}\mathbf{X}_{probe}. \quad (2.2)$$

Let $\Delta\mathbf{V}_\infty = \mathbf{V}_\infty - \mathbf{V} = \mathbf{V}_{probe} + \hat{\boldsymbol{\Omega}}\mathbf{X}_{probe}$ denote the velocity of wind at the center of mass of the quadrotor. Note, Eq. (2.2) assumes the probe measures all three vector components of the wind in the body frame; in the experimental testbed, only the \mathbf{b}_1 and \mathbf{b}_2 components are measured.

The flow instrumentation utilizes custom-built pressure probes, highlighted in Fig. 2.3, that provide information through differential-pressure measurements to sense wind speeds up to 8 m/s. The flow probes are made aluminum tubes, bent at a 90 degree angle and set opposing each other. The airspeed is related to the differential pressure through by the following equations [5]:

$$\begin{aligned} u &= L_u \sqrt{\frac{2L_b(P_2 - P_1)}{\rho}} \\ v &= L_v \sqrt{\frac{2L_b(P_4 - P_3)}{\rho}}, \end{aligned} \quad (2.3)$$

where scaling factors L_u and L_v are determined by calibration, and L_b accounts for gravity and unit conversion. Figure 2.2 shows the accuracy of the calibrated flow probes to a ground-truth Testo 405i hot-wire anemometer. Values at high wind speed show good agreement, and low speed values where the onboard probe is less accurate are acceptable because low wind speeds will yield only a small disturbance on the quadrotor. In addition to magnitude accuracy, Yeo et al. [5] also showed directional accuracy with less than 15% error.

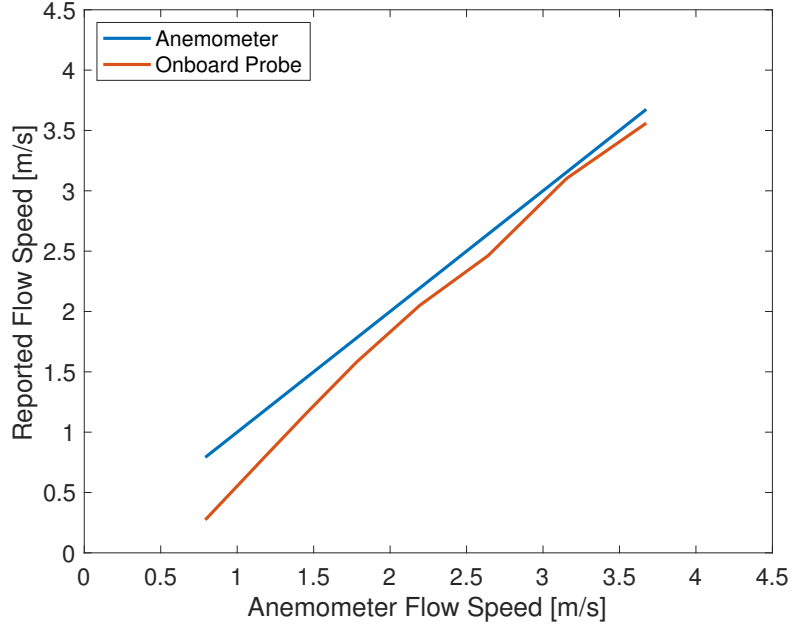


Figure 2.2: Flow probe calibration

2.3 Experimental Testbed

Performance of the developed controller is tested experimentally with the quadrotor in Fig. 2.3, using motion capture feedback for position and heading control, sensing from the IMU on the onboard flight-controller for inner-loop attitude control, and flow sensing to inform aerodynamic terms. The quadrotor is a 210 mm carbon fiber frame with a Matek F405 STD flight controller and Matek FCHUB-6S power distribution board. Gemfan 5030 propellers are mounted to EMAX RS-2205 motors that are controlled by EMAX Lightning 20A ESCs. The quadrotor runs Cleanflight open-source software that has been modified to support flow measurement feedback and run the feedback-linearization controller described in this work. Data from the quadrotor is collected on a micro SD card at a rate of 250 Hz using Cleanflight’s Blackbox feature.



Figure 2.3: Experimental quadrotor vehicle with flow probes circled in red

Implementing the controller and sensors on the Cleanflight software requires a number of modifications. Converting the standard PID controller to the feedback-linearization controller described in this work involves adding the blade-flapping solution to produce the aerodynamic moment, as well as updating the motor inputs to reflect the feedback linearization inputs. The IMU file is also modified to include functions that operate on rotation matrices for use in the feedback linearization algorithm. Additionally, the mixer file relating transmitter input to motor input is updated to reflect the desired thrust input, as identified in Fig. 2.5. Interfacing with the flow sensors requires significant updates to the Cleanflight software. Dedicated flow files are created to define communication protocols and conversions from the digital signal to flow speed. Additionally, parameters, features, sensors, and tasks are added to the Cleanflight software to support serial communication with the flow sensors. Finally, the configurator graphical user interface is also updated, allowing

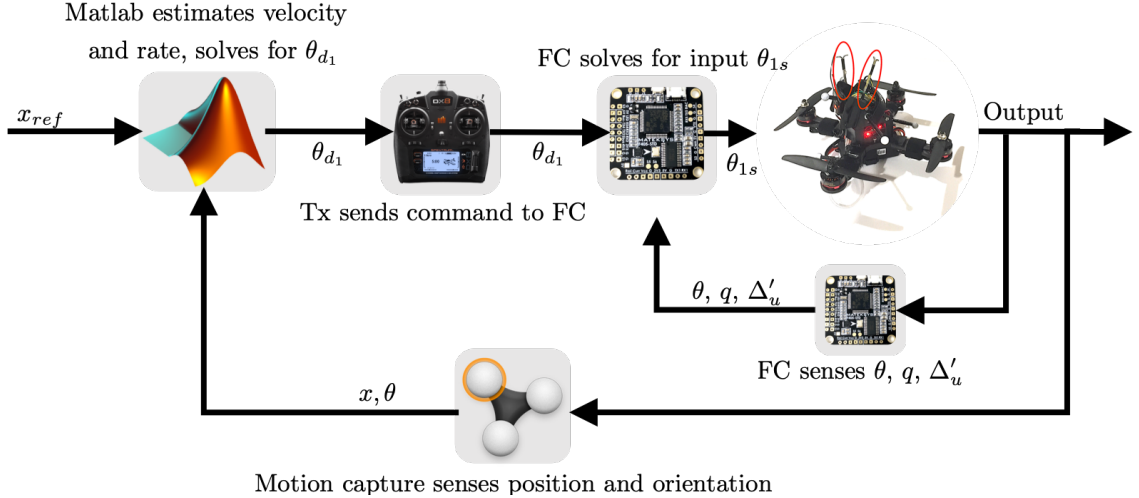


Figure 2.4: Block diagram of experimental control loop, showing communication between motion capture, Matlab, transmitter (Tx) and flight controller (FC)

the user to engage with the flow sensing functionality. A detailed account of the modifications to the Cleanflight software are listed in Appendix B.

Position and attitude data are collected in an OptiTrack motion capture facility and streamed to the outer-loop controller running in Matlab as shown in Fig. 2.4. Errors, thrust, and desired body axes are computed and passed to the flight controller through the trainer port of an RC transmitter, where the custom Cleanflight software incorporates flow measurements to solve for the final desired axes and produce the prescribed thrust at each motor. For attitude-only experiments, only the inner loop in Fig. 2.4 is automated, with the thrust set by the user to compensate for the vehicle weight, and other inputs left at their desired nominal stick input values.

A teetering test-stand was built to enable correlation of the PWM signal provided to the motors to the resulting thrust. On the teetering stand, one side is

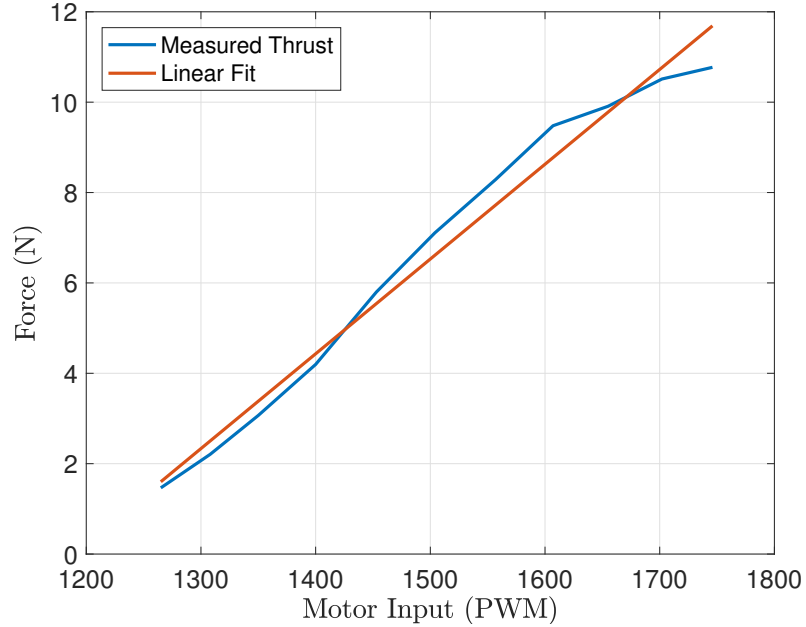


Figure 2.5: Linear fit of rotor thrust to experimental data

attached to the quadrotor, and the other rests on a scale. The transmitter PWM and corresponding gram-force on the scale produce the relationship in Fig. 2.5 with a slope of 0.021 N/PWM, after adjusting for the number of rotors and converting to Newtons.

Gust-rejection testing is performed in the motion-capture facility using the gust generator system in Fig. 2.6, consisting of a set of DysonTM fans placed behind remotely actuated blinds. Blinds are required for the system to produce gust inputs because the transient response produced by modulating the power of the fans is not fast enough to represent gust-like inputs desired for this work. The blinds are controlled by an Arduino to produce a desired profile programmed into LabVIEW software. Square-wave inputs are best suited for the blinds because the blinds redirect the flow rather than affecting the wind speed itself, meaning that a gradual



Figure 2.6: Gust generation system consists of a set of eight Dyson fans behind remotely operated blinds

input to the blinds does not lead to a gradual change in wind speed. During each of the tests, wind speed is established by an independent Testo 405i anemometer prior to testing in addition to using the onboard flow probes. Additional information on the gust generator system is available in [50].

Chapter 3: Blade Flapping and Rotor-Pendulum Dynamics

Addressing flight stability in gusts begins with understanding the dynamic response of the quadrotor to wind disturbances. This is done by modeling the blade-flapping response of the quadrotor propellers to oncoming wind, which is then used to calculate forces and moments at the hub of the propeller. The models are validated experimentally by comparing to a rotor-pendulum test-stand subjected to a wind gust. This work was presented in the 2016 ASME Dynamic Systems and Control Conference [45].

3.1 Rotor Dynamics

This work utilizes a rotor-pendulum to investigate the effect of wind on a small, stiff propeller. The rotor-pendulum is a variation of the gyro-pendulum, which is a spherical pendulum with a rapidly spinning mass on the mobile end that causes the system to precess and nutate. Figure 3.1 shows the rotor-pendulum system: a gyro-pendulum with the spinning mass replaced by a propeller. Consider inertial reference frame $\mathcal{I} \triangleq (O, \mathbf{e}_1, \mathbf{e}_2, \mathbf{e}_3)$ and intermediate frame $\mathcal{A} \triangleq (O, \mathbf{a}_1, \mathbf{a}_2, \mathbf{a}_3)$, where $\mathbf{a}_3 = \mathbf{e}_3$ and $\mathbf{a}_1 \cdot \mathbf{e}_1 = \cos \theta$. Spherical frame $\mathcal{B} \triangleq (O, \mathbf{b}_1, \mathbf{b}_2, \mathbf{b}_3)$ satisfies $\mathbf{b}_2 = \mathbf{a}_2$ and $\mathbf{b}_1 \cdot \mathbf{a}_1 = \cos \phi$. The hub frame is $\mathcal{C} \triangleq (O', \mathbf{c}_1, \mathbf{c}_2, \mathbf{c}_3)$, where $\mathbf{c}_3 = \mathbf{b}_3$ and $\mathbf{c}_1 \cdot \mathbf{b}_1 = \cos \psi$. Let

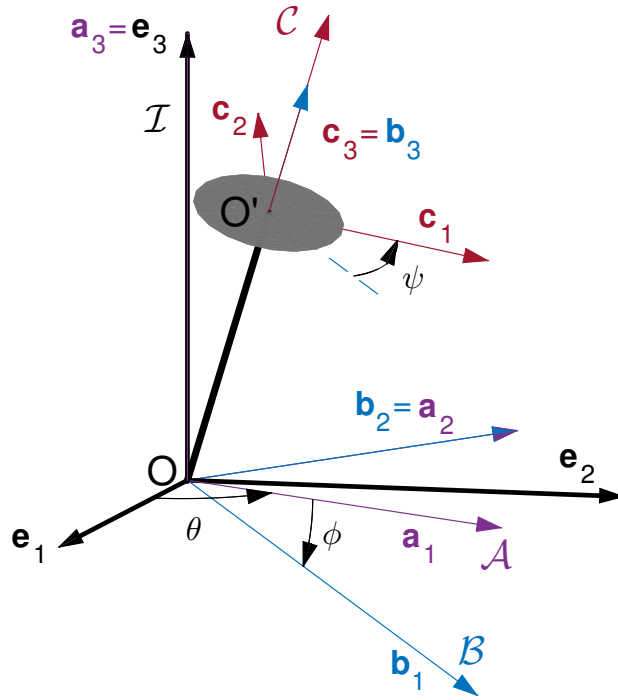


Figure 3.1: Reference frames of the rotor-pendulum

N_b represent the number of propeller blades and the superscript (n) , where $n = 1, 2$, or 3 , denote the blade index, so that frame $\mathcal{D}^{(n)} \triangleq (H^{(n)}, \mathbf{d}_1^{(n)}, \mathbf{d}_2^{(n)}, \mathbf{d}_3^{(n)})$ has origin at the blade hinge, and rotates about \mathbf{c}_2 by the flap-angle β . (The blade index (n) is included only where needed for clarity.) Let r denote the displacement along the length of the blade of a point P with respect to O' , and dr be the differential position. The differential forces, moments, and mass are denoted $Fdr \triangleq dF$, $Mdr \triangleq dM$, and $m dr \triangleq dm$, where the quantities F , M , and m are each measured per unit length.

The blade-flap angle is derived under the assumption that O' is fixed in inertial space and the blade rotates around the hub in the \mathbf{c}_3 direction at a constant rate ω such that $\omega t = \psi$, where ψ is the blade azimuth. (The assumption that O' is fixed is relaxed later in the analysis of the rotor-pendulum system.) Let $\mathbf{r}_{P/O'}$

denote the position of blade-element P with respect to O' ; $\mathcal{I}\mathbf{v}_{P/O'} = \frac{\mathcal{I}d}{dt}(\mathbf{r}_{P/O'})$ and $\mathcal{I}\mathbf{a}_{P/O'} = \frac{\mathcal{I}d}{dt}(\mathcal{I}\mathbf{v}_{P/O'})$ denote the inertial kinematics. Figure 3.2 denotes the hinge offset $e = \|\mathbf{r}_{H/O'}\|$; $R - e = \|\mathbf{r}_{Q/H}\|$ is the length of the portion of the blade beyond the hinge and $r - e = \|\mathbf{r}_{P/H}\|$ is the distance from the hinge to point P . Let $S_\beta = \sin \beta$ and $C_\beta = \cos \beta$. Using the cross product with the angular velocity $\mathcal{I}\boldsymbol{\omega}^c = \omega\mathbf{c}_3$ ($\mathcal{I}\boldsymbol{\omega}^c = \dot{\theta}\mathbf{a}_3 + \dot{\phi}\mathbf{b}_2 + \omega\mathbf{c}_3$, where $\dot{\theta} = \dot{\phi} = 0$ due to the fixed hub) to differentiate the unit vectors \mathbf{c}_1 and \mathbf{c}_2 , the inertial kinematics are

$$\mathbf{r}_{P/O'} = (e + (r - e)C_\beta)\mathbf{c}_1 + (r - e)S_\beta\mathbf{c}_3 \quad (3.1)$$

$$\begin{aligned} \mathcal{I}\mathbf{v}_{P/O'} &= -(r - e)\dot{\beta}S_\beta\mathbf{c}_1 \\ &+ (e + (r - e)C_\beta)\omega\mathbf{c}_2 + (r - e)\dot{\beta}C_\beta\mathbf{c}_3 \end{aligned} \quad (3.2)$$

$$\begin{aligned} \mathcal{I}\mathbf{a}_{P/O'} &= [-(r - e)(\ddot{\beta}S_\beta + \dot{\beta}^2C_\beta) - (e + (r - e)C_\beta)\omega^2]\mathbf{c}_1 \\ &- 2(r - e)\dot{\beta}\omega S_\beta\mathbf{c}_2 + [(r - e)\ddot{\beta}C_\beta - (r - e)\dot{\beta}^2S_\beta]\mathbf{c}_3. \end{aligned} \quad (3.3)$$

Figure 3.2 shows the differential forces on the blade element at P : dF_1 is the tension force; dF_2 is the sum of the lift and drag components in the \mathbf{c}_1 - \mathbf{c}_2 plane; dF_3 is the sum of the lift and drag components in the \mathbf{c}_1 - \mathbf{c}_3 plane; and gdm is the weight. Assuming the forces between the hub and the hinge are negligible, the total differential force acting on a blade element is

$$\begin{aligned} d\mathbf{F}_P^{(n)} &= (-dF_1C_\beta - dF_3S_\beta)\mathbf{c}_1 + (-dF_2)\mathbf{c}_2 \\ &+ (-dF_1S_\beta + dF_3C_\beta - gdm)\mathbf{c}_3. \end{aligned} \quad (3.4)$$

Equating the mass times the acceleration (3.3) with the force (3.4) in the \mathbf{c}_3 direction according to Newton's second law yields the differential tension force

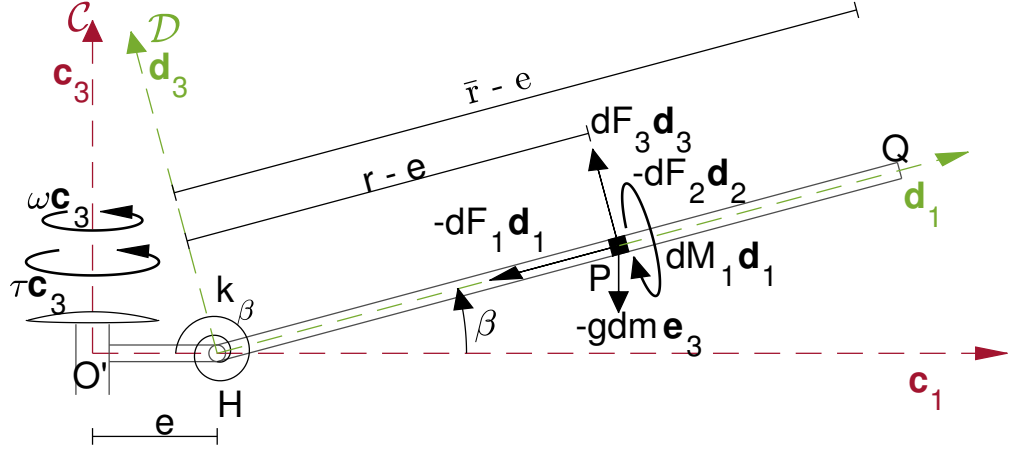


Figure 3.2: Blade-flapping free-body diagram

dF_1 , which is used in the angular-momentum form of Newton's second law in the sequel. The angular momentum of the point P with respect to O' is $\mathcal{I}_{\mathbf{h}_{P/O'}} = \mathbf{r}_{P/O'} \times (dm^{\mathcal{I}} \mathbf{v}_{P/O'})$, i.e.,

$$\begin{aligned}
 \mathcal{I}_{\mathbf{h}_{P/O'}} &= dm[-(r-e)eS_{\beta}\omega - \frac{1}{2}(r-e)^2S_{2\beta}\omega]\mathbf{c}_1 \\
 &\quad + dm[-(r-e)^2\dot{\beta} - (r-e)eC_{\beta}\dot{\beta}]\mathbf{c}_2 \\
 &\quad + dm[(e+(r-e)C_{\beta})^2\omega]\mathbf{c}_3.
 \end{aligned} \tag{3.5}$$

The above equations are used to derive the blade-flapping equations for a rotor with a fixed hub, using the angular-momentum form of Newton's second law in Appendix A to provide continuity and consistent nomenclature. Additional blade-flapping derivations can be found in [51] and [52] by Chen, which include development for a dynamic hub.

A goal of this work is to use the simplest physics-based model which sufficiently captures the behavior of the system. As such, this development begins with the equations for a fixed hub. A linear inflow model is added to the fixed-hub equations in order to correctly predict forces and moments as identified in experiments. Terms

related to the rolling and pitching of the hub have not been added, though they may be included if necessary for future applications.

3.2 Rotor-Pendulum Dynamics

3.2.1 Full Model

Figure 3.3 introduces two additional reference frames to describe the aerodynamic forces, which depend on the magnitude and direction of the wind as well as the phase delay of the propeller. Let \mathbf{V}_∞ represent the velocity of the wind in the inertial frame and $\Delta\mathbf{v}_\infty$ represent the velocity of the wind experienced by an observer at point O' in the spherical frame (due to the combination of the wind and the motion of point O'). Define the wind frame $\mathcal{U} \triangleq (O', \mathbf{u}_1, \mathbf{u}_2, \mathbf{u}_3)$, where $\mathbf{u}_3 = \mathbf{b}_3$ and \mathbf{u}_1 is the direction of the component of $\Delta\mathbf{v}_\infty$ in the plane perpendicular to \mathbf{b}_3 . Also consider the phase-delay frame $\mathcal{V} \triangleq (O', \mathbf{v}_1, \mathbf{v}_2, \mathbf{v}_3)$, where $\mathbf{v}_3 = \mathbf{u}_3$ and $\mathbf{v}_1 \cdot \mathbf{u}_1 = \cos \phi_D$ (\mathbf{v}_2 corresponds to the direction of maximum flapping).

The hub forces in the plane perpendicular to \mathbf{b}_3 , i.e., $\mathbf{F}_{O'}^\perp \triangleq \mathbf{F}_{O'} - (\mathbf{F}_{O'} \cdot \mathbf{b}_3)\mathbf{b}_3$, are a combination of the tilt of the thrust vector and the drag forces on the blades. Starting from (3.4), and averaging the force over an entire revolution, the planar hub force is

$$\mathbf{F}_{O'}^\perp = \frac{N_b}{2\pi} \int_0^{2\pi} \left[\int_0^{\bar{r}} (-dF_2 \mathbf{c}_2 \cdot \mathbf{u}_1) \mathbf{u}_1 - \int_e^{\bar{r}} S_\beta dF_3 \mathbf{c}_1 \right] d\psi, \quad (3.6)$$

where $\mathbf{c}_2 \cdot \mathbf{u}_1 = -S_\psi$. While not practical for online calculation, (3.6) is solved symbolically in order to achieve high accuracy. Using two blades in both simulation and

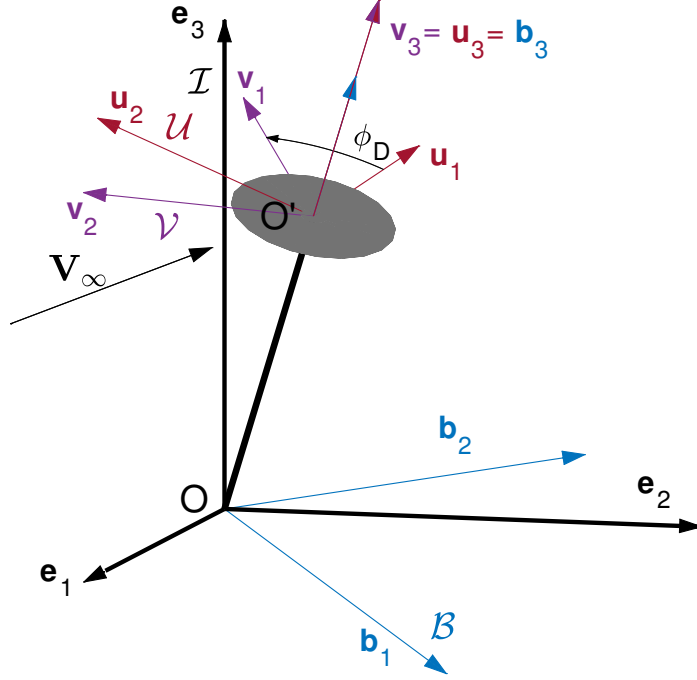


Figure 3.3: Rotor-pendulum \mathcal{U} and \mathcal{V} frames

experiment, the differential blade tension forces $dF_1^{(1)}$ and $dF_1^{(2)}$ cancel out because $dF_1^{(1)} = -dF_1^{(2)}$, leaving only the dF_2 and dF_3 components. The dF_3 component is calculated from GemFan 5030 propeller experimental thrust data at a range of speeds; the dF_2 component arises from induced drag.

The dF_3 term in (3.6) is converted from the \mathcal{C} frame to the \mathcal{V} frame, which does not rotate with ψ . From (A.18), β responds as a once-per-revolution sinusoid $\beta(\psi) = \beta_0 + \beta_{max}S(\psi - \phi_D)$. Making the small-angle assumption based on the calculated magnitude of β_{max} , (3.6) becomes

$$\begin{aligned} \mathbf{F}_{O'}^\perp = & \frac{N_b}{2\pi} \int_0^{2\pi} \left[\int_0^{\bar{r}} (dF_2 S_\psi) \mathbf{u}_1 - (\beta_0 + \beta_{max} S(\psi - \phi_D)) \right. \\ & \left. \times \int_e^{\bar{r}} (C(\psi - \phi_D) \mathbf{v}_1 + S(\psi - \phi_D) \mathbf{v}_2) dF_3 \right] d\psi. \end{aligned} \quad (3.7)$$

Due to the nature of the sinusoidal terms, the force along \mathbf{v}_1 resulting from dF_3 in (3.7), as well as all forces due to β_0 , integrate to zero over one full rotation, leaving only the \mathbf{v}_2 component.

Quadrotors experience high induced drag, which results from the lift force and induced angle of attack (both found in (A.8)). The specific value for induced angle of attack used in (4.39) is found by applying (A.9) to (A.8), then neglecting $\omega\beta^*(r-e)$ and $\mu\omega\bar{r}S_\beta C_\psi$ (because β^* and β are small), which yields $\alpha_{ind} = \arctan(\lambda_i/(r'+\mu S_\psi))$. Induced drag is the only non-negligible component of differential force dF_2 , thus

$$dF_2 = \frac{1}{2}\rho(\omega r - (\mathbf{c}_2 \cdot \mathbf{u}_1)(\Delta\mathbf{v}_\infty \cdot \mathbf{u}_1))^2 c C_{\ell_\alpha} \alpha_{eff} S_{\alpha_{ind}} dr. \quad (3.8)$$

There also exist bluff-body drag forces acting in the direction of the wind on the swept area of the rotor and the pendulum rod. The bluff force on each component is

$$\begin{aligned} \mathbf{F}_{\bar{r}bluff} &= \frac{1}{2}\rho\|\Delta\mathbf{v}_\infty\|^2 \left(\Delta\hat{\mathbf{v}}_\infty \cdot \mathbf{b}_3 \pi \bar{r}^2 \right) C_{DRP} \Delta\hat{\mathbf{v}}_\infty, \\ \mathbf{F}_{\ell bluff} &= \frac{1}{2}\rho\|\Delta\mathbf{v}_\infty\|^2 \left(\Delta\hat{\mathbf{v}}_\infty \cdot \mathbf{u}_1 w \ell \right) C_{DRP} \Delta\hat{\mathbf{v}}_\infty, \end{aligned} \quad (3.9)$$

where $\Delta\hat{\mathbf{v}}_\infty = \Delta\mathbf{v}_\infty/\|\Delta\mathbf{v}_\infty\|$, w is the rod width, ℓ is the rod length, and the drag coefficient $C_{DRP} = 1.28$ [53] is taken by approximating each component as a three-dimensional flat plate.

The moment on the hub in the plane perpendicular to \mathbf{b}_3 , i.e., $\mathbf{M}_{O'}^\perp \triangleq \mathbf{M}_{O'} - (\mathbf{M}_{O'} \cdot \mathbf{b}_3)\mathbf{b}_3$, is derived from the spring, hinge offset, and the pitching moment of the airfoil. The lift and weight forces do not transmit a moment to the hub due to the nature of the hinge, leading to their absence in the following moment equation

as compared to (A.2). The moment in the plane perpendicular to \mathbf{b}_3 is

$$\begin{aligned} \mathbf{M}_{O'}^\perp &= \frac{N_b}{2\pi} \int_0^{2\pi} - \left[k_\beta \beta + e S_\beta \int_e^{\bar{r}} dF_1 \right] \mathbf{c}_2 d\psi \\ &+ \frac{N_b}{2\pi} \int_0^{2\pi} \int_0^{\bar{r}} (dM_1 \mathbf{c}_1 \cdot \mathbf{u}_2) \mathbf{u}_2 d\psi, \end{aligned} \quad (3.10)$$

where $\mathbf{c}_1 \cdot \mathbf{u}_2 = S_\psi$. Similar to (3.6), (3.10) is solved symbolically in order to achieve high accuracy.

Converting the first half of (3.10) from the rotating \mathcal{C} frame to the \mathcal{V} frame as in (3.6) and applying the small angle assumption to β yields

$$\begin{aligned} \mathbf{M}_{O'}^\perp &= \frac{N_b}{2\pi} \int_0^{2\pi} \left[\left(k_\beta + e \int_e^{\bar{r}} dF_1 \right) \right. \\ &\quad \left. \times (\beta_0 + \beta_{max} S_{(\psi-\phi_D)}) (S_{(\psi-\phi_D)} \mathbf{v}_1 - C_{(\psi-\phi_D)} \mathbf{v}_2) \right] d\psi \\ &+ \frac{N_b}{2\pi} \int_0^{2\pi} \int_0^{\bar{r}} (dM_1 \mathbf{c}_1 \cdot \mathbf{u}_2) \mathbf{u}_2 d\psi. \end{aligned} \quad (3.11)$$

The moment along \mathbf{v}_2 from the first half of (3.11) and the moment due to β_0 integrate to zero over one full rotation, leaving only the \mathbf{v}_1 component.

The centrifugal or tension differential force $dF_1 = r\omega^2 dm$ is found by equating the \mathbf{c}_1 components in (3.3) and (3.4), applying small-angle simplifications to trigonometric terms involving β , and assuming that $\dot{\beta}$ and $\ddot{\beta}$ are negligible in comparison to ω .

The differential moment dM_1 on the hub due to the airfoil pitching is calculated by approximating the shape of the Gemfan 5030 airfoil as a thin, cambered 4-digit 5502 NACA airfoil, and using the calculation for this shape to determine the coefficient of blade pitching moment [54, pp. 275-278] and [55, pp. 113-114]. The blade-pitching differential moment is

$$dM_1 = \frac{1}{2} \rho (\omega r - (\mathbf{c}_2 \cdot \mathbf{u}_1) (\Delta \mathbf{v}_\infty \cdot \mathbf{u}_1))^2 c^2 c_{m,c/2} dr, \quad (3.12)$$

where $c_{m,c/2}$ is the blade pitch moment coefficient per unit span at the half chord.

3.2.2 Reduced Model

In order to reduce the complexity and number of parameters while retaining the essential behavior of the system, we neglect the tilt of the thrust vector $S_\beta dF_3$, the moment due to hinge offset $eS_\beta dF_1$, and the airfoil pitching moment dM_1 , as they have a relatively small overall effect (for the parameter values used here), as compared to the induced drag force dF_2 and the hinge spring moment $k_\beta\beta$. Thus, (3.7) and (3.11) become

$$\mathbf{F}_{O'}^\perp \approx \frac{N_b}{2\pi} \int_0^{2\pi} \int_0^{\bar{r}} dF_2 S_\psi \mathbf{u}_1 d\psi, \quad (3.13)$$

and

$$\mathbf{M}_{O'}^\perp \approx \frac{N_b}{2\pi} \int_0^{2\pi} k_\beta \beta_{max} S_{(\psi-\phi_D)}^2 \mathbf{v}_1 d\psi. \quad (3.14)$$

The induced angle of attack in the induced drag (4.39) is also simplified by assuming uniform inflow (which has shown to be sufficiently accurate for this term, compared to the flap angles where linear inflow was necessary), using the mean velocity of the blade, neglecting the change in velocity due to wind, and assuming the angle is small, such that $\alpha_{ind} = 2\lambda_0$. Additionally, we assume a constant effective angle of attack $\alpha_{eff} = \theta_0 + (3/4)\theta_{tw} - \alpha_{ind}$, which eliminates the need for online multivariable integration, and yields the following equations from (3.13)–(3.14):

$$\mathbf{F}_{O'}^\perp \approx \frac{N_b}{4} \rho c C_{l_\alpha} \alpha_{eff} S_{\alpha_{ind}} \omega \bar{r}^2 (\Delta \mathbf{v}_\infty \cdot \mathbf{u}_1) \mathbf{u}_1, \quad (3.15)$$

and

$$\mathbf{M}_{O'}^\perp \approx \frac{N_b}{2} k_\beta \beta_{max} \mathbf{v}_1. \quad (3.16)$$

Furthermore, the blade-flapping equations (A.15–A.17) are simplified by assuming $e' = 0$ (no hinge offset) and ignoring all β multipliers on the right-hand side as each of these are small and contribute little to the solution. The simplifications reduce (A.15)–(A.17) to a concise set of equations that is no longer implicit. In fact, with explicit flapping equations and no other parameters dependent on β_0 , we no longer need to calculate β_0 , and the remaining parameters are

$$\beta_{1c} \approx \frac{-\gamma}{8(\nu_\beta^2 - 1)} \lambda_0 k_{\lambda_x}, \quad (3.17)$$

$$\beta_{1s} \approx \frac{\mu \gamma}{4(\nu_\beta^2 - 1)} \left(\frac{4}{3} \theta_0 + \theta_{tw} - \lambda_0 \right). \quad (3.18)$$

Using forces and moments from (3.6), (3.10), (3.13), and (3.14), both the full and reduced models are compared to experimental force and moment data from a motor and propeller in a wind tunnel, taken by an ATI Nano 17 six-axis Force-Torque transducer, with flow speed measurements provided by a Thomas Scientific Traceable hot wire anemometer. Choosing $e' = 0.1$ and $k_\beta = 3$ Nm/rad yields the results in Figs. 3.4 and 3.5, which show agreement between model and experiment data in both the magnitude and direction of forces at a propeller speed of 8000 rpm over a range of wind speeds. The reduced model varies only slightly from the full model, and remains well matched to the experimental results. Though the simplifications eliminate all forces on the hub in the \mathbf{b}_2 direction in the model, the measured force is small compared to that in the \mathbf{b}_1 direction, and may be ignored. The full model of the force in the \mathbf{b}_1 direction overpredicts the magnitude of the force at this particular wind speed due to the difficulty of fitting both forces and moments over a range of wind and propeller speeds. Thus, ignoring terms for the reduced

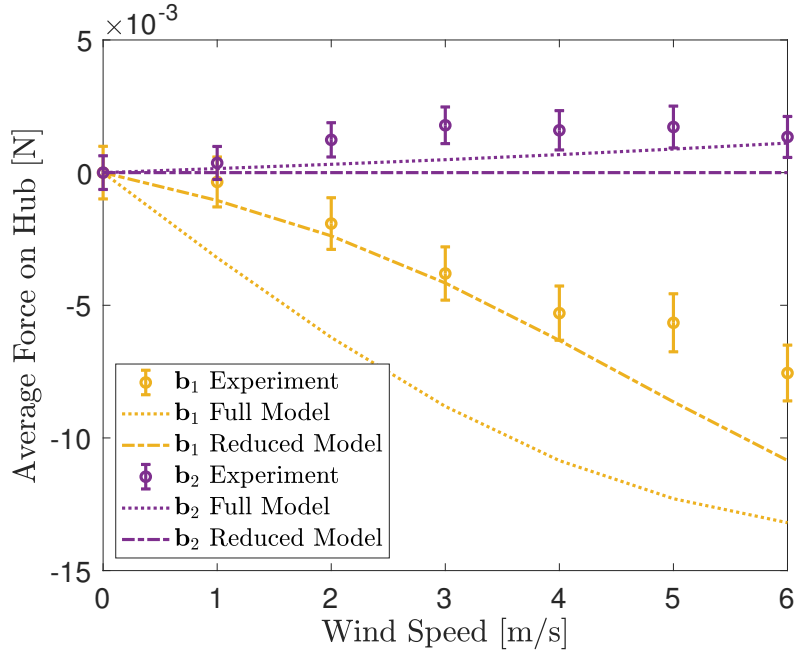


Figure 3.4: Hub force in wind: model/data comparison

model yields a closer fit to experimental data for the \mathbf{b}_1 force. This experimentally validated model produces estimates of the moment on the propeller for wind speeds up to 6 m/s. Higher wind speeds have been explored using flap-angle visualization on wind-tunnel data, yielding Fig. 3.6, which shows flap angles of over one degree for wind speeds above 15 m/s. The β upper limit shown on the plot represents the flap angle that produces a moment sufficient to saturate the motors when addressed in the feedback-linearization controller described in the sequel.

3.2.3 Rotor-Pendulum Equations of Motion

The simplified forces and moments derived above are applied to the rotor-pendulum in Fig. 3.7, where $\mathbf{F}_{O'} = \mathbf{F}_{O'}^\perp + C_\beta dF_3 \mathbf{c}_3$ and $\mathbf{M}_{O'} = \mathbf{M}_{O'}^\perp + \tau \mathbf{c}_3$, and τ is the magnitude of the moment produced by motor torque. Figure 3.7 also shows

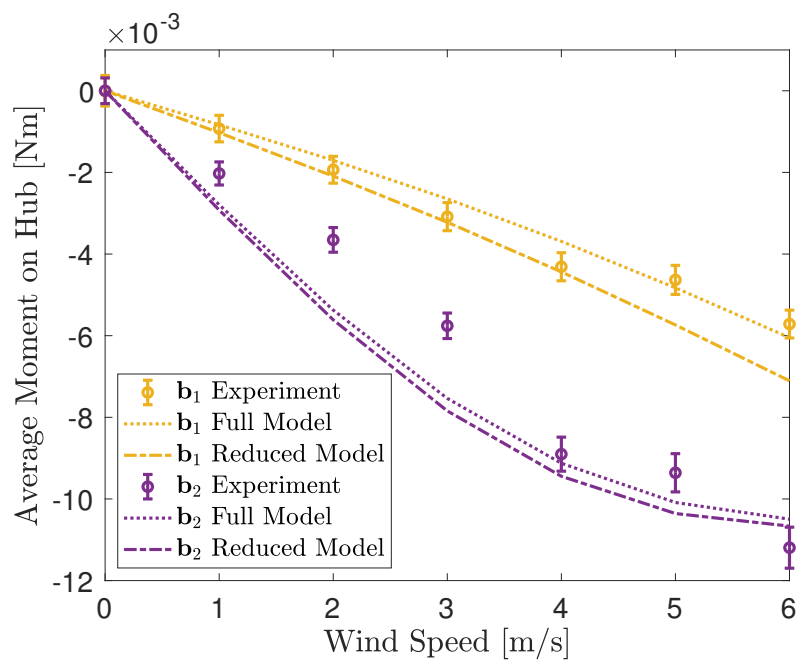


Figure 3.5: Hub moment in wind: model/data comparison

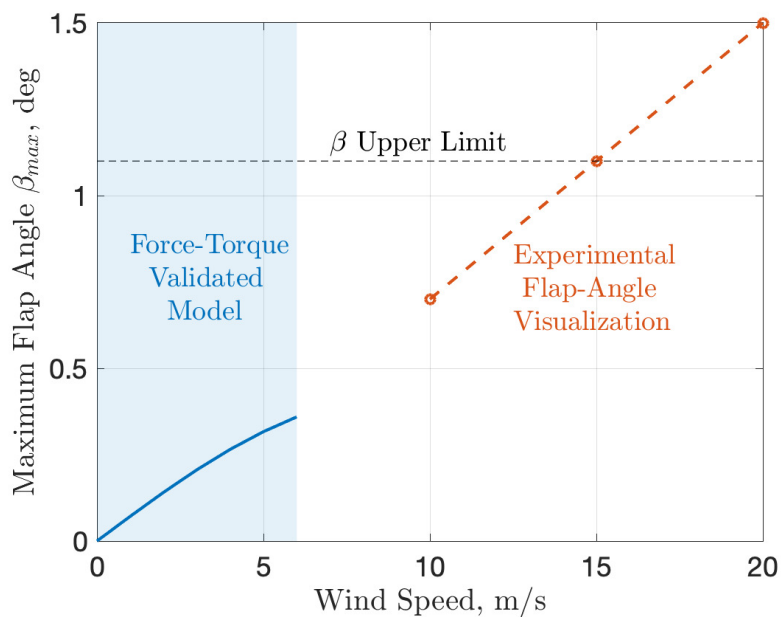


Figure 3.6: Maximum flap-angle dependency on wind at 12,000 rpm. Upper limit denotes the flap angle requiring a control moment that saturates the thrusts.

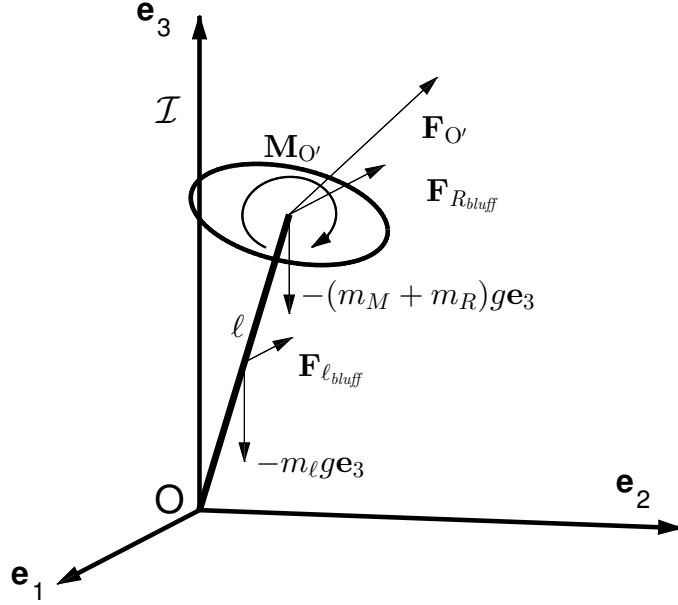


Figure 3.7: Rotor-pendulum free-body diagram

the force $-(m_m + m_{\bar{r}})g\mathbf{e}_3$ due to the weight of the motor and rotor at the hub, the force $-m_\ell g\mathbf{e}_3$ due to the weight of the rod, and the bluff-body forces.

The position of the point O' with respect to O is $\mathbf{r}_{O'/O} = \ell\mathbf{b}_3$ and the corresponding inertial velocity is ${}^{\mathcal{I}}\mathbf{v}_{O'/O} = \ell\dot{\phi}\mathbf{b}_1 + \ell\dot{\theta}S_\phi\mathbf{b}_2$. The angular velocity of frame \mathcal{B} with respect to \mathcal{I} is ${}^{\mathcal{I}}\boldsymbol{\omega}^{\mathcal{B}} = \dot{\theta}\mathbf{a}_3 + \dot{\phi}\mathbf{b}_2 = -\dot{\theta}S_\phi\mathbf{b}_1 + \dot{\phi}\mathbf{b}_2 + \dot{\theta}C_\phi\mathbf{b}_3$, and the angular velocity of the rotor is ${}^{\mathcal{I}}\boldsymbol{\omega}^{\mathcal{C}} = {}^{\mathcal{I}}\boldsymbol{\omega}^{\mathcal{B}} + \omega\mathbf{b}_3$. Let m_m and $m_{\bar{r}}$ be the mass of the motor and rotor, respectively, and I_ℓ and $I_{\bar{r}}$ the moment of inertia matrices for the rod and rotor, respectively. The total angular momentum of the system with respect to origin O is

$$\begin{aligned} {}^{\mathcal{I}}\mathbf{h}_O &= I_\ell {}^{\mathcal{I}}\boldsymbol{\omega}^{\mathcal{B}} + \mathbf{r}_{\ell/O} \times m_\ell {}^{\mathcal{I}}\mathbf{v}_{\ell/O} \\ &\quad + I_{\bar{r}} {}^{\mathcal{I}}\boldsymbol{\omega}^{\mathcal{C}} + \mathbf{r}_{O'/O} \times (m_m + m_{\bar{r}}) {}^{\mathcal{I}}\mathbf{v}_{O'/O} \end{aligned} \quad (3.19)$$

and the moment about O is

$$\begin{aligned} \mathbf{M}_O = & \mathbf{M}_{O'} + \frac{\ell}{2} \mathbf{b}_3 \times (-m_\ell g \mathbf{e}_3 + \mathbf{F}_{\ell_{bluff}}) \\ & + \ell \mathbf{b}_3 \times (-(m_m + m_{\bar{r}})g \mathbf{e}_3 + \mathbf{F}_{O'} + \mathbf{F}_{\bar{r}_{bluff}}). \end{aligned} \quad (3.20)$$

Assuming that the angular velocity of the rotor ω is sufficiently large such that the angular velocity ${}^{\mathcal{I}}\boldsymbol{\omega}^{\mathcal{B}}$ may be ignored in the calculation of ${}^{\mathcal{I}}\boldsymbol{\omega}^{\mathcal{C}}$, and defining $m_{O'} \triangleq m_m + m_{\bar{r}}$, the equations of motion for the system resulting from Euler's second law are

$$\begin{aligned} \ddot{\theta} = & \frac{1}{\left(\frac{m_\ell}{3} + m_{O'}\right) \ell^2 S_\phi} \left[-\mathbf{M}_O \cdot \mathbf{b}_1 + \frac{m_{\bar{r}}}{3} \bar{r}^2 \dot{\phi} \left(\dot{\theta} C_\phi + \omega \right) \right. \\ & \left. - 2 \left(m_{O'} + \frac{m_\ell}{3} \right) \ell^2 \dot{\phi} \dot{\theta} C_\phi \right] - \zeta_{RP} \dot{\theta}, \end{aligned} \quad (3.21)$$

$$\begin{aligned} \ddot{\phi} = & \frac{1}{\left(\frac{m_\ell}{3} + m_{O'}\right) \ell^2} \left[\mathbf{M}_O \cdot \mathbf{b}_2 + \left(m_{O'} + \frac{m_\ell}{3} \right) \ell^2 \dot{\theta}^2 S_\phi C_\phi \right. \\ & \left. + \left(m_{O'} + \frac{m_\ell}{2} \right) g \ell S_\phi - \frac{m_{\bar{r}}}{3} \bar{r}^2 \dot{\theta} S_\phi \left(\dot{\theta} C_\phi + \omega \right) \right] - \zeta_{RP} \dot{\phi}, \end{aligned} \quad (3.22)$$

which include rotor-pendulum damping term ζ_{RP} , representing the natural damping of the bearings, wires, and other components of the physical system. When aerodynamic forces and rotor-pendulum damping are ignored, (3.21) and (3.22) reduce to the gyro-pendulum equations [56, pp. 469-471]. In order to simulate the forces and moments in MATLAB, the wind vector is used to identify $\mu = \|\Delta \mathbf{v}_\infty\|/(\omega \bar{r})$, β , and the \mathcal{U} and \mathcal{V} frames, which are used with the above calculations to produce \mathbf{M}_O .

Equilibrium analysis is performed by setting $[\dot{\theta}, \ddot{\theta}, \dot{\phi}, \ddot{\phi}]^T = 0$ in (3.21) and (3.22), assuming small angles such that the magnitude of the wind velocity component in the plane of the rotor is constant, and using the parameters listed in Tab. 3.1. When $\mathbf{V}_\infty = 0$ m/s, the rotor-pendulum hangs at the downward equilibrium

Table 3.1: Rotor-Pendulum Model Parameters

Parameter	Name	Value	Units
C_{l_α}	airfoil lift slope	2π	[]
λ_0	avg. inflow ratio	0.075	[]
ζ	blade damping coef.	0.026	[]
I_β	blade inertia	1.8×10^{-6}	kgm^2
ν_β	blade scaled nat. freq.	1.9	[]
θ_{tw}	blade twist	-6.6	deg
c	chord length	0.015	m
ρ	density of air	1.225	kg/m^3
e	effective hinge offset	0.1	[]
k_β	hinge spring const.	3	Nm/rad
γ	Lock number	1.04	[]
m_m	motor mass	0.018	kg
N_b	number of blades	2	[]
ζ_{RP}	pendulum damp. coef.	1	[]
ℓ	rod length	0.254	m
m_ℓ	rod mass	0.043	kg
w	rod width	0.01	m
θ_0	root angle of attack	16	deg
$m_{\bar{r}}$	rotor mass	0.0027	kg
\bar{r}	rotor radius	0.0635	m
ω_{β_0}	spring nat. freq.	1290	rad/s

$[\theta_{eq}, \phi_{eq}] = [0^\circ, 180^\circ]$, whereas $\mathbf{V}_\infty = -3\mathbf{e}_1$ m/s yields an offset to the side and in the direction of the wind with $[\theta_{eq}, \phi_{eq}] = [19^\circ, 186^\circ]$. Using state vector $[\theta, \dot{\theta}, \phi, \dot{\phi}]^T$ and solving numerically for the Jacobian matrix, the linearized equations of motion using $\mathbf{V}_\infty = -3\mathbf{e}_1$ m/s and $\omega = 8000$ rpm are

$$\frac{d}{dt} \begin{bmatrix} \theta \\ \dot{\theta} \\ \phi \\ \dot{\phi} \end{bmatrix} = \begin{bmatrix} 0 & 1 & 0 & 0 \\ -45.5 & -1.38 & -4.68 & -15.1 \\ 0 & 0 & 0 & 1 \\ -0.0339 & 0.146 & -44.2 & -1.03 \end{bmatrix} \begin{bmatrix} \theta \\ \dot{\theta} \\ \phi \\ \dot{\phi} \end{bmatrix}. \quad (3.23)$$

The eigenvalues of this system are $(-0.534+5.97i, -0.534-5.97i, -0.668+7.45i, -0.668-7.45i)$, showing exponential stability with moderate oscillations. Although the matrix values differ when varying wind speed with constant ω , the eigenvalues remain in similar locations. Thus, using the above parameters, the rotor-pendulum without wind settles to the downward vertical, whereas the rotor-pendulum with wind converges to an off-vertical angle approximately 19° from the wind direction.

The rotor-pendulum is simulated using (3.21) and (3.22) in the presence of a step wind input with the rotor-pendulum initially hanging downward. Figure 3.8 shows the simulated trajectory of the end of the rotor-pendulum projected on the horizontal plane, from the perspective of looking down at the hanging pendulum. As expected, with no wind at all, the rotor-pendulum simply hangs downward. As the magnitude of the gust increases, the vertical offset angle and magnitude of oscillation increase, with the rotor-pendulum settling over time to the equilibrium value in the center of the oscillation. As the wind increases, the angle θ about the \mathbf{e}_3 axis reduces slightly due to the bluff body force, more closely aligning the pendulum

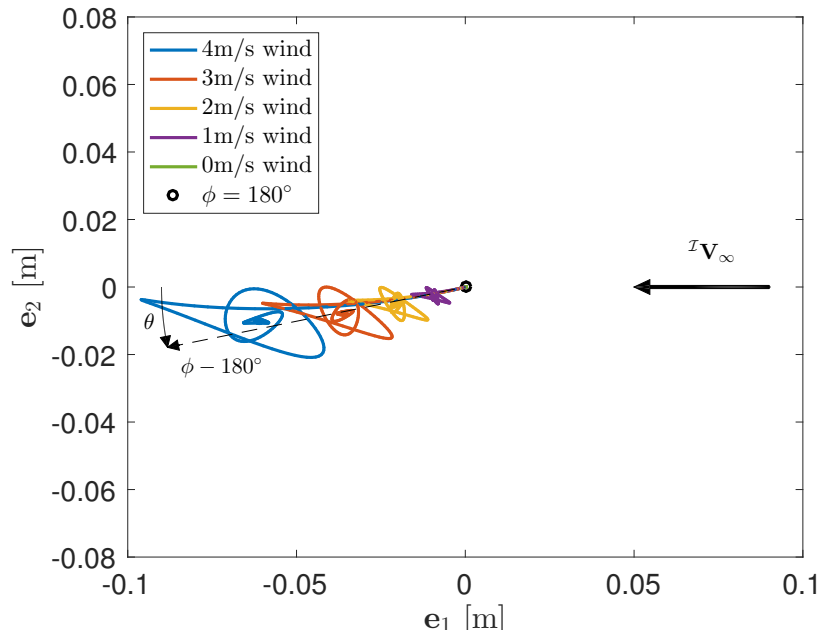


Figure 3.8: Simulated rotor-pendulum results

to the wind direction.

3.3 Rotor-Pendulum Experimental Results

In order to validate the rotor-pendulum model, an experimental stand (Fig. 3.9) was built and tested in a known wind field produced by a set of blower-style Dyson fans (Fig. 3.10), with the system response identified using 18 OptiTrack motion-capture cameras. Tests were initiated in the downward position and performed with a rotor speed of 8000 rpm and wind velocities of 0 m/s and $-3\mathbf{e}_1$ m/s. In order to verify the aerodynamic effects on the rotor, a disk with equal moment of inertia was constructed using a 3D printer and also tested at both wind speeds to help isolate the effect of the propeller's lifting surfaces. As expected, when testing without wind, both the rotor and disk exhibit stable equilibria at $\phi = 180^\circ$ and arbitrary

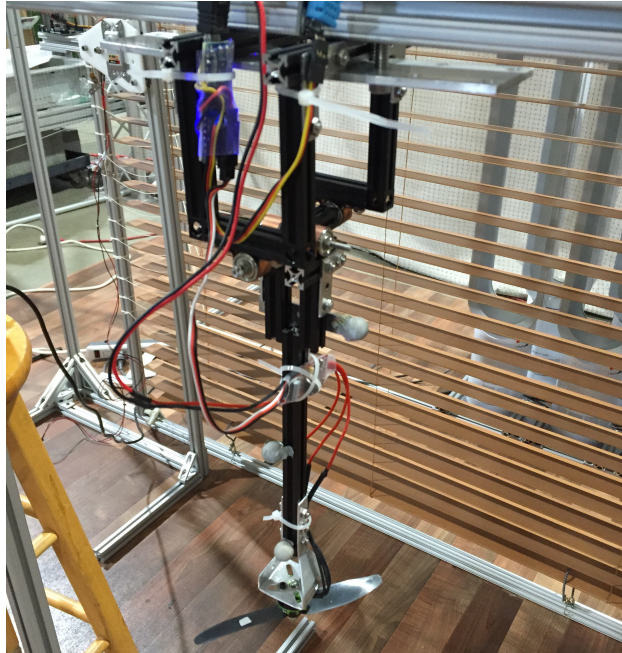


Figure 3.9: Rotor-pendulum stand



Figure 3.10: Test stand with gust generation system

side-offset θ . Under a constant $-3\mathbf{e}_1$ m/s wind, the stable equilibrium point for the experimental stand with the rotor is $[\theta_{eq}, \phi_{eq}] = [20^\circ, 190^\circ]$, and with the disk is $[\theta_{eq}, \phi_{eq}] = [6^\circ, 182^\circ]$. This result shows substantial influence of the propeller's lifting surfaces compared to the effect of bluff-body drag alone.

To test a dynamic response, a wind step input from 0 to $-3\mathbf{e}_1$ m/s was generated by opening the blinds between the fans and the test stand in Fig. 3.10 with the fans running throughout the test. Figure 3.11 shows the experimental results in comparison to the theoretical results under the same conditions.

Without the lifting surfaces of a rotor, bluff-body drag moves the disk only slightly, and in the direction approximately parallel to the wind direction as expected. The propeller also moves primarily in the direction of the wind, but to a much greater extent, and progresses in an inward spiral pattern as it reaches an equilibrium angle. This result shows the influence of the lifting surfaces of the propeller in wind: creating a higher moment, which also yields slight movement in the $-\mathbf{e}_2$ direction. Theoretical and experimental results show strong agreement, indicating the importance of linear inflow calculations in blade-flapping analysis. Slight inaccuracy between the model and experiment is likely due to unmodeled aerodynamic complexity.

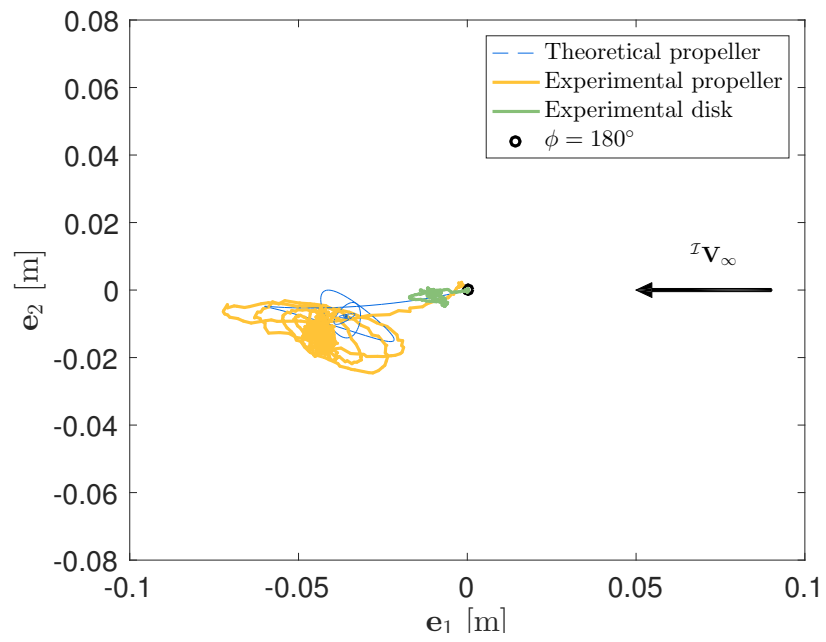


Figure 3.11: Model/data comparison for rotor-pendulum experiment

Chapter 4: Nonlinear Control of Quadrotor Attitude and Position

The models of aerodynamic forces and moments in Chapter 3 enable the development of a controller capable of addressing wind gusts directly. Inner- and outer-loop controllers are developed separately, with simulated results presented for each. A variable-gain algorithm is also presented to address thrust constraints. The position and attitude control architecture is shown in Fig. 4.1, with the separate inner- and outer-loop controllers that are detailed below the dotted line. This chapter contains work presented in the 2017 ASME Dynamic Systems and Control Conference [46], as well as the 2019 AIAA SciTech Forum [48].

4.1 Attitude Control Design with $SO(3)$

By representing the kinematics using rotation matrices in the Lie group $SO(3)$, I extend the controller in [32] with flow feedback to produce a flow-aware attitude controller that achieves nearly global stabilization while avoiding singularities associated with Euler angles. The configuration error function [57]

$$\Psi(R, R_d) = \frac{1}{2} \text{tr} (I - R_d^T R), \quad (4.1)$$

is locally positive definite when the angle between R and R_d , defined by $\theta_R = \arccos((\text{Tr}(R_d^T R) - 1)/2)$, is less than π [32]. The angle is less than π when

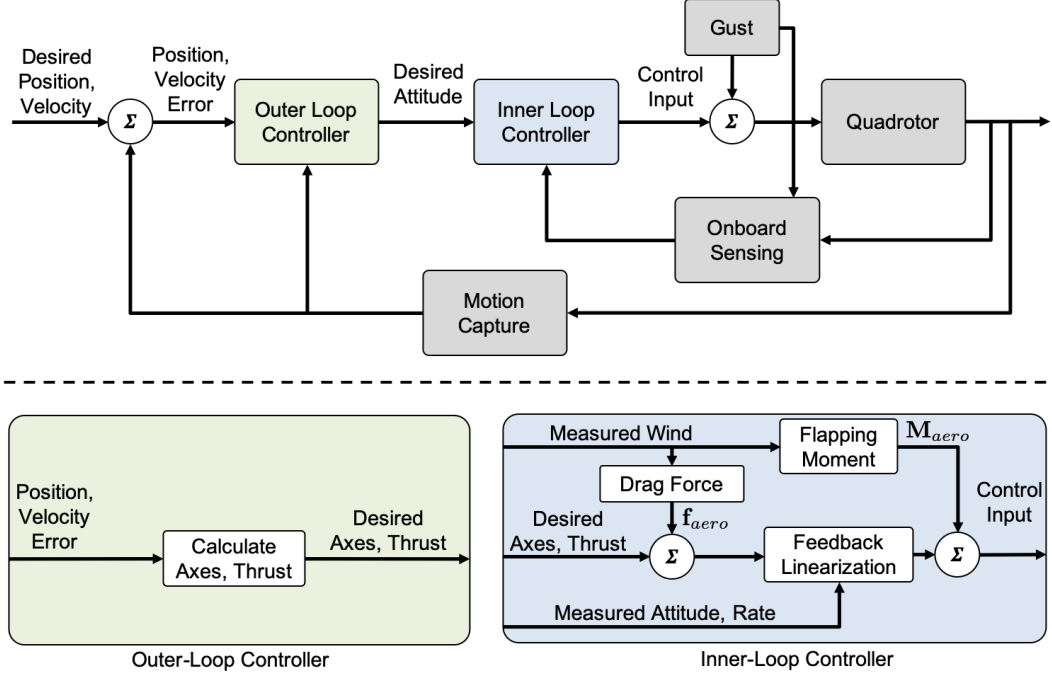


Figure 4.1: Position and control architecture

$\Psi(R, R_d) < 2$, which occurs almost globally. The attitude tracking error \mathbf{e}_R is [32]

$$\mathbf{e}_R = \frac{1}{2} (R_d^T R - R^T R_d)^\vee, \quad (4.2)$$

which is derived from the configuration error function. The angular-velocity tracking error is [32]

$$\mathbf{e}_\Omega = \Omega - R^T R_d \Omega_d. \quad (4.3)$$

Note $d(R_d^T R)/dt = (R_d^T R)\hat{\mathbf{e}}_\Omega$, when compared to (2.1), shows \mathbf{e}_Ω is to $R_d^T R$ as Ω is to R .

I employ the development of the aerodynamic moment on the propeller hub from Section 3.2 and Appendix A to the complete quadrotor, and describe $\mathbf{M}_{O'}^\perp$ in the \mathcal{U} frame:

$$\mathbf{M}_{O'}^\perp \approx \frac{N_b}{2\pi} \int_0^{2\pi} k_\beta \beta_{\max} S_{(\psi-\phi_D)}^2 (C_{\phi_D} \mathbf{u}_1 + S_{\phi_D} \mathbf{u}_2) d\psi, \quad (4.4)$$

which integrates to

$$\mathbf{M}_{O'}^\perp \approx \frac{N_b}{2} k_\beta \beta_{\max} (C_{\phi_D} \mathbf{u}_1 + S_{\phi_D} \mathbf{u}_2). \quad (4.5)$$

When solving for the total aerodynamic moment on the quadrotor, counter-rotating pairs cancel the \mathbf{u}_1 component to yield

$$\mathbf{M}_{aero} = [4k_\beta \beta_{\max} S_{\phi_D} \mathbf{u}_2 \cdot \mathbf{b}_1, 4k_\beta \beta_{\max} S_{\phi_D} \mathbf{u}_2 \cdot \mathbf{b}_2, 0]^T. \quad (4.6)$$

The thrust moment is determined based on the position and rotation for each motor. Using the "X" configuration for the quadrotor in this work, the thrust moment is

$$\mathbf{M}_{thrust} = \begin{bmatrix} \frac{\ell\sqrt{2}}{4}(-T_1 - T_2 + T_3 + T_4) \\ \frac{\ell\sqrt{2}}{4}(T_1 - T_2 + T_3 - T_4) \\ c_m(T_1 - T_2 - T_3 + T_4) \end{bmatrix}, \quad (4.7)$$

where c_m is a coefficient relating the thrust produced to the torque of the motor, found empirically to be approximately 0.0085 Nm/N for the testbed described in Section 2.3.

The system is stabilized using the thrust moment in (4.7) to address attitude and rate errors. The 3-DOF quadrotor attitude stand is overactuated, allowing specification of any desired configuration of three angles. In fact, in order to avoid redundant controls, three inputs are defined corresponding to the three degrees of freedom in the system:

$$\begin{aligned} \nu_1 &= -T_1 - T_2 + T_3 + T_4 \\ \nu_2 &= T_1 - T_2 + T_3 - T_4 \\ \nu_3 &= T_1 - T_2 - T_3 + T_4. \end{aligned} \quad (4.8)$$

Taking T_0 to be the nominal thrust in hover yields

$$\begin{aligned}
T_1 &= T_0 + \frac{1}{4}(-\nu_1 + \nu_2 + \nu_3) \\
T_2 &= T_0 + \frac{1}{4}(-\nu_1 - \nu_2 - \nu_3) \\
T_3 &= T_0 + \frac{1}{4}(\nu_1 + \nu_2 - \nu_3) \\
T_4 &= T_0 + \frac{1}{4}(\nu_1 - \nu_2 + \nu_3),
\end{aligned} \tag{4.9}$$

which implies

$$\mathbf{M}_{thrust} = \left[\frac{\ell\sqrt{2}}{4}\nu_1, \frac{\ell\sqrt{2}}{4}\nu_2, c_m\nu_3 \right]^T. \tag{4.10}$$

The equations of motion for the 3DOF quadrotor test-stand using the error dynamics are [46]

$$\dot{\mathbf{e}}_R = \frac{1}{2} (\text{tr} [R^T R_d] I - R^T R_d) \mathbf{e}_\Omega \tag{4.11}$$

and

$$\dot{\mathbf{e}}_\Omega = J^{-1} \left(-\hat{\Omega} J \Omega + \mathbf{M}_{thrust} + \mathbf{M}_{aero} \right) + \hat{\Omega} R^T R_d \Omega_d - R^T R_d \dot{\Omega}_d. \tag{4.12}$$

Define $H = \text{diag}\{\ell\sqrt{2}/4, \ell\sqrt{2}/4, c_m\}$ and $\boldsymbol{\nu} = [\nu_1, \nu_2, \nu_3]^T$, then choose [46]

$$\begin{aligned}
\boldsymbol{\nu} = H^{-1} J \left[-k_R \mathbf{e}_R - k_\Omega \mathbf{e}_\Omega - J^{-1} \left(-\hat{\Omega} J \Omega + \mathbf{M}_{aero} \right) \right. \\
\left. - \hat{\Omega} R^T R_d \Omega_d + R^T R_d \dot{\Omega}_d \right]
\end{aligned} \tag{4.13}$$

such that

$$\begin{aligned}
\mathbf{M}_{thrust} = -Jk_R \mathbf{e}_R - Jk_\Omega \mathbf{e}_\Omega + \hat{\Omega} J \Omega - \mathbf{M}_{aero} \\
+ J \left(-\hat{\Omega} R^T R_d \Omega_d + R^T R_d \dot{\Omega}_d \right).
\end{aligned} \tag{4.14}$$

When (4.14) is inserted in (4.12), the angular-velocity error dynamics become [46]

$$\dot{\mathbf{e}}_\Omega = -k_R \mathbf{e}_R - k_\Omega \mathbf{e}_\Omega. \tag{4.15}$$

The following result is proven for a system with time varying parameters and thus extends to this system with time varying wind velocity ${}^B\mathbf{V}_O = {}^B\mathbf{V}_O(t)$.

Proposition 4.1 ([32] Exponential Stability of Attitude Dynamics) *Consider the control moment \mathbf{M}_{thrust} defined in (4.14) for any positive constants k_R, k_Ω . Suppose that the initial condition satisfies*

$$\begin{aligned} \Psi(R(0), R_d(0)) &< 2 \\ \|\mathbf{e}_\Omega(0)\|^2 &< \frac{2}{\lambda_{\min}(J)} k_R (2 - \lambda_{\min}(J) \Psi(R(0), R_d(0))), \end{aligned} \tag{4.16}$$

where $\lambda_{\min}(J)$ is the minimum eigenvalue of the inertia matrix J . Then, the zero equilibrium of the attitude tracking error $\mathbf{e}_R, \mathbf{e}_\Omega$ is exponentially stable. Furthermore, there exist constants $\alpha_2, \beta_2 > 0$ such that

$$\Psi(R(t), R_d(t)) \leq \min\{2, \alpha_2 e^{-\beta_2 t}\}. \tag{4.17}$$

The conditions in Proposition 4.1 are satisfied almost globally, as long as $R(0)$ and $R_d(0)$ differ by less than π . Additionally, from (4.16), the initial bound on the attitude rate error can be increased by increasing k_R .

Considering the inherent limitations of the motors and propellers, the thrust of each propeller is saturated above by some maximum thrust T_{\max} and below by zero, i.e., $0 \leq T_j \leq T_{\max}, j = 1, \dots, 4$.

Lemma 4.2 *Let $T' = \min(T_{\max} - T_0, T_0) > 0$. We have $T_j \leq T_{\max}$, for all $j = 1, \dots, 4$, provided that*

$$|\nu_1| + |\nu_2| + |\nu_3| \leq 4T'. \tag{4.18}$$

Proof. (The proof is shown for T_1 , but may be adapted for the other propellers.)

From (4.18), we have

$$-4T' \leq -\nu_1 + \nu_2 + \nu_3 \leq 4T', \quad (4.19)$$

which implies

$$-T_0 \leq \frac{1}{4}(-\nu_1 + \nu_2 + \nu_3) \leq T_{\max} - T_0. \quad (4.20)$$

Rearranging (4.20) yields

$$0 \leq T_0 + \frac{1}{4}(-\nu_1 + \nu_2 + \nu_3) \leq T_{\max} \quad (4.21)$$

and, substituting terms from (4.9), yields

$$0 \leq T_1 \leq T_{\max}. \quad (4.22)$$

□

Pappas et al. [40] show that, given a feedback-linearizable system with bounded input $\dot{x} = f(x) + g(x)u$, $|u| \leq M$, stabilizing control can be achieved if the portion of the input dedicated to feedback linearization is less than the upper bound, i.e., $|g^{-1}(x)f(x)| < M$. In order to apply the results from [40] to our system, define $\boldsymbol{\delta} = [\delta_1, \delta_2, \delta_3]^T \triangleq H^{-1}J[-J^{-1}(-\hat{\boldsymbol{\Omega}}J\boldsymbol{\Omega} + \mathbf{M}_{aero}) - \hat{\boldsymbol{\Omega}}R^TR_d\boldsymbol{\Omega}_d + R^TR_d\dot{\boldsymbol{\Omega}}_d]$ and $\mathbf{u} = [u_1, u_2, u_3]^T \triangleq H^{-1}J[-k_R\mathbf{e}_R - k_\Omega\mathbf{e}_\Omega]$, such that $\boldsymbol{\nu} = \boldsymbol{\delta} + \mathbf{u}$. I use $\boldsymbol{\delta}$ to represent the cost of feedback linearization of the error dynamics, and \mathbf{u} to represent the stabilizing control. In the following proposition, $\epsilon > 0$ represents the control authority available for stabilization.

Proposition 4.3 *If the cost of feedback linearization $\boldsymbol{\delta}$ satisfies*

$$|\delta_1| + |\delta_2| + |\delta_3| \leq 4T' - \epsilon, \quad (4.23)$$

then the error dynamics of the input-constrained system Eqns. (4.11) and (4.15) are exponentially stable by proposition 4.1.

Proof. Insert $\boldsymbol{\nu} = \boldsymbol{\delta} + \mathbf{u}$ into (4.18) to obtain

$$|\delta_1 + u_1| + |\delta_2 + u_2| + |\delta_3 + u_3| \leq 4T', \quad (4.24)$$

which is satisfied if

$$|\delta_1| + |\delta_2| + |\delta_3| + |u_1| + |u_2| + |u_3| \leq 4T'. \quad (4.25)$$

Rewriting (4.23), we find

$$|\delta_1| + |\delta_2| + |\delta_3| + \epsilon \leq 4T'. \quad (4.26)$$

Comparing (4.26) to (4.25), if we choose k_R and k_Ω such that

$$|u_1| + |u_2| + |u_3| \leq \epsilon, \quad (4.27)$$

then the inputs will satisfy (4.18) and, by lemma 4.2, the thrusts will not saturate. If (4.16) is also satisfied, then with positive gains k_R and k_Ω chosen to satisfy (4.27), proposition 4.1 is satisfied, and the zero equilibrium of the tracking error is exponentially stable [32]. \square

4.2 Three Degree-of-Freedom Attitude Simulation

I now investigate conditions under which Proposition 4.3 is satisfied so that the system may be stabilized. Consider a station-keeping scenario, such that $\boldsymbol{\Omega}_d \equiv 0$,

which leads to $\boldsymbol{\delta} \triangleq H^{-1}(\hat{\boldsymbol{\Omega}}J\boldsymbol{\Omega} - \mathbf{M}_{aero})$. When represented in matrix components,

$$\boldsymbol{\delta} = \begin{bmatrix} \frac{2}{\ell}[(J_2 - J_3)qr - 4k_\beta\beta_{\max}S_{\phi_D}\mathbf{u}_2 \cdot \mathbf{b}_1] \\ \frac{2}{\ell}[(J_3 - J_1)pr - 4k_\beta\beta_{\max}S_{\phi_D}\mathbf{u}_2 \cdot \mathbf{b}_2] \\ \frac{1}{c_m}(J_1 - J_2)pq \end{bmatrix}. \quad (4.28)$$

From the symmetry of the quadrotor, note $J_1 = J_2$ and $J_3 = 2J_1$, such that

$$\boldsymbol{\delta} = \begin{bmatrix} \frac{2}{\ell}[-2J_1qr - 4k_\beta\beta_{\max}S_{\phi_D}\mathbf{u}_2 \cdot \mathbf{b}_1] \\ \frac{2}{\ell}[2J_1pr - 4k_\beta\beta_{\max}S_{\phi_D}\mathbf{u}_2 \cdot \mathbf{b}_2] \\ 0 \end{bmatrix}. \quad (4.29)$$

When applied to (4.23), we have

$$\left| \frac{1}{\ell}[-2J_1pr - 4k_\beta\beta_{\max}S_{\phi_D}\mathbf{u}_2 \cdot \mathbf{b}_2] \right| \leq \left| \frac{2J_1}{\ell}pr \right| + \left| \frac{4}{\ell}k_\beta\beta_{\max} \right| \leq T' - \frac{\epsilon}{4}, \quad (4.30)$$

$$\left| \frac{1}{\ell}[2J_1qr - 4k_\beta\beta_{\max}S_{\phi_D}\mathbf{u}_2 \cdot \mathbf{b}_1] \right| \leq \left| \frac{2J_1}{\ell}qr \right| + \left| \frac{4}{\ell}k_\beta\beta_{\max} \right| \leq T' - \frac{\epsilon}{4}.$$

Thus, when the system experiences zero angular velocity, the flapping angle must satisfy $\beta_{\max} < \ell T' / (4k_\beta) \approx 1.1^\circ$ using the system parameters listed in Table 4.1 corresponding to the experimental testbed. A combination of theoretical and experimental results are used to identify the wind velocity corresponding to this flap angle. Theoretical results have been validated up to 6 m/s using an ATI Nano 17 six-axis Force-Torque transducer [45]. Experimental values for high-speed flow were gathered using high-speed cameras and image processing techniques [58]. Figure 3.6 shows the values for each, indicating that the quadrotor will reach the bound on β_{\max} in a 15 m/s wind gust.

From the condition on angular velocity in (4.30), when the system experiences zero wind, angular velocities must satisfy $pr < \ell T' / (2J_1)$ and $qr < \ell T' / (2J_1)$, which

correspond to $pr < 50 \text{ rad/s}^2$ and $qr < 50 \text{ rad/s}^2$ for our parameters. Attitude bounds are satisfied when p , q , and r are each less than 7 rad/s or, alternatively, when p and q are less than 50 rad/s and r , which is not critical for station holding, is less than 1 rad/s .

In order to show the effectiveness of the controller, it is tested with and without saturation under the same conditions. (Note that the system model used here for testing is the full aerodynamic model from [45] rather than the simplified model used to design the controller.) Using the parameters in Tab. 4.1, a repeated edgewise 20 m/s 1-cosine gust is applied, shown in Fig. 4.2. The quadrotor's initial attitude is $R(0) = I$ and rates are $\Omega(0) = [0, 0, 0]^T$, with $R_d = I$ and $\Omega_d = [0, 0, 0]^T$. The response is shown in Fig. 4.3, with the corresponding control effort in Fig. 4.4. The quadrotor response to nonzero attitude rates is also shown in Fig. 4.5 with no wind, $R(0) = I$, with $R_d = I$ and $\Omega_d = [0, 0, 0]^T$, using initial rates of $\Omega(0) = [5, 5, 5]^T$, with the corresponding control effort in Fig. 4.6. Attitude response figures use a logarithmic vertical axis to more effectively show differences in the configuration error function.

Attitude and control plots show the system with and without saturation, and with and without flow sensing. Figure 4.3 shows lower error in the system with flow sensing, and no difference between saturated and unsaturated thrusts. The controller is able to effectively reject the gust without saturating the thrusts, so the saturated and unsaturated systems show identical results. Figure 4.3 shows that the system in the presence of repeated gusts exhibits predictable deviations and returns to the equilibrium value with no destabilizing effect due to repetition.

Table 4.1: Quadrotor Model Parameters

Parameter	Name	Value	Units
A_f	quadrotor frontal area	0.02	m^2
C_D	quadrotor drag coef.	0.8	[]
C_{l_α}	airfoil lift slope	2π	[]
λ_0	avg. inflow ratio	0.075	[]
ℓ	beam length	0.21	m
m_ℓ	beam mass	0.03	kg
ζ	blade damping coef.	0.026	[]
I_β	blade inertia	1.8×10^{-6}	kgm^2
ν_β	blade scaled nat. freq.	1.5	[]
θ_{tw}	blade twist	-6.6	deg
c	chord length	0.015	m
ρ	density of air	1.225	kg/m^3
e	effective hinge offset	0.1	[]
k_β	hinge spring const.	3	Nm/rad
γ	Lock number	1.04	[]
m	quadrotor mass	0.510	kg
m_m	motor mass	0.018	kg
c_m	motor torque coefficient	0.0085	[]
N_b	number of blades	2	[]
T_{\max}	propeller max thrust	3	N
T_0	propeller nom. thrust	1.3	N
ω	propeller nom. ang. vel.	12,000	rpm
θ_0	root angle of attack	16	deg
m_r	rotor mass	0.0027	kg
r	rotor radius	0.0635	m
ω_{β_0}	spring nat. freq.	1290	rad/s

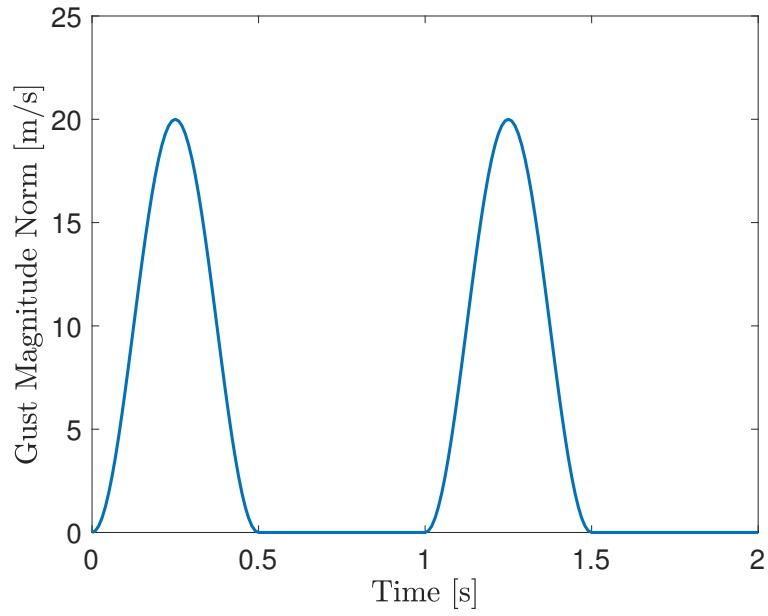


Figure 4.2: 20 m/s 1-cosine wind gust profile

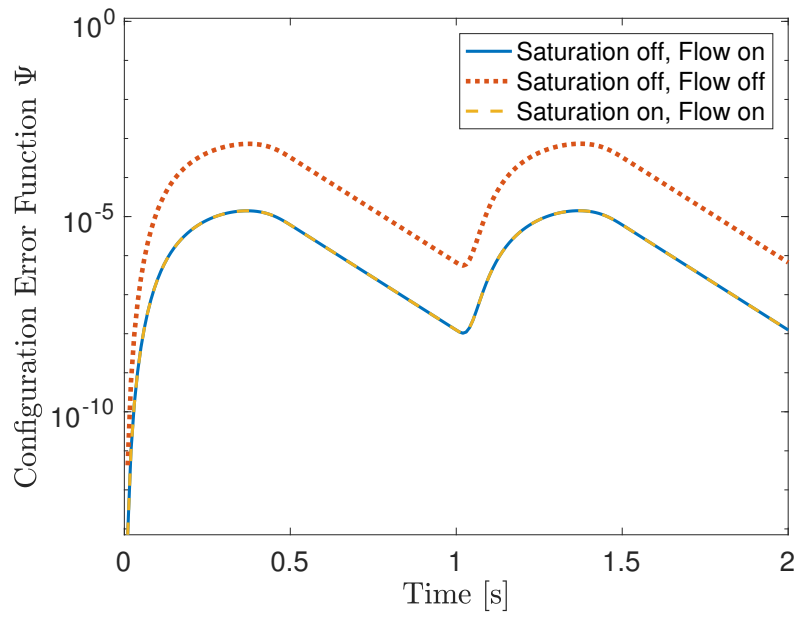


Figure 4.3: 20 m/s wind gust response, $\Omega(0) = [0, 0, 0]^T$

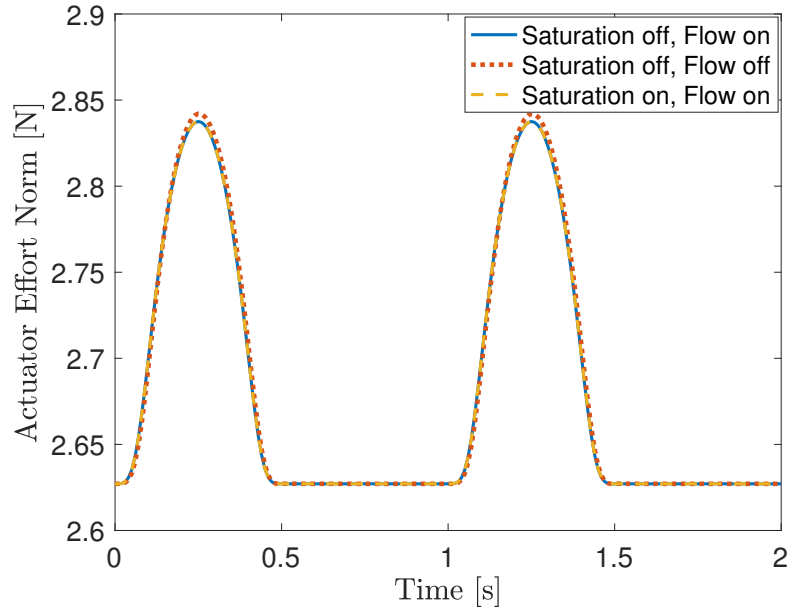


Figure 4.4: 20 m/s wind control effort, $\Omega(0) = [0, 0, 0]^T$

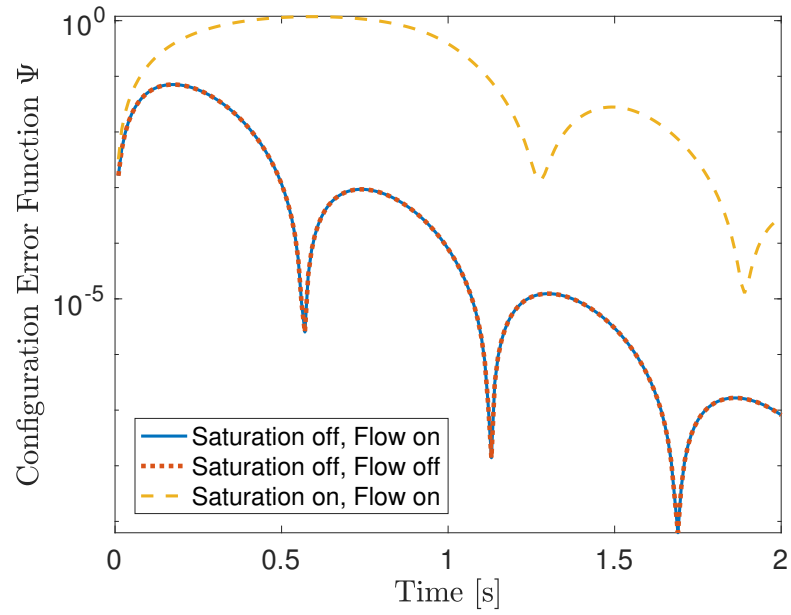


Figure 4.5: Response to $\Omega(0) = [5, 5, 5]^T$, no wind

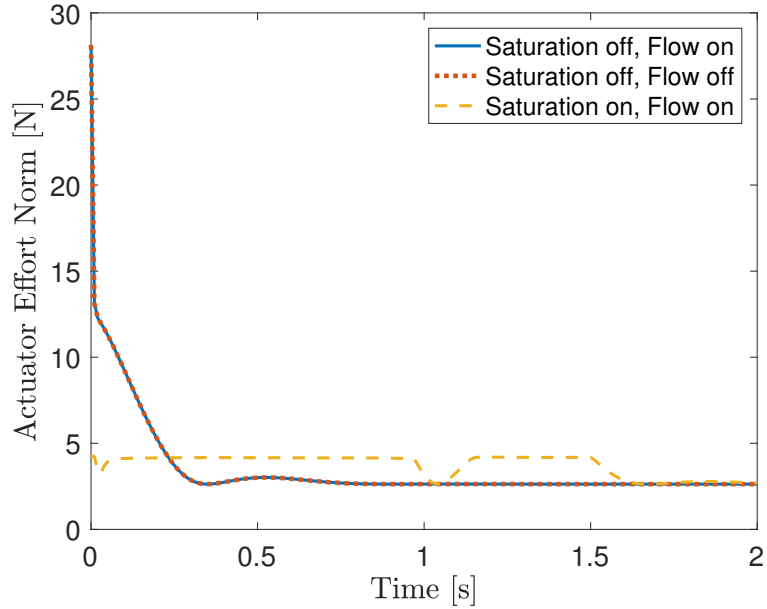


Figure 4.6: Control effort for $\Omega(0) = [5, 5, 5]^T$, no wind

The value of the configuration error function is very low with and without flow sensing, and when converted using the angle from the Euler axis, corresponds to approximately 0.3 degree error in the case with flow sensing versus 2 degree error in the case without flow sensing. Figure 4.4 shows very similar control efforts between different conditions, changing only based on flow sensing. Without flow sensing the actuators respond marginally later and with slightly higher magnitude; a small change in actuation that causes nearly an order of magnitude difference in peak angular error. While the steady state error can be mitigated with an integrator in the controller, both systems will experience a similar initial error, thus the controller with flow sensing will continue to show improved performance.

In Fig. 4.5, nonzero initial rates cause initial deviation, then gradual return to equilibrium. In the cases without thrust saturation, the result is identical due

to the absence of external flow over the vehicle, and the system quickly settles to a very low error. The rapid settling is due to an initial actuator response over five times greater than what is physically realizable, shown in Fig. 4.6. In the case with saturation, although the cost to feedback linearize the system does not saturate the inputs, the controller is unable to achieve the same control authority as the unsaturated cases. Input saturation effectively reduces the gains and results in larger initial deviations and a longer settling time, but nonetheless returns the system to equilibrium, showing that we can expect successful stabilization for the physical system under actuator limitations.

4.3 Variable-Gain Algorithm

The bound on the stabilization effort in (4.27) to keep the motors from saturating due to the stability gains may be addressed in practice through a variety of methods. One method is to use static gains and simply allow the system to saturate when the linearization effort or gains are too high. Although this is easy to implement and may be successful in many circumstances, the portion designed to linearize the system will not be preserved as motors saturate, and the intended direction of the moment on the vehicle may be altered.

Another approach may be applied by estimating the maximum disturbance on the system to solve for the available control authority ϵ , estimating the maximum errors \mathbf{e}_R and \mathbf{e}_Ω on the system, then choosing gains k_R and k_Ω such that the inputs do not exceed the estimated maximum control authority ϵ . This approach will be

successful up to a predetermined limit, and preserve the direction of the desired moment on the vehicle, but will generally result in conservative gains and possibly a slow system response.

A third approach uses the mathematical development above to monitor the linearization effort resulting from kinematics and aerodynamics and adjust the stabilizing gains in real time such that the motors do not saturate, which will also preserve the direction of the moment on the system. Using variable gains avoids putting additional bounds on the linearization effort and system errors, and can also provide higher gains when sufficient control authority exists (compared to choosing overly-conservative gains to avoid saturation). Gains are varied using multiplier k_{mod} such that the total control input $\boldsymbol{\nu} = \boldsymbol{\delta} + k_{mod}\mathbf{u}$, where $\boldsymbol{\delta}$ represents the cost of feedback linearization of the error dynamics, \mathbf{u} represents the stabilizing control, and k_{mod} is a multiplier such that $k_{mod}\mathbf{u}$ will use all available stabilizing control authority without exceeding thrust constraints. The algorithm requires two steps. The first step is to solve for the value of k_{mod} for each of the four motor inputs that will use all available control authority for that input, i.e., $k_{mod_i} = \max\left(\frac{-4T_0 - T_{i_\delta}}{T_{i_u}}, \frac{4T_{\max} - 4T_0 - T_{i_\delta}}{T_{i_u}}\right)$, where $T_{1_\delta} \triangleq -\delta_1 + \delta_2 + \delta_3$, $T_{1_u} \triangleq -u_1 + u_2 + u_3$, and $T_{1_\nu} \triangleq -\nu_1 + \nu_2 + \nu_3$ from Eqn. (4.9), and likewise for each of the other thrusts. Second, the smallest of the four values of k_{mod_i} is chosen such that only one input reaches the constraint, and the others remain within limits, i.e., $k_{mod} = \min(k_{mod_i})$. Additionally k_{mod} is restricted to $0 \leq k_{mod} \leq 1$ such that the nominal gains are used when sufficient control authority exists. Note that I have not adapted the stability analysis in [32] to account for dynamic gains, thus the stability guarantees only hold when sufficient authority exists

to use the nominal gains.

Corollary 4.4 *If (4.23) is satisfied and $\boldsymbol{\nu} = \boldsymbol{\delta} + k_{mod}\mathbf{u}$, with $k_{mod} = \min(k_{mod_i})$ and $k_{mod_i} = \max\left(\frac{-4T_0 - T_{i_\delta}}{T_{i_u}}, \frac{4T_{max} - 4T_0 - T_{i_\delta}}{T_{i_u}}\right)$, then (4.27) is satisfied and Prop. 2 holds for arbitrary positive k_R and k_Ω .*

Proof. If equation (4.23) is satisfied, then from [40], positive stabilizing gains k_R and k_Ω exist. The condition $k_{mod_i} = \max\left(\frac{-4T_0 - T_{i_\delta}}{T_{i_u}}, \frac{4T_{max} - 4T_0 - T_{i_\delta}}{T_{i_u}}\right)$ implies

$$\frac{-4T_0 - T_{1_\delta}}{(T_{1_u})} \leq k_{mod_i} \leq \frac{4(T_{max} - T_0) - T_{1_\delta}}{(T_{1_u})} \quad (4.31)$$

with gain scaling factor k_{mod_i} constrained to be positive to maintain the sign of the gains. This expression can be further rearranged as

$$-4T_0 - T_{1_\delta} \leq k_{mod_i}(T_{1_u}) \leq 4(T_{max} - T_0) - T_{1_\delta}, \quad (4.32)$$

and

$$-4T_0 \leq T_{i_\delta} + k_{mod_i}(T_{i_u}) \leq 4(T_{max} - T_0). \quad (4.33)$$

By the definition of T_{i_δ} , T_{i_u} , and T_{i_ν} , with $\boldsymbol{\nu} = \boldsymbol{\delta} + k_{mod}\mathbf{u}$, it follows that

$$-T_0 \leq \frac{1}{4}T_{i_\nu} \leq T_{max} - T_0, \quad (4.34)$$

which can be rewritten as

$$0 \leq T_i = T_0 + \frac{1}{4}T_{i_\nu} = T_i \leq T_{max}. \quad (4.35)$$

Thus, (4.9) is satisfied for arbitrary choice of k_R and k_Ω for each individual motor.

Choosing $k_{mod} = \min(k_{mod_i})$ ensures that the most conservative scaling factor is applied to all motors such that none exceed the thrust bound. \square

Investigating thrust saturation in simulation allows us to test conditions that we cannot produce on the test stand. Parameters for the quadrotor are shown in Tab. 4.1. We simulate the attitude-only case with initial conditions $\boldsymbol{\Omega} = [8, 8, 8]^T$ rad/s, where the effort to linearize exceeds the bounds, as well as $\boldsymbol{\Omega} = [4, 4, 4]^T$ rad/s, where the system does not saturate due to linearization effort, but the stability gains are sufficiently high to saturate the system. For each initial condition, we simulate the quadrotor without bounding the thrust, and with bounded thrust with and without variable gains. Figure 4.7 shows each initial condition, where different colors represent different bounding cases, and different line styles correspond to the two different initial conditions. The quadrotor angle in the first plot is the axis-angle representation of the rotation matrix R . The motor thrust for the unbounded case is shown on its own in the middle plot so that the differences in the low-thrust static gain and variable gain cases are highlighted in the third plot.

When the thrust is not bounded, the system reaches equilibrium much faster and with a significantly smaller deviation, though the thrust from one motor reaches over 40 N, compared to the actual limit of 3 N for each individual motor. More interestingly, all cases with bounded thrust stabilize, even when the linearization effort exceeds the thrust bounds and allows no initial stabilizing control. In the moderate case, $\boldsymbol{\Omega} = [4, 4, 4]^T$ rad/s, we see very similar performance for attitude stabilization; for the more aggressive case, $\boldsymbol{\Omega} = [8, 8, 8]^T$ rad/s, static gains show slightly better performance. This outcome is likely due to the lower norm for the variable gain case that occurs because the nominal motor thrust, 1.3 N, is not in the middle of the thrust range, 0–3 N. Thus, the lower bound can saturate more easily

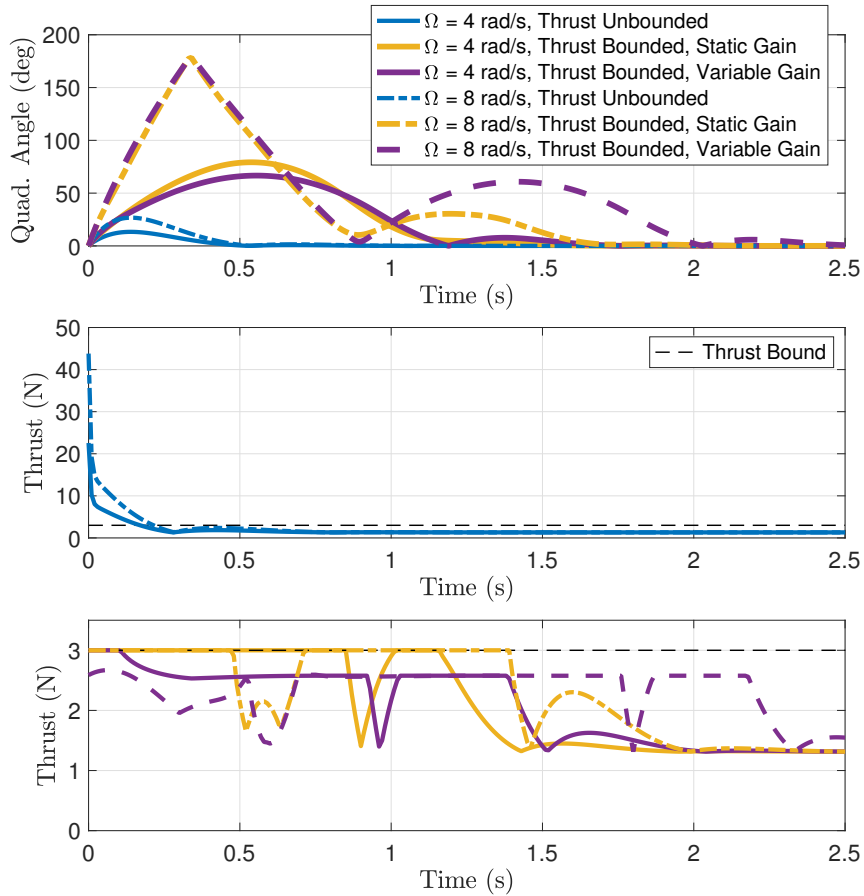


Figure 4.7: Effect of thrust saturation with multiple initial conditions, top: quadrotor angle, middle: maximum motor thrust for the unbounded case, bottom: maximum motor thrust for bounded cases

and, in order to maintain the desired direction of the moment on the vehicle, an artificially lower limit is placed on the upper bound. While static gains show better performance here, the input is restricted to be a moment, so the higher available authority leads to improved performance. However, in the free-flight case shown in the sequel, the addition of the total thrust as an input complicates control allocation such that the variable-gain approach becomes more effective.

4.4 Position Control Design with SE(3)

The outer loop of the cascaded controller design extends [32] with the addition of the aerodynamic drag force. It operates by solving for the position errors, then prescribing the magnitude and direction of the thrust through \mathbf{b}_3 and \mathbf{f}_{thrust} . The desired \mathbf{b}_1 direction is prescribed independently of \mathbf{f}_{thrust} and \mathbf{b}_3 . The thrust force and axis directions are transmitted to the inner loop, where desired roll and pitch angles are determined based on \mathbf{b}_{3_d} , with the desired yaw angle determined by \mathbf{b}_{1_d} . For position control, it is no longer assumed that the average thrust T_0 is constant, which may be incorporated in the above stability analysis without additional modification.

The desired attitude R_d input to the inner-loop controller is chosen based on the position and heading error of the quadrotor. Tracking errors are defined as [32]

$$\mathbf{e}_x = \mathbf{x} - \mathbf{x}_d, \quad (4.36)$$

$$\mathbf{e}_v = \mathbf{v} - \mathbf{v}_d,$$

where \mathbf{x}_d and \mathbf{v}_d are the desired position and velocity, respectively. For a given smooth tracking command $\mathbf{x}_d(t)$, and positive constants k_x and k_v , define [32]

$$\mathbf{b}_{3_d} = \frac{-k_x \mathbf{e}_x - k_v \mathbf{e}_v + m g \mathbf{e}_3 + m \ddot{\mathbf{x}}_d - \mathbf{f}_{aero}}{\| -k_x \mathbf{e}_x - k_v \mathbf{e}_v + m g \mathbf{e}_3 + m \ddot{\mathbf{x}}_d - \mathbf{f}_{aero} \|}, \quad (4.37)$$

where it is assumed $\| -k_x \mathbf{e}_x - k_v \mathbf{e}_v + m g \mathbf{e}_3 + m \ddot{\mathbf{x}}_d - \mathbf{f}_{aero} \| \neq 0$, and the aerodynamic drag term \mathbf{f}_{aero} is included as follows.

The drag force results from bluff body drag on the quadrotor as well as induced drag from the propellers such that $\mathbf{f}_{aero} = \mathbf{f}_{bluff} + \mathbf{f}_{ind}$. Define A_f as the frontal area

of the quadrotor and C_D as the drag coefficient of the quadrotor. Bluff-body drag is modeled as

$$\mathbf{f}_{bluff} = \frac{1}{2}\rho\|\Delta\mathbf{v}_\infty\|A_fC_D\Delta\mathbf{v}_\infty, \quad (4.38)$$

where $\Delta\mathbf{v}_\infty = R(\mathbf{V}_{probe} + \hat{\Omega}\mathbf{X}_{probe})$. Induced drag results from the lift force and induced angle of attack. Let $\alpha_{ind} = \arctan(\lambda_0/0.75)$ denote the induced angle of attack (using, for simplicity, the average angle, rather than integrating across the blade), which results from the velocity of the wind relative to the rotating blade; $\alpha_{eff} = \alpha_{geo} - \alpha_{ind}$ is the effective angle of attack; and α_{geo} is the geometric angle of attack resulting from the blade pitch relative to the plane of the hub. Define N_r as the number of rotors on the vehicle, N_b as the number of blades per rotor, and \bar{r} as the length of the rotor blade. Induced drag is

$$\mathbf{f}_{ind} = N_r \frac{N_b}{2\pi} \int_0^{2\pi} \int_0^{\bar{r}} \frac{1}{2}\rho(\omega r + S_\psi(\Delta\mathbf{v}_\infty \cdot \mathbf{u}_1))^2 c C_{l_\alpha} \alpha_{eff} S_{\alpha_{ind}} S_\psi dr d\psi \mathbf{u}_1, \quad (4.39)$$

which is then integrated along the length of the blade and around one rotor revolution. To avoid the multivariable integration, the induced angle of attack term α_{ind} in Eqn. (4.39) is simplified by assuming uniform inflow (which has shown to be sufficiently accurate for this term, compared to the flap angles where linear inflow was necessary), using the mean velocity of the blade, neglecting the change in velocity due to wind, and assuming the angle is small, such that $\alpha_{ind} = 2\lambda_0$. Additionally, assume a constant effective angle of attack $\alpha_{eff} = \theta_0 + (3/4)\theta_{tw} - \alpha_{ind}$, which yields the following:

$$\mathbf{f}_{ind} \approx N_r \frac{N_b}{4} \rho c C_{l_\alpha} \alpha_{eff} S_{\alpha_{ind}} \omega \bar{r}^2 (\Delta\mathbf{v}_\infty \cdot \mathbf{u}_1) \mathbf{u}_1. \quad (4.40)$$

The drag force is incorporated in \mathbf{b}_{3d} and thrust force is correspondingly chosen

as

$$f_{thrust} = (-k_x \mathbf{e}_x - k_v \mathbf{e}_v + mg \mathbf{e}_3 + m \ddot{\mathbf{x}}_d - \mathbf{f}_{aero}) \cdot \mathbf{b}_3. \quad (4.41)$$

The desired heading \mathbf{b}_{1_d} is prescribed in the outer loop, assuming that \mathbf{b}_{1_d} is not parallel to \mathbf{b}_{3_d} . The desired attitude of the quadrotor transmitted to the inner-loop controller is $R_d = [\mathbf{b}_{2_d} \times \mathbf{b}_{3_d}, \mathbf{b}_{2_d}, \mathbf{b}_{3_d}] \in SO(3)$, where $\mathbf{b}_{2_d} = (\mathbf{b}_{3_d} \times \mathbf{b}_{1_d}) / \|\mathbf{b}_{3_d} \times \mathbf{b}_{1_d}\|$. Additionally, assume $\|mg \mathbf{e}_3 + m \ddot{\mathbf{x}}_d\| < B$ for a given positive constant B . The complete error dynamics of the system are

$$\begin{aligned} \dot{\mathbf{e}}_R &= \frac{1}{2} (\text{tr} \{R^T R_d\} I - R^T R_d) \mathbf{e}_\Omega \\ \dot{\mathbf{e}}_\Omega &= J^{-1} \left(-\hat{\Omega} J \Omega + \mathbf{M}_{thrust} + \mathbf{M}_{aero} \right) + \hat{\Omega} R^T R_d \Omega_d - R^T R_d \dot{\Omega}_d \\ m \dot{\mathbf{e}}_x &= m \dot{\mathbf{x}} - m \dot{\mathbf{x}}_d = m \mathbf{v} - m \mathbf{v}_d \\ m \dot{\mathbf{v}} &= m \ddot{\mathbf{x}} - m \ddot{\mathbf{x}}_d = -mg \mathbf{e}_3 + \mathbf{f}_{thrust} + \mathbf{f}_{aero}. \end{aligned} \quad (4.42)$$

The stability of the dynamics in Eqn. (4.42) relies on the convergence of the attitude dynamics in order to ensure that \mathbf{b}_3 follows \mathbf{b}_{3_d} . Almost global exponential stability of the attitude dynamics is described above using the moment input in Eqn. (4.14). Furthermore, for stability of the complete dynamics initial attitude error must be less than $\pi/2$ [32], corresponding to the configuration error function $\Psi < 1$. Applying the control force \mathbf{f}_{thrust} and moment \mathbf{M}_{thrust} defined in Eqs. (4.41) and (4.14), the dynamics in Eqn. (4.42) are exponentially stable according to Proposition 4.5, with the region of attraction characterized by $\Psi(R(0), R_d(0)) \leq \psi_1 < 1$, where ψ_1 is a constant.

Proposition 4.5 ([32] Exponential stability of the complete error dynamics) *Consider the control force f_{thrust} and moment \mathbf{M}_{thrust} defined in Eqs. (4.41) and (4.14). Suppose the initial condition satisfies*

$$\Psi(R(0), R_d(0)) \leq \psi_1 < 1 \quad (4.43)$$

for a fixed constant ψ_1 . Define $W_1, W_{12}, W_2 \in \mathbb{R}^{2 \times 2}$ to be

$$W_1 = \begin{bmatrix} \frac{c_1 k_x}{m} & -\frac{c_1 k_v}{2m} \\ -\frac{c_1 k_v}{2m}(1 + \alpha) & k_v(1 - \alpha) - c_1 \end{bmatrix}, \quad (4.44)$$

$$W_{12} = \begin{bmatrix} k_x e_{V_{\max}} + \frac{c_1}{m} B & 0 \\ B & 0 \end{bmatrix}, \quad (4.45)$$

$$W_2 = \begin{bmatrix} c_2 k_R & -\frac{1}{2} c_2 k_\Omega \\ -\frac{1}{2} c_2 k_\Omega & \lambda_{\min}(J) k_\Omega - c_2 \end{bmatrix}. \quad (4.46)$$

where $\alpha = \sqrt{\psi_1(2 - \psi_1)}$, $e_{V_{\max}} = \max\{\|e_V(0)\|, \frac{B}{k_v(1 - \alpha)}\}$, $c_1, c_2 \in \mathbb{R}$. For any positive constants k_x, k_v , we choose positive constants c_1, c_2, k_R, k_Ω such that

$$c_1 < \min \left\{ k_v(1 - \alpha), \frac{4mk_x k_v(1 - \alpha)}{k_v^2(1 - \alpha)^2 + 4mk_x}, \sqrt{k_x m} \right\}, \quad (4.47)$$

$$c_2 < \min \left\{ \lambda_{\min}(J) k_\Omega, \frac{4\lambda_{\min}(J) k_\Omega k_R}{k_\Omega^2 + 4k_R}, \lambda_{\min}(J) \sqrt{k_R}, \lambda_{\max}(J) \sqrt{\frac{2k_R}{2 - \psi_1}} \right\}, \quad (4.48)$$

$$\lambda_{\min}(W_2) > \frac{4\|W_{12}\|^2}{\lambda_{\min}(W_1)}. \quad (4.49)$$

Then, the zero equilibrium of the tracking errors of the complete system is exponentially stable. The region of attraction is characterized by Eqn. (4.43) and

$$\|e_\Omega(0)\|^2 < \frac{2}{\lambda_{\min}(J)} k_R (1 - \lambda_{\min}(J) \Psi(R(0), R_d(0))). \quad (4.50)$$

Furthermore, although Proposition 4.5 requires that the initial attitude error be less than $\pi/2$, the attitude error function Ψ is guaranteed to exponentially decrease [32], and will therefore enter the region of attraction in a finite time, by which almost global exponential attractiveness of the complete dynamics is guaranteed by Proposition 3 of [32].

4.5 Six Degree-of-Freedom Position and Attitude Simulation

The variable-gain algorithm described by Corollary 4.4 is also included for the 6DOF quadrotor, and shows improved simulated responses to a step commands in position. Figure 4.8 shows a step command from initial conditions $(-8, 1, 0)$ to $(x, y, z) = (0, 0, 10)$ m hovering above the origin. Figure 4.9 shows a step command from initial conditions $(-8, -6, 0)$ m to the same final position. In both cases, the quadrotor reaches the goal with and without the variable gain algorithm, however, in the case starting closer to the desired position, the variable gain algorithm enables the vehicle to take a more direct path to the desired location. In the case beginning farther from the initial position, using variable gains enables the vehicle to more quickly and effectively approach the desired position, whereas the fixed-gain case struggles to allocate authority and yields a more erratic trajectory.

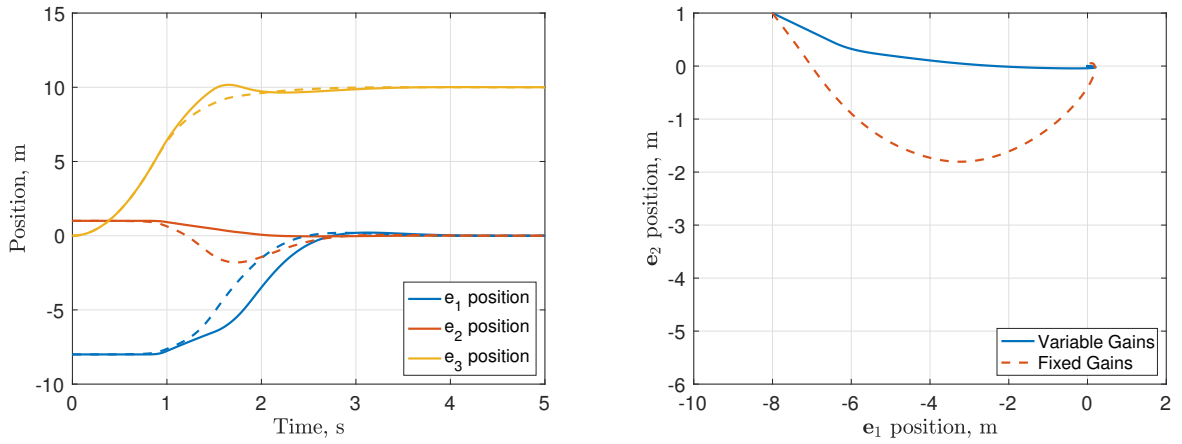


Figure 4.8: Simulated position control with and without variable gains. Initial location $(-8, 1, 0)$ to desired location $(0, 0, 10)$. Left: e_1 , e_2 and e_3 positions. Right: Overhead view of e_1 and e_2 position.

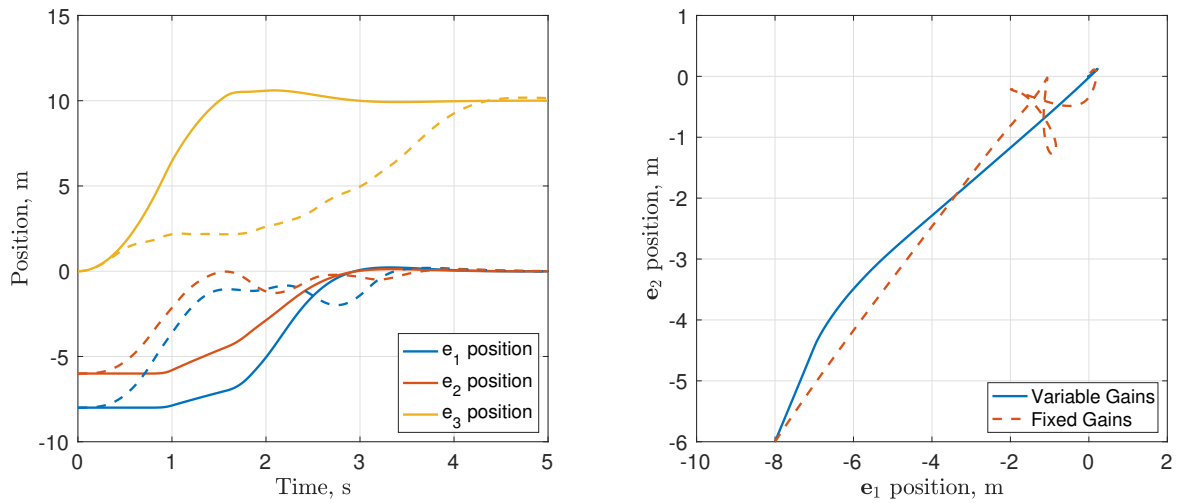


Figure 4.9: Simulated position control with and without variable gains. Initial location $(-8, -6, 0)$ to desired location $(0, 0, 10)$. Left: e_1 , e_2 and e_3 positions. Right: Overhead view of e_1 and e_2 position.

Chapter 5: Linear Control of Attitude and Position

In addition to the nonlinear control strategy presented above, this work investigates the benefits of adding flow sensing to a more traditional linear controller. The linear model of the quadrotor is found using system identification techniques in the frequency domain. The model is used to calculate stability and performance criteria for the closed-loop controller, whose gains are optimized based on handling qualities criteria. This work was presented in the 2019 VFS Autonomous VTOL Technical Meeting [47].

5.1 Model Identification

Modeling results are presented for the longitudinal degree of freedom (the process is the same for each of the other degrees of freedom). Define inertial frame $\mathcal{I} \triangleq (O, \mathbf{e}_1, \mathbf{e}_2, \mathbf{e}_3)$ in a north-west-up orientation with O at a known point on the ground, and body frame $\mathcal{B} \triangleq (O', \mathbf{b}_1, \mathbf{b}_2, \mathbf{b}_3)$ in a forward-left-up orientation with O' at the center of mass of the quadrotor, as shown in Figure 2.1. In the longitudinal degree-of-freedom, u is the velocity along \mathbf{b}_1 , q is the pitch rate along \mathbf{b}_2 , θ is the pitch angle along \mathbf{b}_2 , and Δ_u is the wind velocity in the \mathbf{b}_1 direction. Let X_u and M_u be the linear acceleration and angular acceleration response to velocity u ,

respectively. We also define X_{Δ_u} and M_{Δ_u} as the linear and angular acceleration response to wind Δ_u , respectively. The state-space description of the system is

$$\begin{bmatrix} \dot{u} \\ \dot{q} \\ \dot{\theta} \end{bmatrix} = \begin{bmatrix} X_u & 0 & g \\ M_u & 0 & 0 \\ 0 & 1 & 0 \end{bmatrix} \begin{bmatrix} u \\ q \\ \theta \end{bmatrix} + \begin{bmatrix} 0 \\ M_{\theta_{1s}} \\ 0 \end{bmatrix} \theta_{1s}(t - \tau_{1s}) + \begin{bmatrix} X_{\Delta_u} \\ M_{\Delta_u} \\ 0 \end{bmatrix} \Delta_u, \quad (5.1)$$

$$y = \begin{bmatrix} 1 & 0 & 0 \\ 0 & 1 & 0 \\ 0 & 0 & 1 \\ 0 & 0 & 0 \end{bmatrix} \begin{bmatrix} u \\ q \\ \theta \end{bmatrix} + \begin{bmatrix} 0 \\ 0 \\ 0 \\ 1 \end{bmatrix} \Delta_u. \quad (5.2)$$

System identification is performed with CIFER[®], which uses frequency sweeps over each channel to develop a linear model fit. Sweep profiles are performed automatically by inserting a frequency chirp into the flight-controller software. Chirps sweep from 0.62 rad/s to over 100 rad/s; an example is shown in Figure 5.1. Large spikes in the data are user inputs to limit translational drift.

The resulting model fit to the flight data is shown in Figure 5.2. Stability derivatives are presented in Table 5.1, as well as Cramer-Rao bounds and insensitivities showing the level of confidence of the identification [42]. The value for X_u has been fixed based on insensitivity analysis. The model has also been validated in the time domain against independent data from separate flight tests, showing good agreement in Figure 5.3.

It was initially predicted that the effect of wind moving over the quadrotor would be equivalent to the effect of the quadrotor moving forward in air, such that

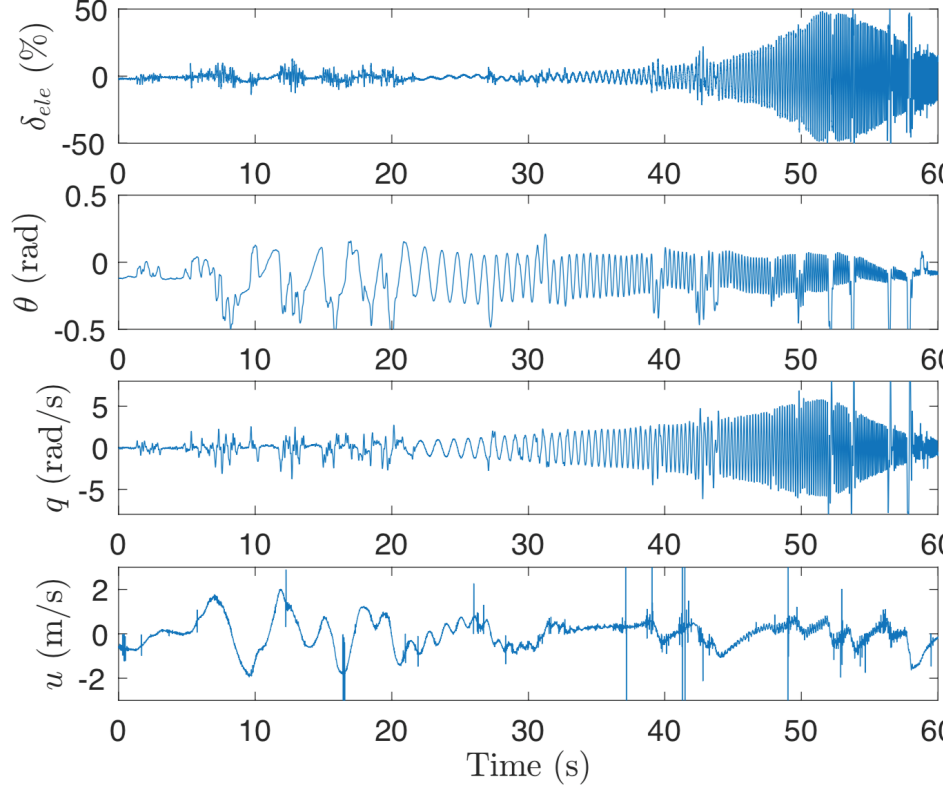


Figure 5.1: Chimp data for longitudinal degree of freedom used as input to CIPHER[®]

$X_{\Delta_u} = -X_u$ and $M_{\Delta_u} = -M_u$. Initial experimental testing using this assumption showed that the quadrotor was unable to completely address the magnitude of the moment generated by the wind. A second attempt to characterize the value of the gust stability derivative applied previous experimental data from the force-torque testing and wind tunnel blade-flap experiments that informed Fig. 3.6. With this data, blade-flap angle was used to calculate the moment acting on the vehicle. The linear relationship of blade-flap angle to wind speed led to a linear relationship between the moment produced and the wind speed, with a slope of 0.0154 (Nm)/(m/s), corresponding to $M_{\Delta_u} = 22.0$, approximately twice the magnitude of M_u . The translational stability derivative X_{Δ_u} was similarly increased, though with

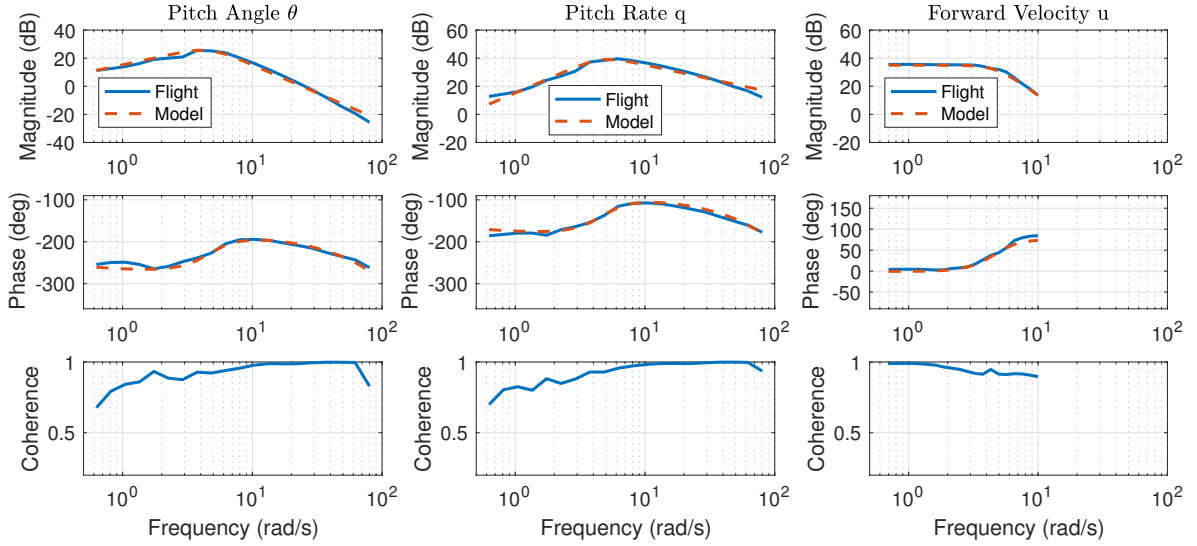


Figure 5.2: Model-data agreement using stability derivatives identified in CIFER[®]

Table 5.1: Stability Derivatives

Parameter	Value	C-R %	Insensitivity %
X_u	-0.05	-	-
M_u	-10.26	4.54	1.59
$M_{\theta_{1s}}$	5.79	3.16	1.09
τ_{1s}	0.0196	5.49	2.74

such a small initial value the change had a much smaller effect than that of the rotational stability derivative.

5.2 Controller Design

The quadrotor flight controller structure shown in Figure 5.4 uses a fast inner-loop running at 2kHz to control the attitude dynamics, and a slower outer-loop running at 100Hz to control the position and heading dynamics. The outer loop applies gains to velocity and position in proportional-integral (PI) control, and also

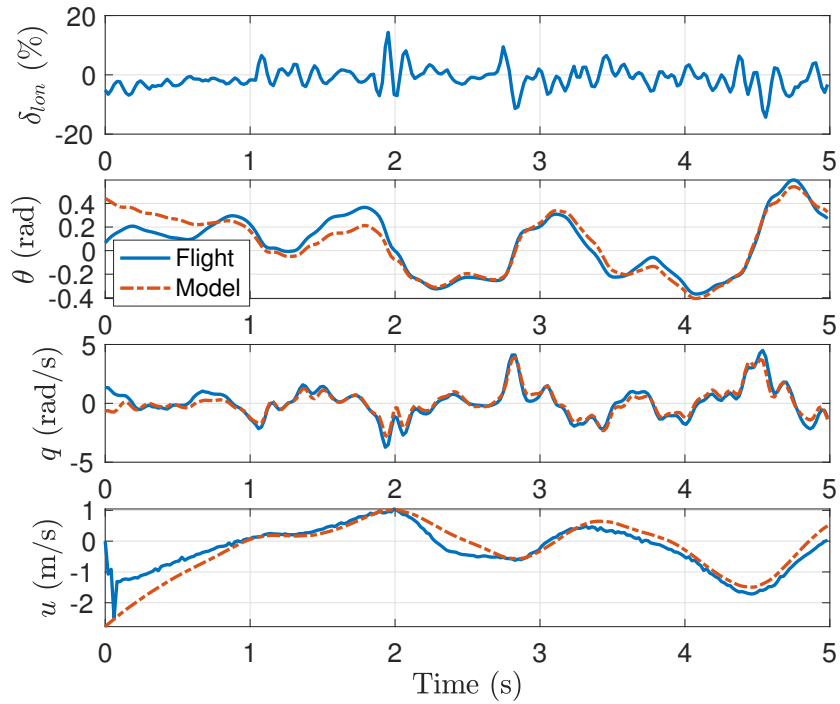


Figure 5.3: Model validation against time-series data

uses a saturation function to limit the maximum desired velocity produced by the position error. The gain-adjusted velocity error is transmitted to the inner loop, where the onboard wind measurements are incorporated to produce the desired attitude. Gains are applied to attitude and rate in a proportional-derivative (PD) controller and combined with flow feedback to produce the final inputs to the motors.

To implement the PID controller, position and speed are fed back to the outer loop; and attitude, attitude rate, and wind speed to the inner loop. This example shows the development in the longitudinal direction (the process for each other degree of freedom is similar). To limit the maximum reference speed, desired position

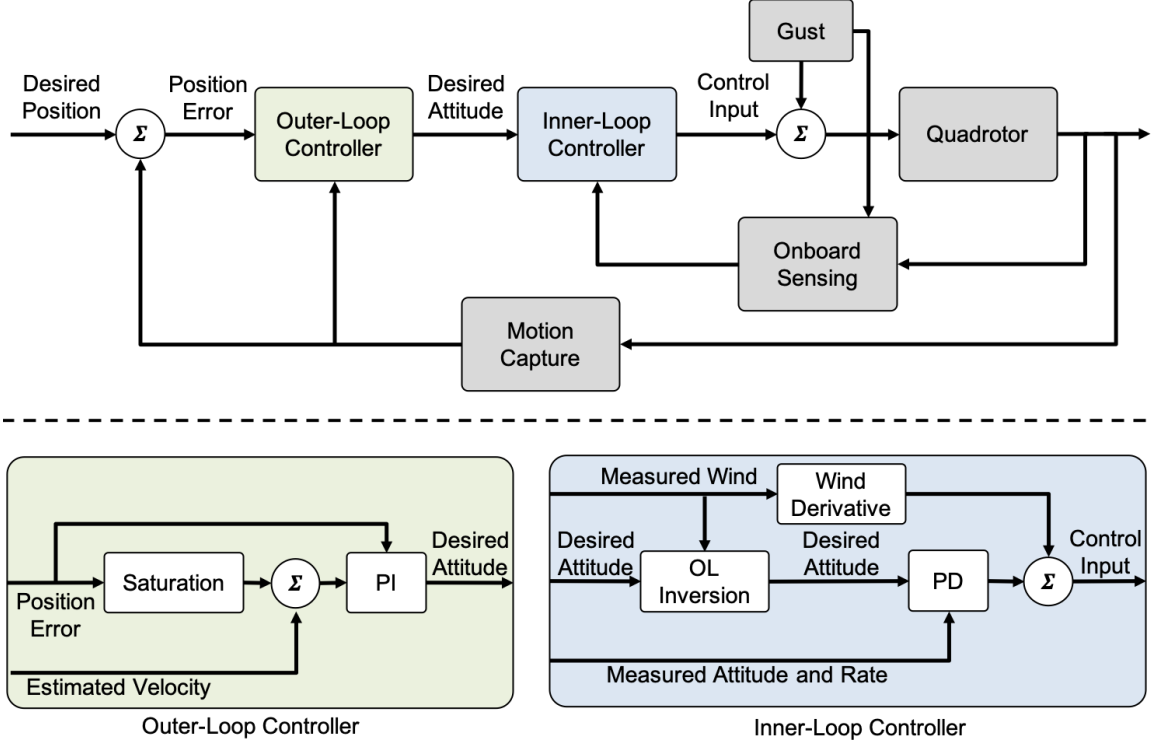


Figure 5.4: Quadrotor linear control architecture

is passed through a saturation function, i.e.,

$$u_d = \text{sat}(K_{\text{sat}}(x - x_d)), \quad (5.3)$$

where K_{sat} sets the slope of the saturation function. Position and velocity errors are then calculated as

$$e_u = u - u_d, \quad (5.4)$$

$$e_x = x - x_d,$$

and a PI control gains are applied to yield the desired dynamics, i.e.;

$$\dot{u}_d = -K_u e_u - K_x e_x. \quad (5.5)$$

Inserting Equation (5.5) into the dynamics (5.1) yields

$$\dot{u} = X_u u + g\theta + X_{\Delta_u} \Delta_u = -K_u e_u - K_x e_x. \quad (5.6)$$

Taking θ as the control input to the outer loop system and solving for the desired pitch angle yields

$$\theta_d = \frac{1}{g}(-K_u e_u - K_x e_x - X_u u - X_{\Delta_u} \Delta_u). \quad (5.7)$$

The identified value for θ_d then drives the errors for the inner-loop control strategy,

$$e_\theta = \theta - \theta_d \quad (5.8)$$

and

$$e_q = q - \frac{d}{dt}\theta_d. \quad (5.9)$$

The desired dynamics are:

$$\dot{q} = -K_q e_q - K_\theta e_\theta, \quad (5.10)$$

and substituting into the system dynamics (5.1) yield,

$$\dot{q} = M_u u + M_{\theta_{1s}} \theta_{1s} + M_{\Delta_u} \Delta_u = -K_q e_q - K_\theta e_\theta. \quad (5.11)$$

Rearranging, with θ_{1s} as the input, the value sent to the mixer is

$$\theta_{1s} = \frac{1}{M_{\theta_{1s}}}(-K_q e_q - K_\theta e_\theta - M_u u - M_{\Delta_u} \Delta_u). \quad (5.12)$$

Using separate onboard and offboard sensing necessitates additional control development. The desired pitch angle must be separated into independent outer- and inner-loop components, where the outer loop component θ_{d_1} uses the position and velocity data only available through motion capture, and the inner loop component θ_{d_2} uses the wind data only available from the onboard flow sensors, such that $\theta_d = \theta_{d_1} + \theta_{d_2}$. The stabilizing portion of the feedback can be calculated in the outer

loop as $\theta_{d_1} = (1/g)(-K_u e_u - K_x e_x)$, and the portion cancelling undesired dynamics is calculated in the inner loop as $\theta_{d_2} = (1/g)(-X_u u - X_{\Delta_u} \Delta_u)$. Although the onboard controller does not have access to accurate velocity data, the flow probes measure the combination of wind speed and flight speed, such that the actual measurement $\Delta'_u = \Delta_u - u$. Based on the initial assumption that $X_{\Delta_u} \approx -X_u$, the desired value can be calculated as $X_{\Delta_u} \Delta'_u = X_{\Delta_u} \Delta_u - X_{\Delta_u} u \approx X_{\Delta_u} \Delta_u + X_u u$. The updated value for X_{Δ_u} based on the blade-flapping experiments overpredicts the effect of the quadrotor velocity, but is a necessary compromise due to the nature of the flow probes. The final inner-loop input similarly approximates $M_{\Delta_u} \approx -M_u$, such that

$$\theta_{1s} = \frac{1}{M_{\theta_{1s}}}(-K_q e_q - K_\theta e_\theta - M_{\Delta_u} \Delta'_u). \quad (5.13)$$

5.3 Controller Optimization

A Simulink model of the controller in combination with the identified linear model were used to identify optimal gains using the CONDUIT[®] environment. CONDUIT[®] requires users to choose a number of specifications relating to handling qualities stability and performance, then uses a multiobjective optimization engine to adjust gains such that each of the prescribed handling qualities specifications is achieved. More details on the CONDUIT[®] software are available in [43]. Handling qualities are characterized as level one, two, or three, with one as the best and three as the worst. The CONDUIT[®] software is designed to achieve level one handling qualities for all specifications, while also minimizing actuator usage. Hard specifications (H) address stability and are required to be met by the optimization,

soft specifications (S) address performance based metrics and are desirable but not required, and summed objective (J) specifications are designed to reduce actuator usage and are correspondingly minimized.

Nominal handling qualities specifications in CONDUIT[®] are designed for full-scale manned aircraft. The small size and unmanned nature of quadrotor UAS lead to different handling qualities requirements, so the CONDUIT[®] specifications have been adjusted based on previous work using CONDUIT[®] for small quadrotor UAS [41, 44]. Additional adjustments were also made based on pilot feedback and flight performance. The specifications to which the gains were optimized for the longitudinal outer loop for position control are shown in Table 5.2, with comments addressing adjustments to handling qualities boundaries. The resulting handling qualities window is shown in Figure 5.5, and shows that each of the specifications meets level 1 requirements. The corresponding characteristics of the control law design are shown in Table 5.3.

Table 5.2: Handling Qualities Specifications

Parameter	Description	Type	Std. Bounds?	Comments
EigLcG1	Eigenvalues	Hard	Y	
StbMgG1	Stability Margins	Hard	N	L1/L2 at 4dB, 20 deg
NicMgG1	Nichols Margins	Hard	N	L1/L2 at 160 deg
DrbRoX1	Disturbance Rejection Bandwidth	Soft	N	L1/L2 at 1.33 rad/s
DrpAvH1	Disturbance Rejection Peak	Soft	N	L1/L2 at 3.33 rad/s
CrsMnG2	Minimum Crossover Frequency	Soft	N	L1/L2 at 4.33 rad/s
CrsLnG1	Crossover Frequency	Sum. Obj.	N	L1/L2 at 10 rad/s
RmsAcG1	Actuator RMS	Sum. Obj.	Y	

Table 5.3: Control Law Performance

Controller	Gain Margin [dB]	Phase Margin [deg]	Crossover Freq. [rad/s]	DRB [rad/s]
Pitch Attitude	9.66	21.8	25.8	11.9
Long. Position	4.10	24.8	4.33	1.33

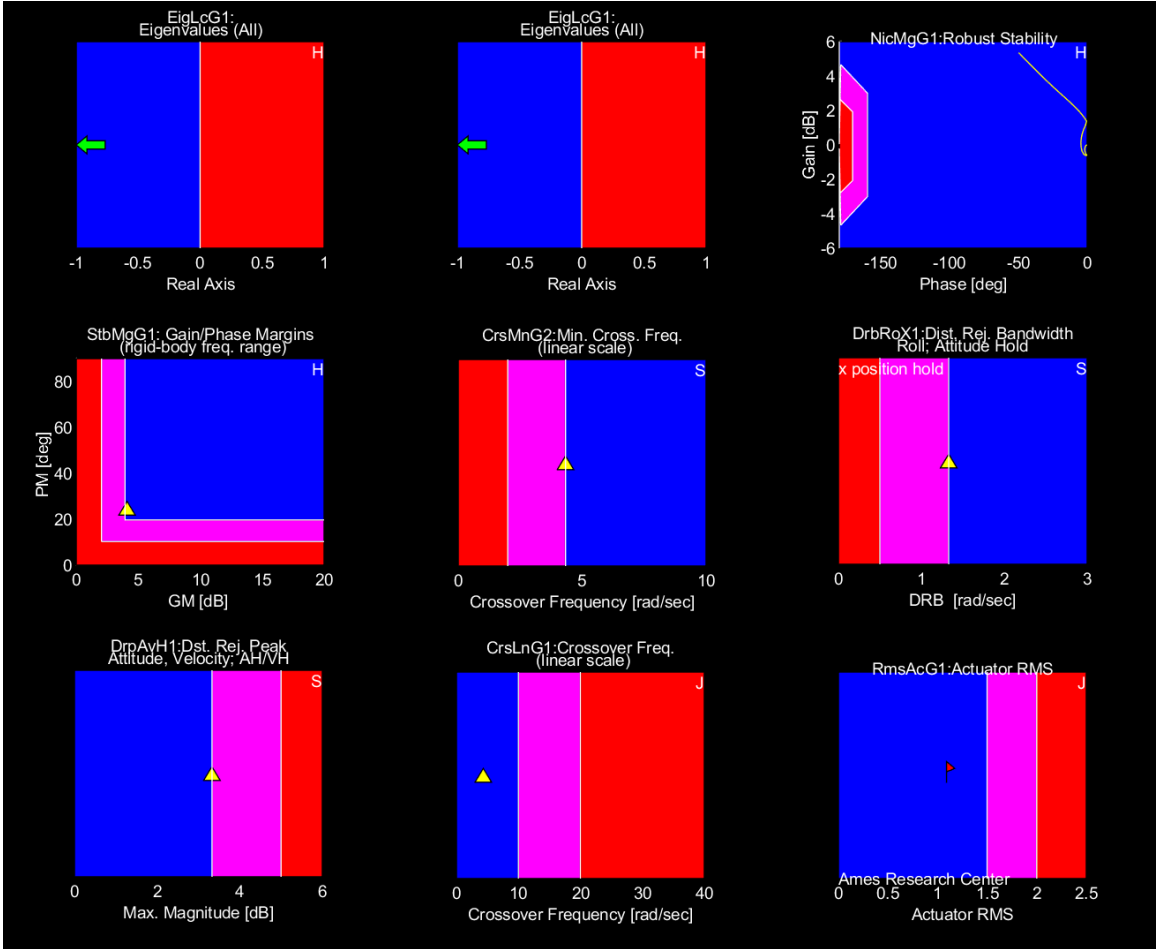


Figure 5.5: CONDUIT[®] handling qualities window. Level one in blue, level two in pink, level three in red. Triangles and flags indicate the value of the handling quality, green arrows indicate an off-screen value, and the line in Nichols robust stability indicates the value across simultaneous changes in gain and phase.

Chapter 6: Quadrotor Control Experimental Results

Experimental testing was performed for each of the controllers developed in this work: nonlinear attitude, nonlinear position and attitude, and linear position and attitude. The controllers are implemented on a custom quadrotor, and tested in a gust-generation environment. Experimental saturation results are also presented for the attitude-only nonlinear case. This chapter contains work presented in the 2019 AIAA SciTech Forum [48], as well as the 2019 VFS Autonomous VTOL Technical Meeting [47].

6.1 Nonlinear Controller

6.1.1 Three Degree-of-Freedom Attitude Control

Initial experimental testing of both saturation performance and the effect of flow sensing was performed on a 3DOF custom quadrotor test stand, shown in Fig. 6.1. A 3D-printed ball joint attaches to the center of the vehicle to constrain its translation. Rotation is unconstrained in yaw, and limited to ± 60 degrees in roll and pitch. Saturation performance is experimentally tested by attaching a zip-tie to one arm of the quadrotor and pulling by hand to produce an impulse. In this case the



Figure 6.1: Quadrotor experimental attitude test stand

linearization effort did not saturate the system, however, the gains in the controller exceeded the control authority available for stabilization and thus saturated the motors. The results are shown in Fig. 6.2 for both static and variable gain cases, where dash-dot lines show the static case in the top plot, and corresponding motor inputs are in the middle plot. Variable gain data are shown as a solid line in the top plot with motor inputs in the bottom plot. The dynamic response of the quadrotor in both cases is successful and nearly identical. Motor commands are also similar in the way the motors respond and in the length of time that motor inputs are on the bounds, however, the variable gains allow the system to maintain the desired direction of the moment rather than naively saturating multiple motors at once. The benefits on a position-constrained test-stand are minimal, though

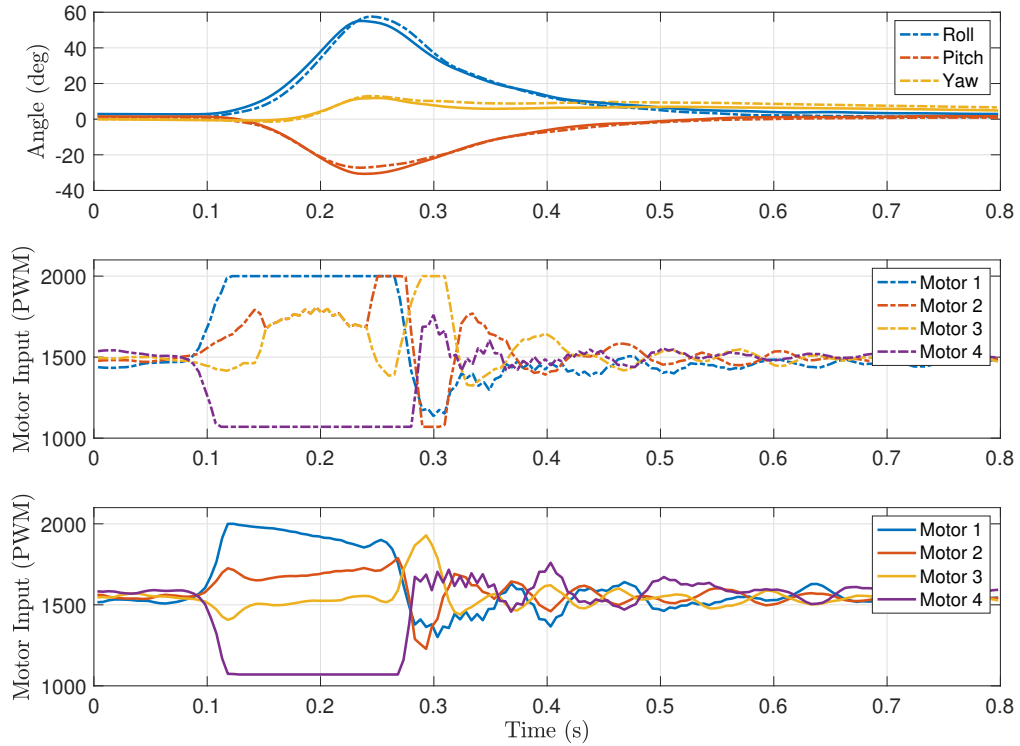


Figure 6.2: Experimental quadrotor response to motor saturation; top: variable gain (solid) and static (dash-dot), middle: static gain motor input, bottom: variable gain motor input

previous simulations show the benefits are greater in free-flight where an incorrect moment has greater consequences.

For gust rejection tests, the quadrotor test stand was placed in front of the gust generator in Fig. 2.6, consisting of a set of Dyson fans behind remotely actuated blinds controlled through Labview using an Arduino. In addition to the on-board flow probes, a separate Testo 405i hot-wire anemometer was mounted to the test-stand frame to provide ground-truth measurements at 1 Hz. Before opening the blinds, the quadrotor was armed, initialized with $\mathbf{e}_1 = -\mathbf{b}_1$, and the throttle set just

above the vehicle weight (noted when the vehicle took the slack on the ball joint). Then the blinds were opened and closed in a square wave pattern with a period of four seconds for the first test, and eight seconds for the second test. Results from the first test, in Fig. 6.3, show improved performance using flow sensing when directly compared to the same controller without flow sensing, as well as comparing against the stock PID controller in the Cleanflight software. With active flow sensing the vehicle shows little to no pitching in response to wind gusts, though it also responds to the sensor noise and thus shows more inconsistency than the controller without flow sensing. The response without flow sensing shows a very clear and consistent correlation to the wind gusts due to the absence of any kind of integral term in the controller. The PID controller shows the greatest initial response, but returns to equilibrium due to the presence of an integral term that also causes the vehicle to pitch toward the fans after the gust ceases.

The second test, in Fig. 6.4, uses a longer period square wave and higher wind speed to show results when the wind and quadrotor have more time to reach a steady state. A stronger wind with a longer period highlights more clearly the quadrotor's reaction to changes in the wind for each controller, which are less obvious in lower wind with a shorter period. The response for the feedback linearization case without flow feedback remains largely unchanged. The PID overshoot at the end of the gust matches that at the beginning, though it is corrected quickly. The controller with flow feedback continues to show the least error, though in this case it shows slight forward pitching at the end of each gust. The lower subfigures of Figs. 6.3 and 6.4 both show that the rising edge of the square-wave gust is sharper and more abrupt

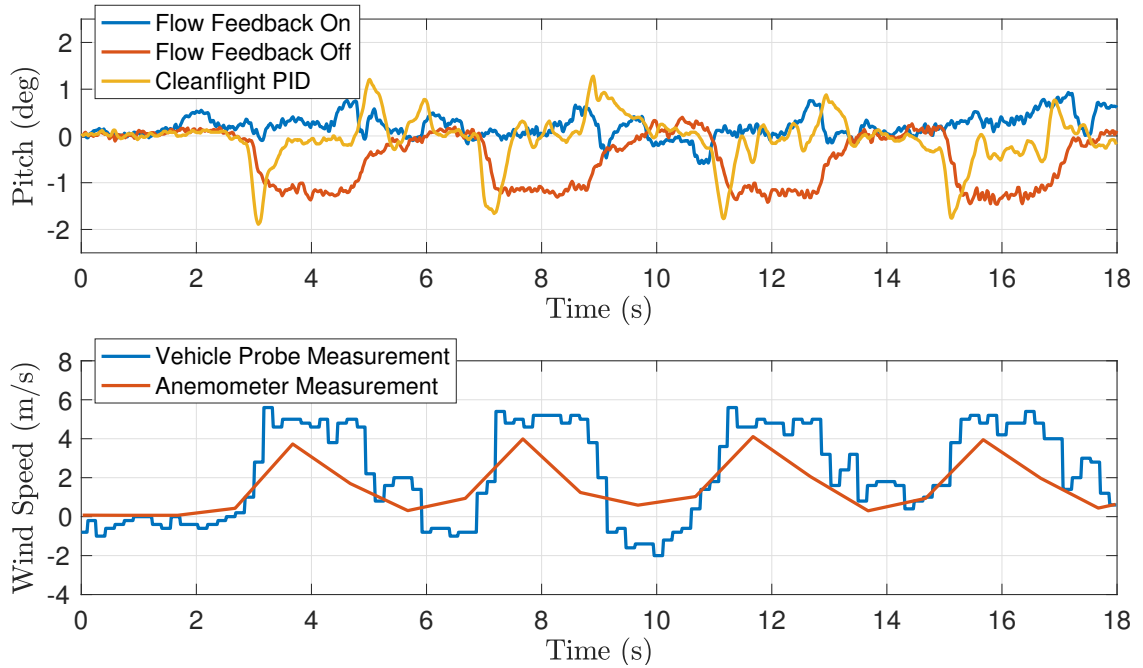


Figure 6.3: Experimental quadrotor response on attitude stand to 4 m/s gusts in the $\mathbf{e}_1 = -\mathbf{b}_1$ direction

than the falling edge, which may be why the quadrotor equipped with flow feedback shows a slightly degraded response to the falling edge.

The initial-response performance of each controller in the two tests is quantified in Fig. 6.5 using data from the first 0.5 seconds of each gust. The box plot shows the median as the central mark in each box, the 25th and 75th percentiles as the bottom and top of each box, and whiskers that extend to the most extreme data points. The initial response is analyzed because high initial error will lead to large translational error even if the attitude is able to recover. There is a small error and tight spread for the controller with flow feedback, high error and a tight spread for the controller without flow feedback, and moderate error with a very wide spread for the PID controller, highlighting the PID controller’s tendency to overshoot.

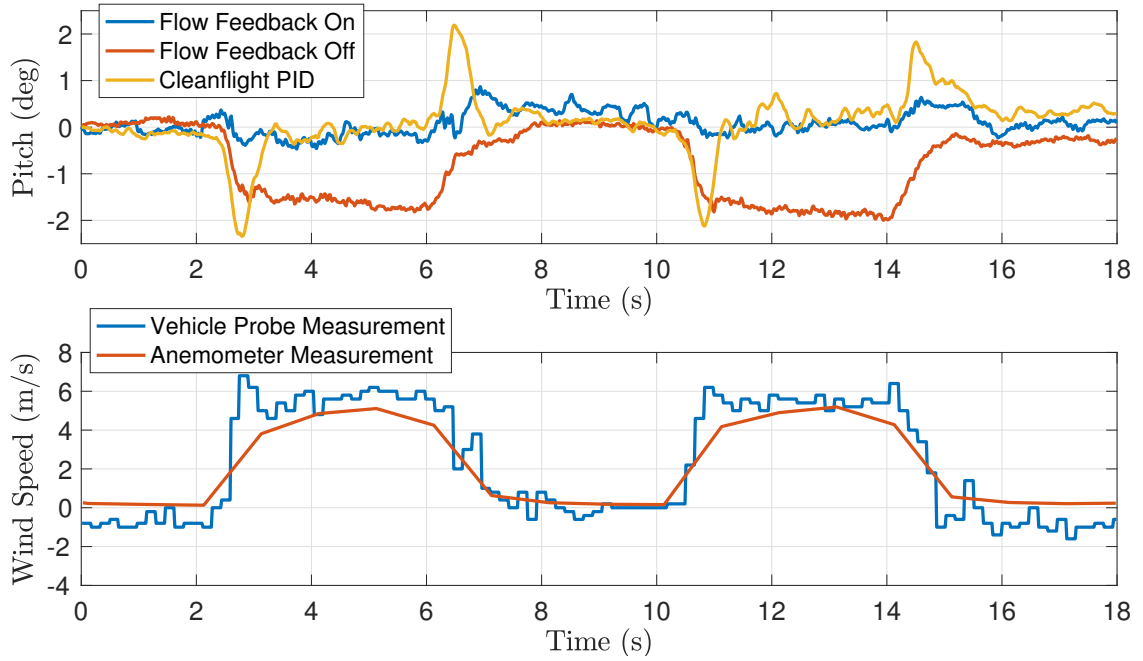


Figure 6.4: Experimental quadrotor response on attitude stand to 5 m/s gusts in the $\mathbf{e}_1 = -\mathbf{b}_1$ direction

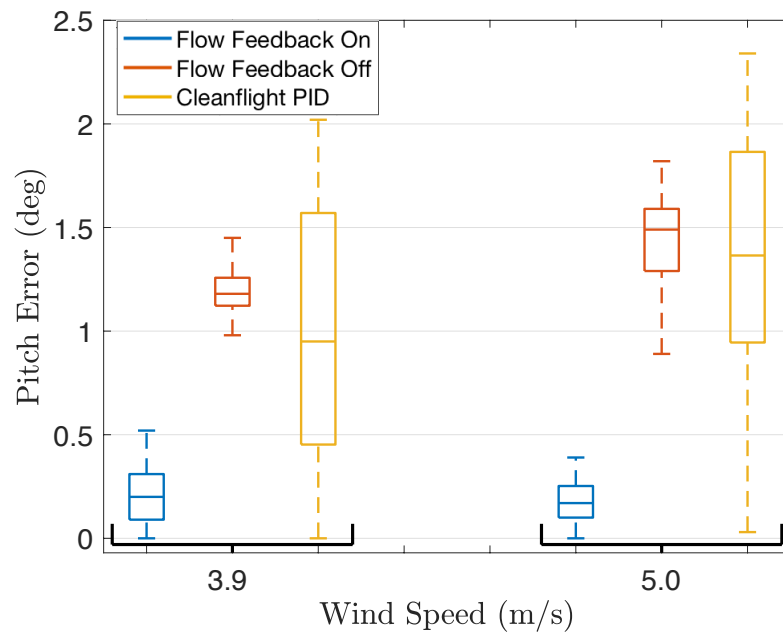


Figure 6.5: Initial pitch response of each controller for the two different wind speeds and gust frequencies

This data demonstrates that even in a reduced degree-of-freedom test-stand, there are clear improvements in gust rejection through the use of flow sensing. The quadrotor responds to the flow before it affects the vehicle, giving it an advantage over both other controllers, even when using an integral term. Flow sensors also avoid the windup associated with adding integral correction, giving a more consistent and predictable response in unsteady winds.

6.1.2 Six Degree-of-Freedom Position and Attitude Control

Similar tests to those described for the attitude stand are performed to investigate the effect of flow feedback on position control of a quadrotor in free-flight. For position testing, baseline wind speeds were established prior to flight using a separate Testo 405i hot-wire anemometer, then tests were initialized with the quadrotor facing the fans such that \mathbf{e}_1 aligns with \mathbf{b}_1 , with $\Delta\mathbf{v}_\infty$ along $-\mathbf{e}_1$. After initialization, the quadrotor was flown to a specific position where it was commanded to hold station, then the blinds were opened and closed in a square-wave pattern to produce gusts.

These tests utilize the outer-loop controller described in Section 4.4 and compare the same three inner-loop controllers as were tested for attitude experiments: $SO(3)$ control with flow feedback, $SO(3)$ control without flow feedback, and the standard PID controller in the Cleanflight software, which also lacks flow feedback. The inner-loop for each controller was tuned by hand to achieve a fast response while maintaining stability. Tests in Figs. 6.6 and 6.8 were subjected to a 4 m/s

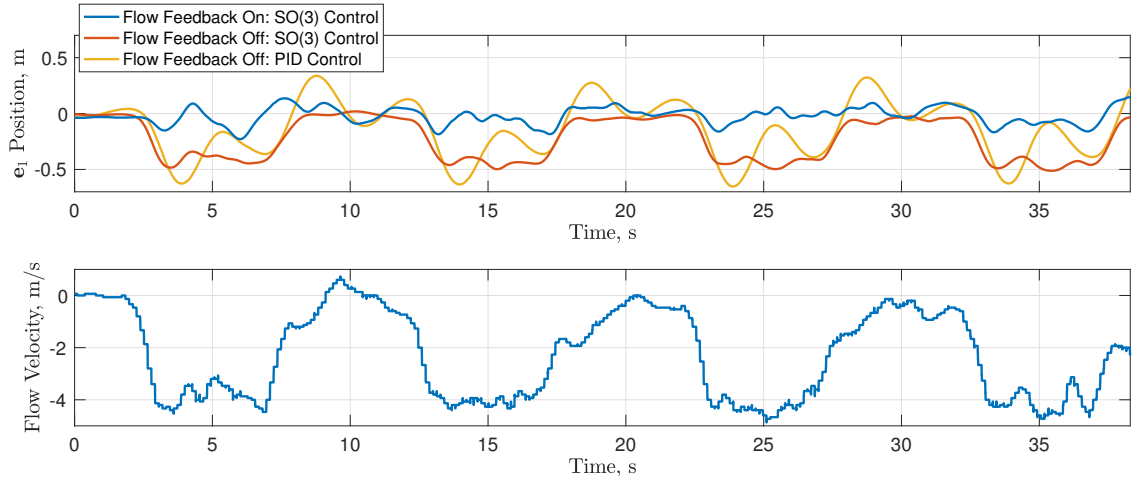


Figure 6.6: Experimental quadrotor e_1 position error in response to 5 s duration 4 m/s gusts in the $-\mathbf{e}_1$ direction. All three controllers use the same outer-loop control, and flow velocity is measured onboard using a custom flow probe.

gust in a square-wave pattern with a period of 10 seconds, and tests in Figs. 6.7 and 6.9 show gusts at the same speed with a period of 4 seconds. Figures 6.6 and 6.7 show the time series e_1 error against the wind speeds measured onboard by the fore-aft flow probe. Figures 6.8 and 6.9 show the position of the vehicle from an overhead view in the $\mathbf{e}_1 - \mathbf{e}_2$ plane on the left, and a side view in the $\mathbf{e}_1 - \mathbf{e}_3$ plane on the right, together showing the full three-dimensional response of the quadrotor to wind. Figure 6.10 shows a box plot of the horizontal Euclidean-distance error for the duration of the test, comparing each of the three controllers at the two different gust frequencies to highlight the statistical differences. The box plot displays the median, 25th and 75th percentiles as the top and bottom of each box, whiskers extending to non-outlier points, and additional dots showing outliers.

For both flow periods, Figs. 6.6 through 6.9 show the best performance when

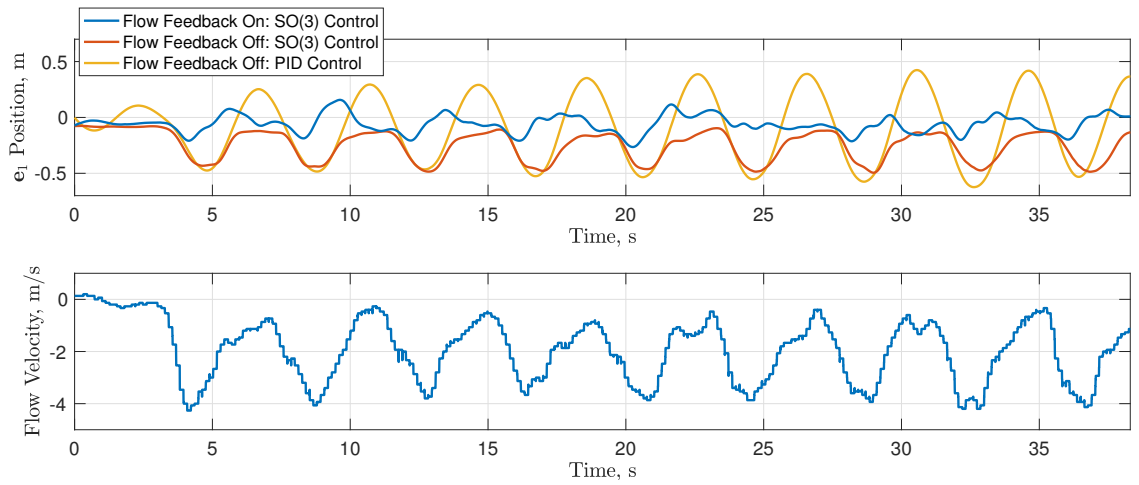


Figure 6.7: Experimental quadrotor e_1 position error in response to 2 s duration 4 m/s gusts in the $-e_1$ direction. All three controllers use the same outer-loop control, and flow velocity is measured onboard using a custom flow probe.

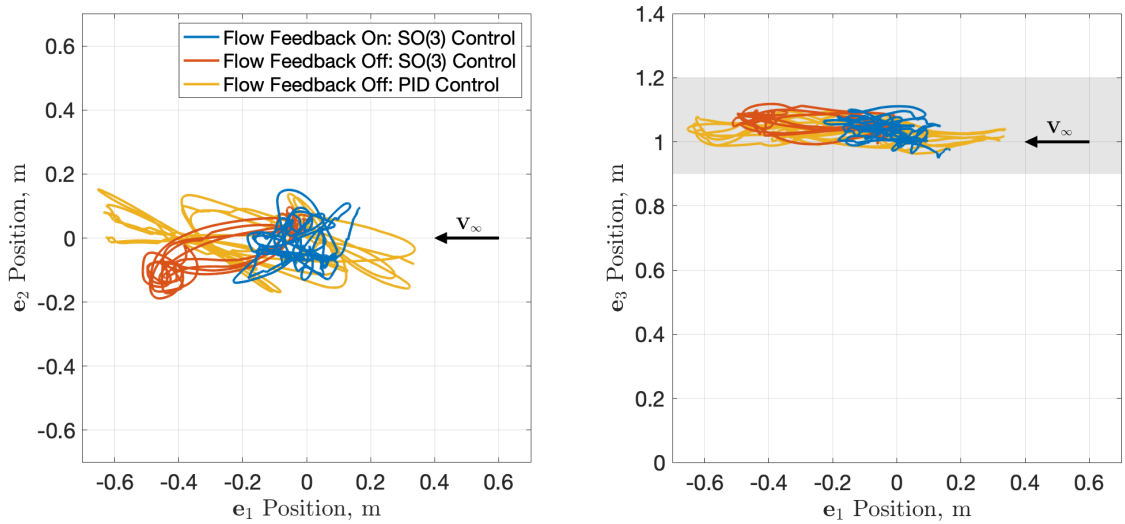


Figure 6.8: Experimental quadrotor position response to 5 s duration 4 m/s gusts in the $-e_1$ direction. All three controllers use the same outer-loop control. Grey area represents desired altitude based on fan output.

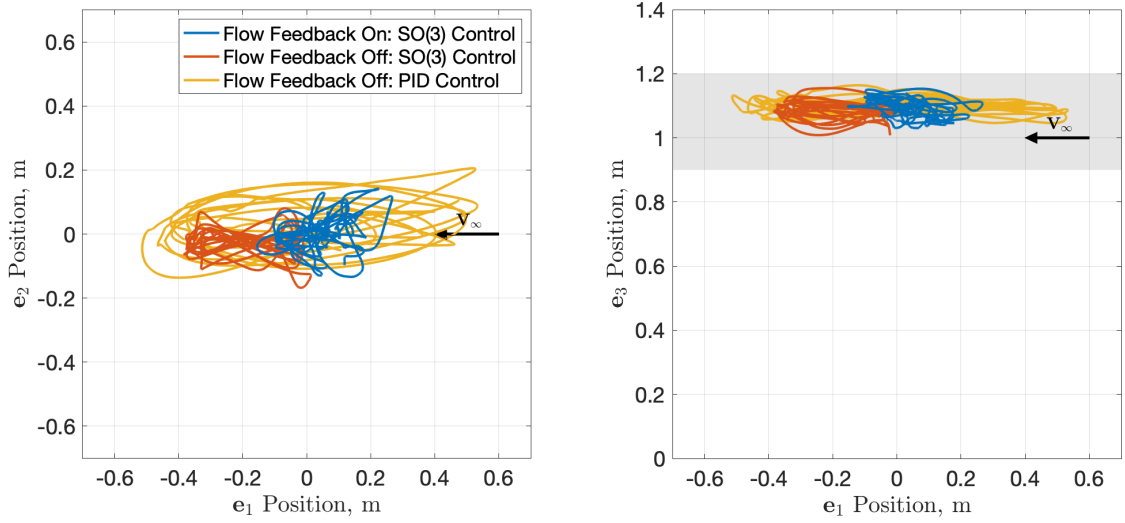


Figure 6.9: Experimental quadrotor position response to 2 s duration 4 m/s gusts in the $-e_1$ direction. All three controllers use the same outer-loop control. Grey area represents desired altitude based on fan output.

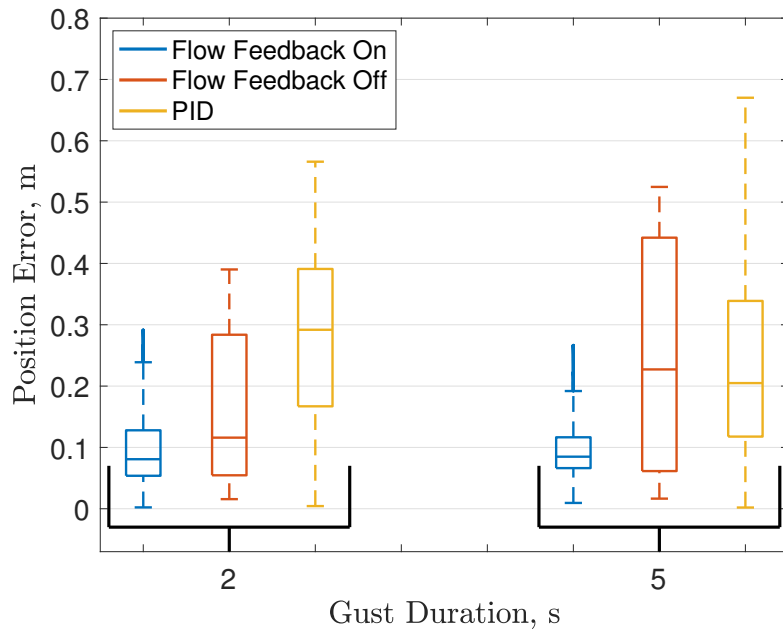


Figure 6.10: Horizontal Euclidean-distance error for each controller at the two different gust frequencies. Boxes show 25th and 75th percentiles and median, whiskers show non-outlier values, and additional points show outliers.

utilizing flow feedback. Both controllers without flow feedback experience significant disturbance in the wind direction, and while the PID controller is able to begin bringing the quadrotor back to the desired position, it suffers from windup overshoot when the gust ceases, similar to the 3DOF test cases. For both gust frequencies, flow feedback allows the quadrotor to detect the gust earlier, and when combined with the model of the dynamic response, the quadrotor directly opposes the resulting aerodynamic moment without first requiring rigid-body accelerations. The initial deviation of each of the other controllers without flow feedback is a direct result of the limitations of IMU sensing, responding only after the vehicle begins to accelerate away from the desired hover position. The fast response and lack of an integral term on the $SO(3)$ controller without flow sensing cause it to follow the disturbance closely, and in fact it maintains a tight position-hold outside of the dynamic portions of the wind gust. The PID controller begins to correct for the disturbance, but is unable to return to the desired position prior to the cessation of the gust, leading to oscillating behavior. Oscillations continue to the point of resonance in the case of the two second gust, though further tuning may address this issue.

The box plot in Fig. 6.10 provides statistical insight into the behavior of each controller for the duration of each test. Flow feedback provides good performance, which is similar for the two different gust frequencies. The $SO(3)$ controller without flow feedback shows improved performance in the shorter gusts compared to the longer gusts that maintain a stronger wind while the blinds are open. Conversely, the PID controller has better performance for the longer gusts due to the resonant state in shorter gusts. The box plot also shows that only the controller with flow

feedback has outliers. This result may be due to the noise in the flow probes, particularly in the lateral direction where no wind is actually flowing over the whole quadrotor. The quadrotor responds to this measurement that is likely a result of the inflow aerodynamics through the rotors, which leads to slightly less consistent behavior in flight.

6.2 Linear Controller

Experimental testing for the linear controller was performed in a similar fashion to that of the nonlinear position and attitude controller, by subjecting the quadrotor to a series of square-wave gusts at different periods in the indoor gust generation facility. Figures 6.11 and 6.12 show displacement in the \mathbf{e}_1 direction as well as the flow speed experienced by the quadrotor. Figures 6.13 and 6.14 show the \mathbf{e}_1 - \mathbf{e}_2 displacement on the left plot and the \mathbf{e}_1 - \mathbf{e}_3 displacement on the right plot over the course of each test.

Figures 6.11 and 6.12 show improvement in station holding through the use of flow sensing for both tests. The longer time-scale gusts in Figure 6.11 show a more significant improvement, where both controllers are able to settle before and after the gusts. Without flow feedback, the quadrotor is blown back by the wind where it keeps a very consistent position until the gust ceases, and with flow feedback the quadrotor quickly compensates for the wind, and experiences only a slight movement in the direction of the wind. The shorter time scale results in Figure 6.12 still show an improvement through the addition of flow feedback, but highlight the capability

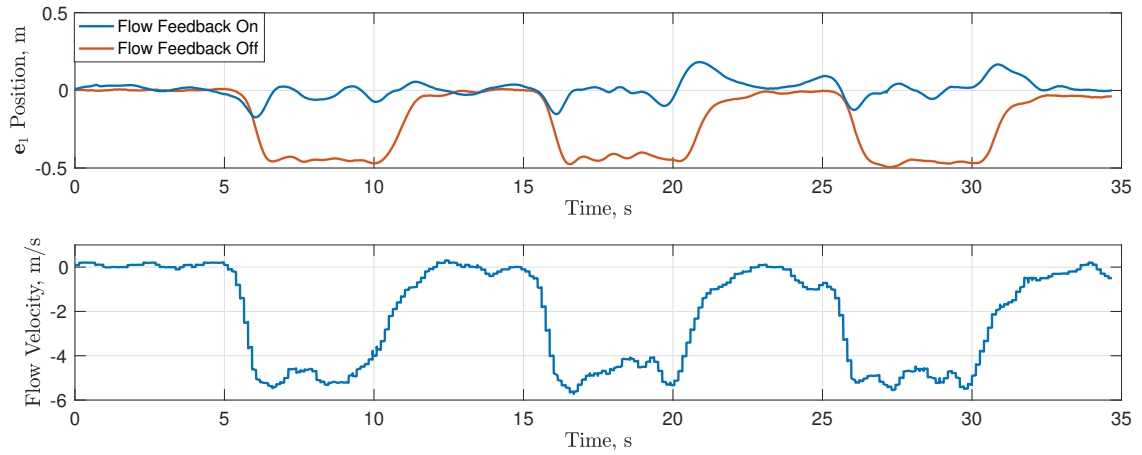


Figure 6.11: Experimental quadrotor e_1 position error in response to 5 s duration 5 m/s gusts in the $-e_1$ direction using a linear controller. Flow velocity is measured onboard using a custom flow probe.

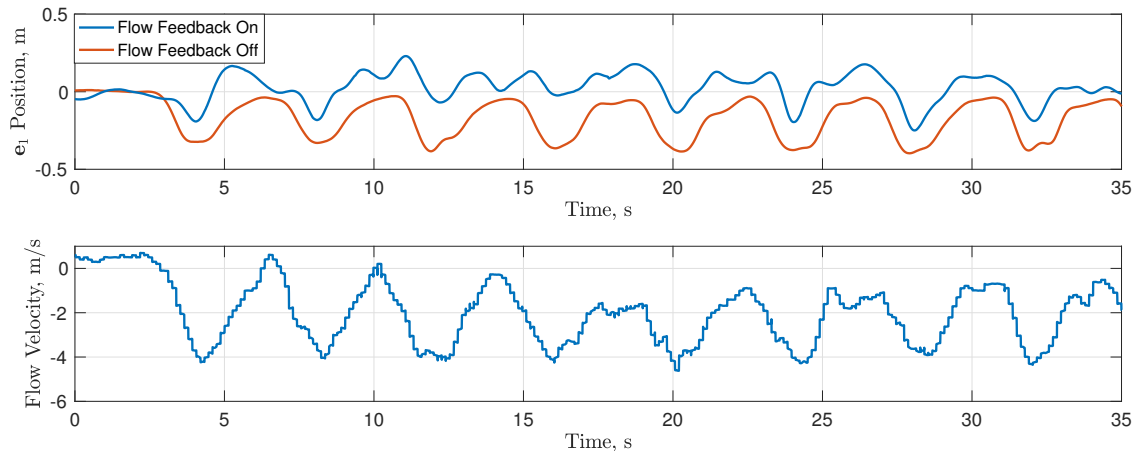


Figure 6.12: Experimental quadrotor e_1 position error in response to 2 s duration 4 m/s gusts in the $-e_1$ direction using a linear controller. Flow velocity is measured onboard using a custom flow probe.

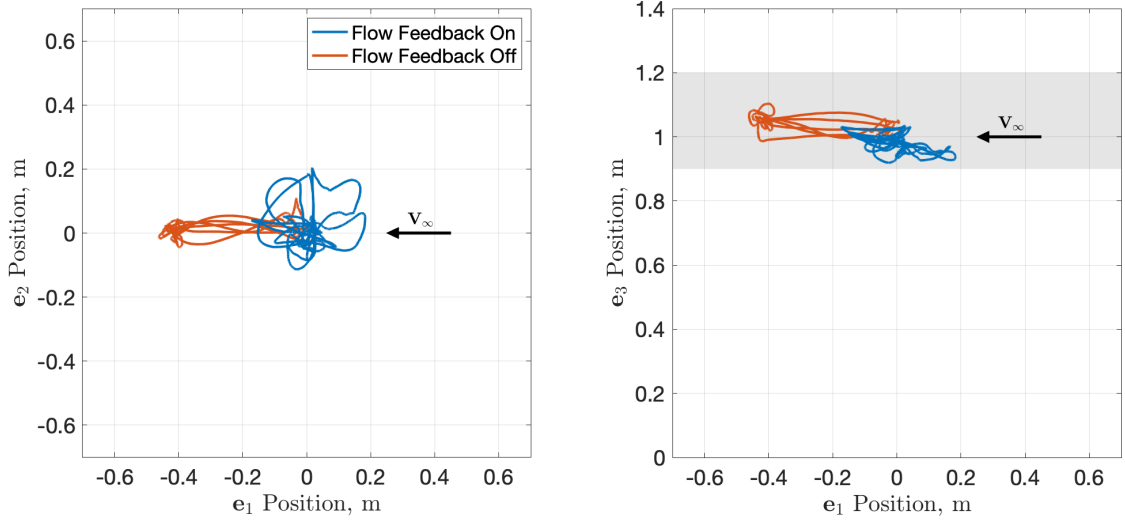


Figure 6.13: Experimental quadrotor position response to 5 s duration 5 m/s gusts in the $-e_1$ direction using a linear controller. Grey area represents desired altitude based on fan output.

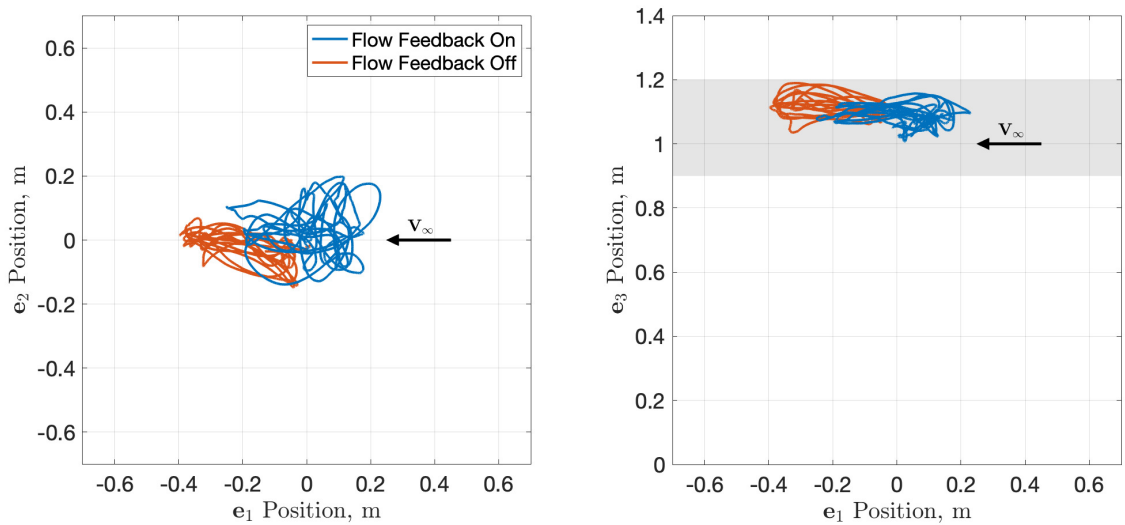


Figure 6.14: Experimental quadrotor position response to 2 s duration 4 m/s gusts in the $-e_1$ direction using a linear controller. Grey area represents desired altitude based on fan output.

even without flow sensing from designing the controller for disturbance rejection in CONDUIT[®]. Furthermore, the shorter gusts reveal the susceptibility to noise when using flow feedback.

The linear controller produced by CONDUIT[®] is designed to address higher frequency turbulent wind using the disturbance rejection bandwidth specification [59] without the use of flow sensing, and thus shows comparatively better results in the two second gusts versus testing with five second gusts. Adding flow feedback does reduce the \mathbf{e}_1 error in the system, however the movement appears slightly more erratic than in the longer time-scale case. The error at the beginning and end of each gust remains consistent between the longer and shorter gusts, however the shorter gusts limit the system's time to stabilize and thus show the quadrotor repeatedly overshooting the desired position as wind conditions change.

The differences in performance for the two time scales are highlighted in Figures 6.13 and 6.14, where in the longer time-scale gusts the systems generally maintain a tight position with or without flow sensing apart from the dynamic portion of the gust. Figure 6.14 shows the quadrotor unable to maintain the tight position in the presence of more rapid gusts for both cases and also show significant motion in the \mathbf{e}_2 direction when flow feedback is utilized, resulting from noise and faulty measurements in the flow signal in the lateral direction. In the longer-time-scale gusts, the \mathbf{e}_2 flow error reduces as the vehicle settles. However, the more dynamic wind in the shorter time-scale leads to fluctuation in the \mathbf{e}_2 direction in addition to the response to the primary flow in the \mathbf{e}_1 direction. This is most likely due to inflow aerodynamics influencing the flow field around the flow probes.

Chapter 7: Conclusion

This work details an investigation into quadrotor stability in wind, including aerodynamics, controller development, and sensing modalities. The effort begins by developing a physics-based model of the blade-flapping phenomena for quadrotor propellers that includes the effect of linear inflow dynamics, and is then simplified to improve tractability for small flight controllers. The blade-flapping model is used to predict the forces and moments at the propeller hub, which are validated by an experiment using a rotor-pendulum test stand.

The aerodynamic forces and moments are added to the model of a quadrotor, first in an attitude-only 3DOF case, and then for a full 6DOF free-flying quadrotor. The model of the quadrotor is developed on $SE(3)$, which provides a geometric description of the quadrotor's motion, and avoids singularities in the kinematics associated with Euler angles. A feedback-linearization controller is able to directly address the quadrotor's nonlinear kinematics as well as the aerodynamic terms. Furthermore, a variable-gain algorithm is developed that addresses thrust saturation when the control gains are sufficiently high to saturate the motors, so that the direction of the desired moment on the vehicle is preserved. Simulated results for both 3DOF and 6DOF controllers show the benefits of flow sensing and variable

gains.

A linear controller is developed separately to investigate the benefits of adding flow feedback to cancel aerodynamic forces and moments to a quadrotor whose controller is optimized for gust rejection prior to adding flow sensing. Frequency-domain system-identification provides the linear model of the quadrotor, which is used to select gains that optimally satisfy handling qualities requirements.

A custom 3DOF quadrotor attitude test stand, and custom free-flight quadrotor platform provide experimental results. All experiments use the same platform, with the reduced degree-of-freedom test stand affixing the quadrotor to a ball-joint at the center of the vehicle. Testing is performed in a motion-capture facility, in front of a gust generation system that produces square-wave wind inputs. The flight controller on the vehicle uses Cleanflight software, which was modified to run the controllers designed in this work and also interface with custom flow probes that provide wind sensing.

The nonlinear controllers show benefits through the addition of flow feedback for both free-flight and attitude-only cases. The controllers are compared to an identical controller without flow feedback as well as a more typical PID controller. Using flow feedback enables the quadrotor to counteract the pitching moment and corresponding translational disturbance resulting from a wind gust, and also avoid the integral windup associated with including an integral term in the controller. The linear controller that was specifically designed to address gust rejection experienced similar benefits through the addition of flow feedback, showing improved station holding in the presence of unsteady wind gusts. One disadvantage of incor-

porating flow sensing on a quadrotor is that the complex inflow dynamics of the quadrotor propellers interfere with wind measurements, corrupting the signal and degrading flight performance.

Future work for this project may include an effort to address the flow measurement interference from inflow dynamics, possibly through flow probe placement or advanced filtering. Additionally, the work shows potential for use in outdoor swarms, where information from one vehicle may be able to warn others of incoming wind events through the use of one or several flow-aware quadrotors in a group.

Appendix A: Blade-Flapping Equations of Motion

The equations setting up the rotor dynamics in Section 3.1 are used here to derive the blade-flapping equations for a rotor with a fixed hub, using the angular-momentum form of Newton's second law. The inertial derivative of the angular momentum along the \mathbf{c}_2 component in the hinge-axis direction is

$$\begin{aligned} \frac{\mathcal{I}d}{dt} (\mathcal{I}\mathbf{h}_{P/O'}) \cdot \mathbf{c}_2 = & dm[(-(r-e)^2 - (r-e)eC_\beta)\ddot{\beta} \\ & + (r-e)eS_\beta\dot{\beta}^2 + (-(r-e)eS_\beta - \frac{1}{2}(r-e)^2S_{2\beta})\omega^2] \end{aligned} \quad (\text{A.1})$$

and the corresponding moment $\mathbf{M}_{O'} \cdot \mathbf{c}_2$ is

$$\begin{aligned} \mathbf{c}_2 \cdot \int_0^{\bar{r}} \mathbf{r}_{P/O'} \times d\mathbf{F}_P^{(n)} = & - \int_e^{\bar{r}} (eC_\beta + (r-e))dF_3 \\ & + \int_e^{\bar{r}} eS_\beta dF_1 + \int_e^{\bar{r}} (e + (r-e)C_\beta)gdm + k_\beta\beta, \end{aligned} \quad (\text{A.2})$$

where the final term is the torsional spring moment. Applying Newton's second law to equate (A.1) and (A.2) and substituting for dF_1 yields

$$\begin{aligned} \int_e^{\bar{r}} (r-e)^2\ddot{\beta}dm + \int_e^{\bar{r}} [(r-e)eS_\beta + \frac{1}{2}(r-e)^2S_{2\beta}]\omega^2dm \\ = \int_e^{\bar{r}} (r-e)dF_3 - k_\beta\beta - \int_e^{\bar{r}} (r-e)C_\beta gdm. \end{aligned} \quad (\text{A.3})$$

The following substitutions are made according to convention [60]: I_β is the blade moment of inertia, N_β is the blade static moment, and M'_β is the aerodynamic moment on the blade, i.e., $I_\beta = \int_e^{\bar{r}} (r-e)^2dm$, $N_\beta = \int_e^{\bar{r}} (r-e)dm$, and $M'_\beta =$

$\int_e^{\bar{r}}(r - e)dF_3$. Equation (A.3) becomes

$$I_\beta \ddot{\beta} + \left(N_\beta e S_\beta + \frac{1}{2} I_\beta S_{2\beta} \right) \omega^2 + k_\beta \beta = M'_\beta - N_\beta g C_\beta. \quad (\text{A.4})$$

Define ω_{β_0} as the torsional spring natural frequency, i.e., $\omega_{\beta_0} = \sqrt{k_\beta/I_\beta}$. The flap angle β is expected to remain sufficiently small to permit the small-angle assumption [19, 27]. These substitutions yield

$$\beta^{**} + \left(1 + \frac{N_\beta e}{I_\beta} + \frac{\omega_{\beta_0}^2}{\omega^2} \right) \beta = \frac{M'_\beta}{I_\beta \omega^2} - \frac{N_\beta g}{I_\beta \omega^2}, \quad (\text{A.5})$$

where * denotes differentiation with respect to ψ such that $\dot{\beta} \triangleq \omega \beta^*$, following convention [19]. Set $\nu_\beta^2 = (1 + N_\beta e/I_\beta + \omega_{\beta_0}^2/\omega^2)$, and define ρ as the density of air, C_{ℓ_α} as the lift slope, c as the blade chord, and consider the Lock number $\gamma = \rho C_{\ell_\alpha} c \bar{r}^4 / I_\beta$. Then define $M'_\beta / (I_\beta \omega^2) = \gamma M_\beta$, where $M_\beta = (\rho C_{\ell_\alpha} c \bar{r}^4 \omega^2)^{-1} \int_e^{\bar{r}}(r - e)dF_3$. With these final substitutions, (A.5) becomes the canonical blade-flapping equation, i.e.,

$$\beta^{**} + \nu_\beta^2 \beta = \gamma M_\beta - \frac{g N_\beta}{\omega^2 I_\beta}. \quad (\text{A.6})$$

The value for the aerodynamic moment M_β is derived using the lift and drag forces in the \mathbf{d}_3 direction. Define α_{ind} as induced angle of attack due to the relative wind, dL as the differential lift, and dD as the differential drag. Assume both α_{ind} and dD are small, yielding

$$dF_3 = C_{\alpha_{ind}} dL - S_{\alpha_{ind}} dD \approx dL. \quad (\text{A.7})$$

Denote by U_T the tangential component (relative to \mathbf{d}_2) of the flow velocity, U_P the perpendicular component of flow velocity, $\alpha_{eff} = \alpha_{geo} - \alpha_{ind}$ the effective angle of attack, and $\alpha_{geo} = \theta_0 + \theta_{tw} r'$ the geometric angle of attack, as seen in Fig. A.1.

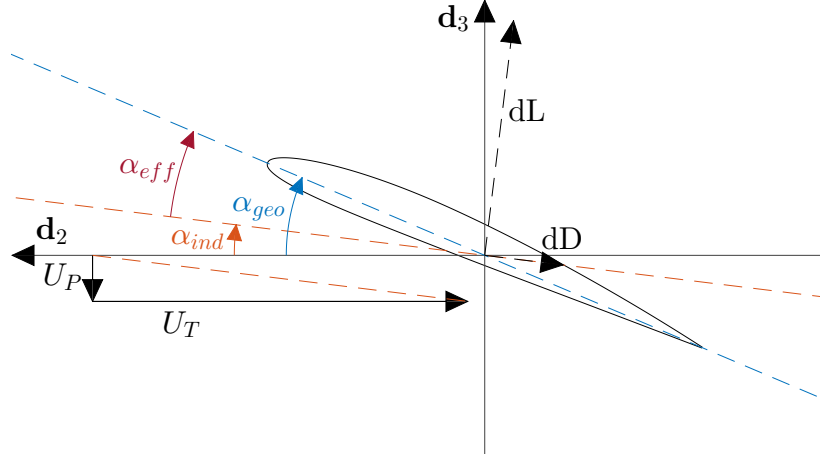


Figure A.1: Aerodynamic forces and angles on a rotor blade

Parameter θ_0 is the root angle of attack, θ_{tw} is the linear twist of the blade, and $r' = r/\bar{r}$ is the blade element distance as a fraction of total length. Define

$$\begin{aligned} dL &= \frac{1}{2}\rho U_T^2 c C_{l_\alpha} \alpha_{eff} dr, \\ \alpha_{ind} &= \tan^{-1}\left(\frac{U_P}{U_T}\right) \approx \left(\frac{U_P}{U_T}\right), \end{aligned} \tag{A.8}$$

where the final approximation holds because $U_P \ll U_T$.

In order to model the tangential and perpendicular flow over the blade, define inflow $\lambda_i = \lambda_0(1 + k_{\lambda_x} r' \cos \psi)$ using a linear inflow model [19]. When investigating blade flapping, uniform inflow is often assumed in quadrotor literature [23, 24, 27]; however, Niemiec and Gandhi [61] showed that using uniform inflow in trim calculations considerably underpredicts pitching moment as compared to linear inflow. Furthermore, in this work, uniform inflow has proven insufficient to predict forces and moments on the hub when comparing to experimental results. Additionally, the inflow ratio λ_0 is typically solved implicitly, though for this work a simpler fixed value shows sufficient accuracy over a range of conditions. The parameter

$k_{\lambda_x} = (15\pi/23) \tan(\chi/2)$ is taken from the model by Pitt and Peters [19], where $\chi = \tan^{-1}(\mu/\lambda_0)$ [62] and μ is the advance ratio of the propeller, which is the ratio of wind speed over the hub to the tip speed of the blades.

The tangential and perpendicular flow over the propeller are

$$\begin{aligned} U_T &= \omega r + \mu\omega\bar{r}S_\psi, \\ U_P &= \lambda_i\omega\bar{r} + \omega\beta^*(r - e) + \mu\omega\bar{r}S_\beta C_\psi. \end{aligned} \quad (\text{A.9})$$

Applying a small angle assumption to U_P and defining $e' = \frac{e}{r}$ and $dr' = \frac{dr}{r}$ yields

$$\begin{aligned} M_\beta &= \frac{1}{2} \int_{e'}^1 (r' - e') \left[(\theta_0 + \theta_{tw}r') (r' + \mu S_\psi) \right. \\ &\quad \left. - [\lambda_0(1 + k_{\lambda_x}r'C_\psi) + \beta^*(r' - e') + \mu\beta C_\psi] (r' + \mu S_\psi) \right] dr'. \end{aligned} \quad (\text{A.10})$$

Integrating M_β and substituting into (A.6) gives

$$\begin{aligned} &\beta^{**} + \frac{\gamma}{8} \left[\left(1 - \frac{8e'}{3} + 2e'^2 - \frac{e'^4}{3} \right) + \left(\frac{4}{3} - 4e' + 4e'^2 - \frac{4e'^3}{3} \right) \mu S_\psi \right] \beta^* \\ &+ \left\{ \frac{\gamma}{8} \left[\left(\frac{4}{3} - 2e' + \frac{2e'^3}{3} \right) \mu C_\psi + (1 - 2e' + e'^2) \mu^2 S_{2\psi} \right] + \left(1 + \frac{N_\beta e}{I_\beta} + \frac{\omega_{\beta_0}^2}{\omega^2} \right) \right\} \beta \\ &= \frac{\gamma}{8} \theta_0 \left[\left(1 - \frac{4e'}{3} + \frac{e'^4}{3} \right) + \left(\frac{8}{3} - 4e' + \frac{4e'^3}{3} \right) \mu S_\psi + (2 - 4e' + 2e'^2) \mu^2 S_\psi^2 \right] \\ &+ \frac{\gamma}{8} \theta_{tw} \left[\left(\frac{4}{5} - e' + \frac{e'^5}{5} \right) + \left(2 - \frac{8e'}{3} + \frac{2e'^4}{3} \right) \mu S_\psi + \left(\frac{4}{3} - 2e' + \frac{2e'^3}{3} \right) \mu^2 S_\psi^2 \right] \\ &- \frac{\gamma}{8} \lambda \left[\left(\frac{4}{3} - 2e' + \frac{2e'^3}{3} \right) + (2 - 4e' + 2e'^2) \mu S_\psi \right] \\ &- \frac{\gamma}{8} \lambda k_{\lambda_x} \left[\left(1 - \frac{4e'}{3} + \frac{e'^4}{3} \right) C_\psi + \left(\frac{2}{3} - e' + \frac{e'^3}{3} \right) \mu S_{2\psi} \right] \left\} - \frac{gN_\beta}{\omega^2 I_\beta} \end{aligned} \quad (\text{A.11})$$

where the forcing terms on the right side and the β^* term result from the solution to the aerodynamic moment M_β .

Although this work is primarily motivated by the the propeller's behavior in wind, setting the advance ratio μ to zero (as in hover) gives intuition by representing

the propeller as a damped second-order system. Here the forcing function arises from a (virtual) periodic increase in angle of attack analogous to a full-size helicopter's cyclic pitch input, e.g., the angle of attack is higher on the advancing side, lower on the retreating side, and unchanged over the nose and tail. Although it is not possible to physically change the angle of attack of each blade on the propeller, the solution serves as a theoretical tool for comparison against full-size helicopters. Redefining (A.11) using the normalized derivative with respect to time, i.e., $\dot{\beta}^* \triangleq \dot{\beta}/\omega$, setting $\mu = 0$, assuming virtual cyclic input such that $\theta = (\theta_0 + \theta_{tw}r')(1 + \theta_{1s} \sin \psi)$, where θ_{1s} is the magnitude of the cyclic input, and ignoring constant offset in forcing yields the classical, damped second-order system with natural frequency ω_n , damping ratio ζ , and forcing function $A\omega^2 \sin(\omega t)$, where A is a constant, i.e.,

$$\ddot{\beta} + 2\zeta\omega_n\dot{\beta} + \omega_n^2\beta = A\omega^2 \sin(\omega t). \quad (\text{A.12})$$

Comparing (A.12) to (A.11), the damping ratio is $\zeta = \gamma/(16\nu_\beta)(1 - 8e'/3 + 2e'^2 - e'^4/3)$ and the natural frequency is $\omega_n = \omega\nu_\beta$. Solving (A.12) yields the particular solution

$$\beta_p = \beta_{max} \sin(\omega t - \phi_D), \quad (\text{A.13})$$

where

$$\beta_{max} = \frac{A}{\sqrt{\left(\left(\frac{\omega_n}{\omega}\right)^2 - 1\right)^2 + (2\zeta\frac{\omega_n}{\omega})^2}}, \quad (\text{A.14})$$

$$\phi_D = \tan^{-1} \left(\frac{2\zeta\frac{\omega_n}{\omega}}{\left(\frac{\omega_n}{\omega}\right)^2 - 1} \right).$$

Here, β_{max} indicates the maximum flapping deviation of the propeller from nominal angle β_0 , and ϕ_D represents the azimuthal angular phase delay between the apparent

maximum aerodynamic force when the advancing blade is moving directly into the wind, and the maximum flapping amplitude.

Figure A.2 (adapted from [60]) shows phase-delay solutions to (A.12) for varying natural frequency and damping ratio. For a typical full-size helicopter with $\nu_\beta = 1.04$ and $\zeta = 0.42$, the phase delay is 85° [60]. Analysis of a small, stiff propeller is performed using a Gemfan 5030 propeller rotating at 8000 rpm. The propeller is 2.7 grams and 12.7 centimeters in diameter, with a 1.5 centimeter chord. Assuming $e' = 0.1$ and $k_\beta = 3$ Nm/rad based on model and experimental fit below, the values of the characteristic blade-parameters are as follows: scaled natural frequency $\nu_\beta = 1.9$, damping ratio $\zeta = 0.026$, and Lock number $\gamma = 1.04$. Due to the atypical values of these parameters compared to full-scale helicopters, the hover flap response to this virtual excitation is also atypical: the phase delay is $\phi_D = 2.2^\circ$, as shown by Fig. A.2.

When solving (A.11) assuming wind over the hub with nonzero advance ratio, periodic terms do not allow for a true analytical solution. However, by taking the Fourier series solution and retain only first harmonics, i.e., $\beta(\psi) = \beta_0 + \beta_{1c} \cos \psi + \beta_{1s} \sin \psi$, it is possible to harmonically match constant and periodic (sine and cosine) terms on each side of the equation [19]. The resulting solution is

$$\begin{aligned} \beta_0 = & \frac{\gamma}{8\nu_\beta^2} \left\{ - \left(e' - 2e'^2 + \frac{e'^3}{3} \right) \mu \beta_{1c} + \theta_0 \left[\left(1 - \frac{4e'}{3} + \frac{e'^4}{3} \right) + (1 - 2e' + 1e'^2) \mu^2 \right] \right. \\ & \left. + \theta_{tw} \left[\left(\frac{4}{5} - e' + \frac{e'^5}{5} \right) + \left(\frac{2}{3} - e' + \frac{e'^3}{3} \right) \mu^2 \right] - \lambda \left(\frac{4}{3} - 2e' + \frac{2e'^3}{3} \right) \right\} \end{aligned} \quad (\text{A.15})$$

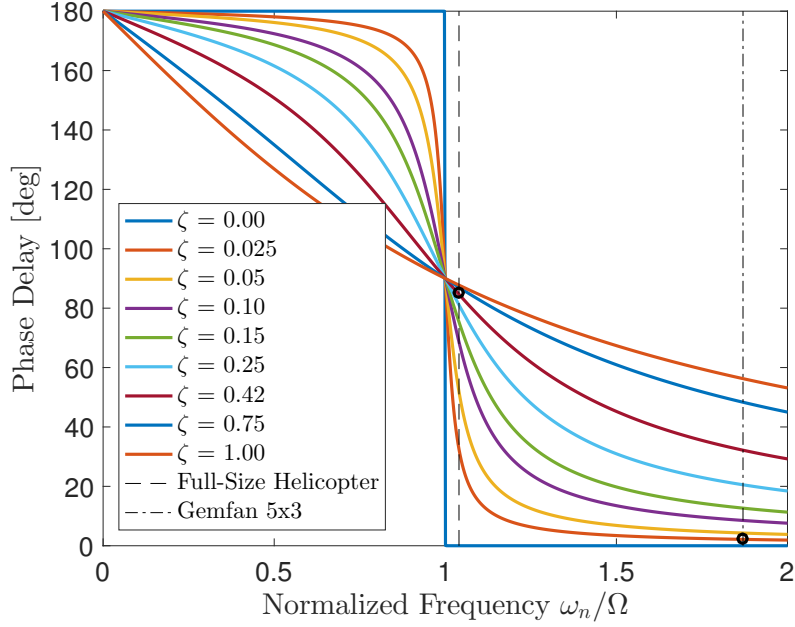


Figure A.2: Blade-flapping phase delay in hover

$$\beta_{1c} = \frac{\gamma}{8(\nu_\beta^2 - 1)} \left\{ - \left[\left(1 - \frac{8e'}{3} + 2e'^2 - \frac{e'^4}{3} \right) + (1 - 2e' + e'^2) \mu^2 \right] \beta_{1s} - \left(\frac{4}{3} - 2e' + \frac{2e'^3}{3} \right) \mu \beta_0 - \lambda k_{\lambda_x} \left(1 - \frac{4e'}{3} + \frac{e'^4}{3} \right) \right\} \quad (\text{A.16})$$

$$\beta_{1s} = \frac{\gamma}{8(\nu_\beta^2 - 1)} \left\{ \left[\left(1 - \frac{8e'}{3} - 2e'^2 - \frac{e'^4}{3} \right) + (1 - 2e' + e'^2) \mu^2 \right] \beta_{1c} + \theta_0 \left[\left(\frac{8}{3} - 4e' + \frac{4e'^3}{3} \right) \mu \right] + \theta_{tw} \left[\left(2 - \frac{8e'}{3} + \frac{2e'^4}{3} \right) \mu \right] - \lambda \left[(2 - 4e' + 2e'^2) \mu \right] \right\} \quad (\text{A.17})$$

Equations (A.15–A.17) yield very different characteristics compared to (A.14), primarily due to the presence of the linear inflow term $\lambda_0 k_{\lambda_x}$ in (A.16), which changes the azimuth angle of the maximum aerodynamic force. Specifically, the linear inflow model yields a 97% change in phase delay compared to (A.14), versus a 1% change when assuming uniform inflow. In order to identify β_{max} and ϕ_D with $\mu \neq 0$, apply

the sinusoidal relationship $A \cos(\omega t + \phi) = I \cos \omega t - Q \sin \omega t$ [63], which shows

$$\beta(\psi) = \beta_0 + \sqrt{\beta_{1c}^2 + \beta_{1s}^2} \sin \left[\psi - \left(\tan^{-1} \left(\frac{\beta_{1s}}{\beta_{1c}} \right) - \frac{\pi}{2} \right) \right]. \quad (\text{A.18})$$

Comparing (A.18) to (A.13) indicates the maximum flap amplitude variation $\beta_{max} = \sqrt{\beta_{1c}^2 + \beta_{1s}^2}$ and phase delay $\phi_D = \tan^{-1}(\beta_{1s}/\beta_{1c}) - \pi/2$. Assuming the same values as above for e' , k_β , and propeller speed, the phase delay and maximum flap of the propeller in 3 m/s wind are $\phi_D = 81^\circ$ and $\beta_{max} = 0.10^\circ$. This result is expanded upon in Section 3.2 to identify the forces and moments acting on the propeller.

Appendix B: Cleanflight Software Modifications

Changes made to the Cleanflight software to add the controllers and sensing presented in this work are listed here. Both the firmware and the user interface were updated.

B.1 Firmware

B.1.1 Update for controller

pid.c

- modified the final pid function “pidController” to use SO(3) and flow cancelling framework
- Created “pidInitInertia” to set inertial parameters since that doesn’t need to be run every PID loop
- flowUpdate here, but not flowInit!
- #include time.h fc/config.h and flow.h
- updated default PID values
- set constants and initialized variables at the top of the file
- Edited P gains in the RESET_CONFIG

pid.h

- adjusted pid limits

imu.c

- Added rotation matrix functions “SO3AttitudeError1,2,3” for pid.c

imu.h

- Included rotation matrix functions

B.1.2 Update for flow sensors

flow.c and flow.h

- created, modeled off of gps.c and gps.h

Makefile

- add sensors/flow.c to normal and speed optimized src

parameter_group_ids.h

- #defined PG_FLOW_CONFIG

flight/mixer.c

- Removed pid scaling and limiting
- Removed normalizing for the mix
- Removed motorOutputRange multiplier for motors since they're already in the desired

units

- include build/debug.h to debug some of the variables

fc/config.c

- added a section to clear FEATURE_FLOW if USE_FLOW is not defined (and added the same for other features based on newer versions of cleanflight)

fc/config.h

- added FEATURE_FLOW to features_e (Needs to match the number in Features.js)

io/serial.h

- added FUNCTION_FLOW to serialPortFunction_e (needs to match number in MSPHelper.js)
- added uint8_t flow_baudrateIndex

io/serial.c

- Added serial port configuration if FLOW_UART is defined

sensors/sensors.h

- added SENSOR_FLOW to sensors_e

sensors/barometer.c

- updated baro_hardware to be BARO_DEFAULT from newer cleanflight to get baro to work on Matek

sensors/compass.c

- mag_hardware to MAG_DEFAULT

sensors/compass.h

- added mag_bustype through ioTag_t mag_spi_csn

fc/cli.c

- added FLOW to featureNames, and sensorTypeNames and added flow.h to the file and flow.h header
- Don't need to play with the baud rate stuff at all (gps bauds cover all serial sensors)

fc/fc_init.c

- added flow initiation if FEATURE_FLOW active and added flow.h to the file

fc/fc_tasks.c

- enable flow task if USE_FLOW and FEATURE_FLOW active and added flow.h header to the file
- added TASK_FLOW with 100 hz sample rate and medium priority

target/common_fc_pre.h

- added #define USE_FLOW
- Set debug mode to flow (#define DEBUG_MODE DEBUG_FLOW)

scheduler/scheduler.h

- #ifdef USE_FLOW, run TASK_FLOW

fc/settings.c

- added PG_FLOW_CONFIG stuff (may not be needed, but seems relevant), and flow.h header

build/debug.h

- added DEBUG_FLOW as a debug option (and updated the flow script accordingly)

target/MATEKF405/target.h

- added flow uart and gps uart definitions for automatically setting them up on the GUI
- added serialRX provider
- defined MAG and set up i2c section, which includes BARO section
- default features: motor stop, flow, gps
- default current and voltage source ADC, set current meter scale

target/MATEKF405/target.mk

- added accgyro_spi_mpu6000 driver, barometer drivers, and compass drivers

B.1.3 Notes

- Need to edit io/osd.c to show the information on an FPV display
- don't need the flow_yeo or flow_fake drivers
- Don't need to add flow baud rate code, gps covers all serial sensors. Unnecessarily changed files: fc/fc.msp, io/serial.c. Other affected files that were also modified for other

reasons: fc/cli.c, io/serial.h

B.2 Configurator

Note: I added flow baud rate code, but later realized that the gps baud rate serves as the sensor baud rate, so I don't need to add flow baud rate code, and it actually causes problems for the gui.

Features.js

- added FLOW to features tab (needs to match number in fc/config.h)

tabs/ports.js

- added FLOW port to sensors dropdown
- added FLOW to gpsbaudrate on 182 so that it doesn't default to flow for that.

js/msp/MSPHelper.js

- add FLOW to self.SERIAL_PORT_FUNCTIONS (Needs to match the number in main/io/serial.h)

locales/en/messages.json

- Added message for flow, and description for the FLOW feature in configuration tab

Bibliography

- [1] Chris Anderson. 10 breakthrough technologies: Agricultural drones. *MIT Technology Review*, 117(3):58–60, 2014.
- [2] Matthew Hutson. Hurricanes show why drones are the future of disaster relief. *NBC MACH*, sep 2017.
- [3] Meredith Cohn. University of Maryland Medical Center transplants first drone-delivered organ, 2019.
- [4] Gregory M Gremillion and J Sean Humbert. Disturbance rejection with distributed acceleration sensing for small unmanned aircraft systems. *AIAA Journal*, 54(8):2233–2246, 2016.
- [5] Derrick Yeo, Nitin Sydney, Derek Paley, and Donald Sofge. Onboard flow sensing for downwash detection and avoidance on small quadrotor helicopters. In *AIAA Guidance, Navigation, and Control Conference, AIAA SciTech Forum, Paper AIAA 2015-1769*, pages 1–12, Kissimmee, FL, 2015.
- [6] Nitin J Sanket, Chahat Deep Singh, Kanishka Ganguly, Cornelia Fermüller, and Yiannis Aloimonos. GapFlyt: Active vision based minimalist structureless gap detection for quadrotor flight. *IEEE Robotics and Automation Letters*, 3(4):2799–2806, 2018.
- [7] Sergei Lupashin, Angela Schöllig, Michael Sherback, and Raffaello D’Andrea. A simple learning strategy for high-speed quadcopter multi-flips. In *IEEE International Conference Robotics and Automation*, pages 1642–1648, Anchorage, AK, 2010.
- [8] Farhad Goodarzi, Daewon Lee, and Taeyoung Lee. Geometric adaptive tracking control of a quadrotor unmanned aerial vehicle on $SE(3)$ for agile maneuvers. *Journal of Dynamic Systems, Measurement, and Control*, 137(9):1–12, 2015.
- [9] Alexander Lanzon, Alessandro Freddi, and Sauro Longhi. Flight control of a quadrotor vehicle subsequent to a rotor failure. *Journal of Guidance, Control, and Dynamics*, 37(2):580–591, 2014.

- [10] Taeyoung Lee. Geometric control of quadrotor UAVs transporting a cable-suspended rigid body. *IEEE Transactions on Control Systems Technology*, 26(1):255–264, 2018.
- [11] Pedro O. Pereira and Dimos V. Dimarogonas. Control framework for slung load transportation with two aerial vehicles. In *IEEE Conference on Decision and Control*, pages 4254–4259, Melbourne, Australia, 2018.
- [12] Ella M Atkins. Risk identification and management for safe UAS operation. In *International Symposium on Systems and Control in Aeronautics and Astronautics*, pages 774–779, Harbin, China, 2010.
- [13] Hao Lu, Cunjia Liu, Lei Guo, and Wen-Hua Chen. Flight control design for small-scale helicopter using disturbance-observer-based backstepping. *Journal of Guidance, Control, and Dynamics*, 38(11):2235–2240, 2015.
- [14] S. Zarovy, M. Costello, and A. Mehta. Experimental method for studying gust effects on micro rotorcraft. *Journal of Aerospace Engineering*, 227(4):703–713, 2012.
- [15] Marcos G Berrios, Tom Berger, Mark B Tischler, Ondrej Juhasz, and Frank C Sanders. Hover flight control design for UAS using performance-based disturbance rejection requirements. In *AHS Int. 73rd Annual Forum*, page 23, Fort Worth, TX, 2017.
- [16] David W Kun and Inseok Hwang. Linear matrix inequality-based nonlinear adaptive robust control of quadrotor. *Journal of Guidance, Control, and Dynamics*, 39(5):1–13, 2015.
- [17] Gregory M Gremillion, Lina M Castano, and J Sean Humbert. Disturbance rejection with distributed acceleration and strain sensing. In *AIAA SciTech*, pages 1–17, Kissimmee, FL, 2015.
- [18] Ondrej Juhasz, Mark J.S. Lopez, Marcos G. Berrios, Tom Berger, and Mark B. Tischler. Turbulence modeling of a small quadrotor UAS using system identification from flight data. In *AHS Technical Meeting on VTOL Unmanned Aircraft Systems*, pages 1–11, Mesa, AZ, 2017.
- [19] J. Gordon Leishman. *Principles of Helicopter Aerodynamics*. Cambridge University Press, New York, NY, 2nd edition, 2006.
- [20] Daniel Mellinger and Vijay Kumar. Minimum snap trajectory generation and control for quadrotors. In *IEEE International Conference Robotics and Automation*, pages 2520–2525, Shanghai, China, 2011.
- [21] Mark Cutler and Jonathan P. How. Analysis and control of a variable-pitch quadrotor for agile flight. *Journal of Dynamic Systems, Measurement, and Control*, 137(10):1–14, 2015.

- [22] Philippe Martin and Erwan Salaün. The true role of accelerometer feedback in quadrotor control. In *IEEE International Conference on Robotics and Automation*, pages 1623–1629, Anchorage, AK, 2010.
- [23] P. Pounds, R. Mahony, and P. Corke. Modelling and control of a large quadrotor robot. *Control Engineering Practice*, 18(7):691–699, 2010.
- [24] Robert Mahony, Vijay Kumar, and Peter Corke. Modeling, estimation, and control of quadrotor. *IEEE Robotics and Automation Magazine*, pages 20–32, sep 2012.
- [25] Sammy Omari, Minh-Duc Hua, Guillaume Ducard, and Tarek Hamel. Non-linear control of VTOL UAVs incorporating flapping dynamics. In *2013 IEEE/RSJ International Conference on Intelligent Robots and Systems*, pages 2419–2425, Tokyo, 2013. IEEE.
- [26] Jean-Marie Kai, Guillaume Allibert, Minh-Duc Hua, and Tarek Hamel. Nonlinear feedback control of Quadrotors exploiting First-Order Drag Effects. *IFAC Papers Online*, 50(1):8189–8195, 2017.
- [27] Gabriel Hoffmann, Haomiano Huang, Steven Waslander, and Claire Tomlin. Quadrotor helicopter flight dynamics and control: theory and experiment. In *Proc. AIAA Guidance, Navigation, and Control Conf., Paper AIAA 2007-6461*, pages 1–20, Hilton Head, SC, 2007.
- [28] Derrick W Yeo, Nitin Sydney, and Derek A Paley. Onboard flow sensing for multi-rotor pitch control in wind. *Journal of Guidance, Control, and Dynamics*, 41(5):1193–1198, 2018.
- [29] S Prudden, A Fisher, A Mohamed, and S Watkins. A flying anemometer quadrotor: Part 1. In *Proceedings of the 7th International Micro Air Vehicle Conference and Competition - Past, Present and Future*, pages 1–7, Beijing, China, 2016.
- [30] P Bruschi, M Piotto, F Dell’Agnello, J Ware, and N Roy. Wind speed and direction detection by means of solid-state anemometers embedded on small quadcopters. In *30th Eurosensors Conference, Eurosensors 2016*, volume 168, pages 802–805, Budapest, Hungary, 2016.
- [31] Ryan L. Thorpe, Matthew McCrink, and James W. Gregory. Measurement of Unsteady Gusts in an Urban Wind Field using a UAV-based Anemometer. *2018 Applied Aerodynamics Conference*, pages 1–11, 2018.
- [32] Taeyoung Lee, Melvin Leok, and N Harris McClamroch. Geometric tracking control of a quadrotor UAV on $SE(3)$. In *IEEE Conference on Decision and Control*, pages 5420–5425, Atlanta, GA, 2010.

- [33] Ning Cao and Alan F. Lynch. Inner-outer loop control for quadrotor UAVs with input and state constraints. *IEEE Transactions on Control Systems Technology*, 24(5):1797–1804, 2016.
- [34] Mark Cutler and Jonathan P How. Actuator constrained trajectory generation and control for variable-pitch quadrotors. In *AIAA Guidance, Navigation, and Control Conference*, pages 1–15, Minneapolis, MN, 2012.
- [35] Taeyoung Lee, Melvin Leok, and N. Harris Mcclamroch. Nonlinear robust tracking control of a quadrotor UAV on $SE(3)$. *Asian Journal of Control*, 15(2):391–408, 2013.
- [36] Zachary T. Dydek, Anuradha M. Annaswamy, and Eugene Lavretsky. Adaptive control of quadrotor UAVs: A design trade study with flight evaluations. *IEEE Transactions on Control Systems Technology*, 21(4):1400–1406, 2013.
- [37] Kostas Alexis, George Nikolakopoulos, and Anthony Tzes. Constrained-control of a quadrotor helicopter for trajectory tracking under wind-gust disturbances. In *IEEE Mediterranean Electrotechnical Conference*, pages 1411–1416, Valletta, Malta, 2010.
- [38] Ashton Roza and Manfredi Maggiore. A class of position controllers for underactuated VTOL vehicles. *IEEE Transactions on Automatic Control*, 59(9):2580–2585, 2014.
- [39] Andrew R. Teel. Global stabilization and restricted tracking for multiple integrators with bounded controls. *Systems and Control Letters*, 18(3):165–171, 1992.
- [40] G.J. Pappas, J. Lygeros, and D.N. Godbole. Stabilization and tracking of feedback linearizable systems under input constraints. In *IEEE Conference on Decision and Control*, pages 1–34, New Orleans, LA, 1995.
- [41] Kenny K Cheung, Joseph A Wagster IV, Mark B Tischler, Christina M Ivler, Marcos G Berrios, Tom Berger, Ondrej Juhasz, Eric L Tobias, Chad L Goerzen, Patrick S Barone, Frank C Sanders, Mark J S Lopez, and Rhys M Lehmann. An overview of the U.S. Army Aviation Development Directorate quadrotor guidance, navigation, and control project. In *American Helicopter Society 73rd Annual Forum Proceedings*, pages 1–19, Fort Worth, TX, 2017.
- [42] Mark B Tischler and Robert K Remple. *Aircraft and Rotorcraft System Identification*. American Institute of Aeronautics and Astronautics, Inc., Reston, VA, second edition, 2012.
- [43] Mark B Tischler, Tom Berger, Christina M Ivler, Mohammadreza H Mansur, Kenny K Cheung, and Jonathan Y Soong. *Practical Methods for Aircraft and Rotorcraft Flight Control Design*. American Institute of Aeronautics and Astronautics, Inc., Reston, VA, first edition, 2017.

- [44] Wei Wei, Kelly Cohen, and Mark B Tischler. System identification and controller optimization of a quadrotor UAV. In *American Helicopter Society 71st Annual Forum Proceedings*, pages 1–10, Virginia Beach, VA, 2015.
- [45] William Craig, Derrick Yeo, and Derek A Paley. Dynamics of a rotor-pendulum with a small, stiff propeller in wind. In *ASME Dynamic Systems and Controls Conference*, pages 1–10, Minneapolis, MN, 2016.
- [46] William Craig and Derek A Paley. Geometric control of quadrotor attitude in wind with flow sensing and thrust constraints. In *ASME Dynamic Systems and Controls Conference*, pages 1–8, Tysons, VA, 2017.
- [47] William Craig, J.T. Lewis, and Derek A Paley. Stabilization of a quadrotor in wind with flow sensing: Linear modeling and control for attitude and position hold. In *VFS Autonomous VTOL Technical Meeting and eVTOL Symposium*, pages 1–10, Mesa, AZ, 2019.
- [48] William Craig, Derrick Yeo, and Derek A Paley. Geometric control of a quadrotor in wind with flow sensing and thrust constraints: Attitude and position control. In *AIAA SciTech Forum, Paper AIAA 2019-1192*, pages 1–12, San Diego, CA, 2019.
- [49] William Craig, Derrick Yeo, and Derek A Paley. Geometric attitude and position control of a quadrotor in wind. *Submitted to AIAA JGCD*.
- [50] Elena Shrestha, Moble Benedict, and Derrick Yeo. Gust Disturbance Rejection Study of a Cyclocopter Micro Air Vehicle. In *AHS Int. 72nd Annual Forum*, pages 1–13, West Palm Beach, FL, 2016.
- [51] Robert T.N. Chen. A simplified rotor system mathematical model for piloted flight dynamics simulation. Technical report, 1979.
- [52] Robert T.N. Chen. Effects of primary rotor parameters on flapping dynamics. Technical Report January, 1980.
- [53] Nancy Hall. Shape Effects on Drag. On the WWW, June. URL <http://www.grc.nasa.gov/WWW/k-12/airplane/shaped.html>, 2015.
- [54] John D. Anderson. *Fundamentals of Aerodynamics*. McGraw-Hill, New York, NY, 1991.
- [55] Ira Abbot and Albert Doenhoff. *Theory of Wing Sections*. Dover Publications, New York, NY, 1959.
- [56] N. Jeremy Kasdin and Derek A Paley. *Engineering Dynamics: A Comprehensive Introduction*. Princeton University Press, Princeton, NJ, 2011.
- [57] Francesco Bullo and Andrew D. Lewis. *Geometric Control of Mechanical Systems*. Springer, New York, NY, 2005.

- [58] Bernadine E. Passe. Experimental Validation of the Blade-Flapping Dynamics of a Small, Stiff Propeller in Wind. In *AIAA Region I Student Conference*, pages 1–10, Charlottesville, VA, 2017.
- [59] Tom Berger, Christina M. Ivler, Marcos G. Berrios, Mark B. Tischler, and David G. Miller. Disturbance rejection handling qualities criteria for rotorcraft. In *AHS Int. 72nd Annual Forum*, pages 1–19, West Palm Beach, FL, 2016.
- [60] Raymond Prouty. *Helicopter Performance, Stability, and Control*. Krieger Publishing Company, Malabar, FL, 2005.
- [61] Robert Niemiec and Farhan Gandhi. Effects of inflow model on simulated aeromechanics of a quadrotor helicopter. In *AHS Int. 72nd Annual Forum*, pages 1–13, West Palm Beach, FL, 2016.
- [62] Robert Chen. A survey of nonuniform inflow models for rotorcraft flight dynamics and control applications. Technical report, NASA, Moffett Field, CA, 1989.
- [63] John B Anderson. *Carrier transmission*. IEEE Press, Piscataway, NJ, 2005.